



**UNIVERSIDAD DE GUANAJUATO**

---

---

**CAMPUS IRAPUATO – SALAMANCA  
DIVISIÓN DE INGENIERÍAS**

**CALORIMETRÍA EN EL ANÁLISIS TÉRMICO DE  
CIRCUITOS MICROELECTRÓNICOS**

**TESIS DOCTORAL**

**QUE PARA OBTENER EL GRADO:  
DOCTOR EN INGENIERÍA ELÉCTRICA**

**PRESENTA:**

**M.Sc. Ing. JORGE MARIO CRUZ-DUARTE**

**DIRECTORES:**

**DR. ARTURO GARCÍA-PÉREZ  
DR. CARLOS RODRIGO CORREA-CELY**

**SALAMANCA, GUANAJUATO**

**DICIEMBRE 2018**



**UNIVERSITY OF GUANAJUATO**

---

---

**CAMPUS IRAPUATO – SALAMANCA  
ENGINEERING DIVISION**

**CALORIMETRY IN THE THERMAL ANALYSIS  
OF MICROELECTRONIC CIRCUITS**

**DISSERTATION**

**FOR THE DEGREE OF:  
DOCTOR IN ELECTRICAL ENGINEERING**

**BY:**

**M.Sc. B.E. JORGE MARIO CRUZ-DUARTE**

**ADVISORS:**

**DR. ARTURO GARCÍA-PÉREZ  
DR. CARLOS RODRIGO CORREA-CELY**

**SALAMANCA, GUANAJUATO**

**DECEMBER 2018**



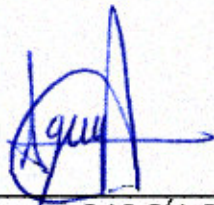
Salamanca, Gto., a 29 de octubre de 2018

**M. en I. HERIBERTO GUTIÉRREZ MARTÍN**  
**JEFE DE LA UNIDAD DE ADMINISTRACIÓN ESCOLAR**  
**PRESENTE**

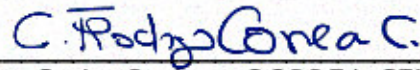
Por medio de la presente, se otorga autorización para proceder a los trámites de impresión, empastado de tesis y titulación al alumno(a) **JORGE MARIO CRUZ DUARTE** del **Programa de Doctorado en INGENIERÍA ELÉCTRICA** y cuyo número de **NUA** es **145267** del cual soy director. **El título de la tesis es: Calorimetría en el análisis térmico de circuitos microelectrónicos.**

Hago constar que he revisado dicho trabajo y he tenido comunicación con los sinodales asignados para la revisión de la tesis, por lo que no hay impedimento alguno para fijar la fecha de examen de titulación.

ATENTAMENTE



Dr. Arturo GARCÍA PÉREZ  
(Director de Tesis)  
SECRETARIO



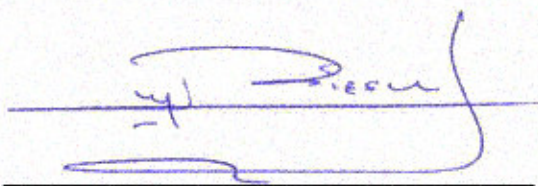
Dr. Carlos Rodrigo CORREA CELY  
(Director de Tesis)



Dr. Juan Gabriel AVIÑA CERVANTES  
PRESIDENTE



Dr. Martín VALTIERRA RODRÍGUEZ  
VOCAL



Dr. José Manuel RIESCO ÁVILA  
VOCAL



Dr. Iván Mauricio AMAYA CONTRERAS  
VOCAL

## ACKNOWLEDGEMENTS

This work would not have been possible without the financial support of the Mexican National Council of Science and Technology (CONACyT), Grant number 578594, and of the Engineering Division and Electronics Department, Campus Irapuato-Salamanca, University of Guanajuato.

I wish to present my special thanks to my advisors, Prof. Dr. C. Rodrigo Correa-Cely and Prof. Dr. Arturo García-Pérez for taught me stuff and gave me noteworthy advises.

I would like to pay my regards to the dissertation committee members, Prof. Dr. José M. Riesco-Ávila, Prof. Dr. Juan G. Aviña-Cervantes, Prof. Dr. Martín Valtierra-Rodríguez and Prof. Dr. Iván M. Amaya-Contreras for their comments and reviews.

I would like to show my warm thank to some remarkable researchers, colleagues and friends, Dr. Ignacio Martín-Díaz, M.E. Luis A. Sánchez-Galindo, Dr. J. Ulises Muñoz-Minjares, Dr. Juan M. Sierra-Hernández, Dr. Daniel Jáuregui-Vázquez, Dr. David Camarena-Martínez, Dr. J. Juan Rosales-García, Dr. Rocío A. Lizárraga-Morales, B.E. Moises Granados-Cruz, M.E. J. Roberto Huerta-Rosales, M.E. Jesús J. Yáñez-Borjas and M.E. David Matajira-Rueda, with whom I intensely discussed topics about science and life.

I do wish to express my thankfulness to my parents, Franklin and Marlene, my brothers, Luis Carlos and Emanuel Ricardo, and my girlfriend, Valentina. They have supported me in my walk and motivated me to perform all my activities with love and devotion.

I wish to present my special thanks to Prof. Dr. Alexandru M. Morega., Dr. Alin A. Dobre, and Dr.(c) Yelda Veli for hosting and welcoming me in their laboratory at the *Universitatea Politehnica din București* (UPB). They were very pleasant and fruitful discussions.

I would like to show my gratitude to the engineer Israel González, from the *Grupo MADIVER SA de CV*, for his advises and feedbacks during the calorimeter's manufacture; and to the engineer J. Andrés Ortega-Contreras and Dr. J. Amparo Andrade-Lucio, for their valuable assistance during the calorimeter's instrumentation.

Finally, my last, but not the least, acknowledge is to the Nopal's recreation centre and its owner, *Don George*, for their valuable help in stressful days (and nights).



## Resumen

Las necesidades digitales del mundo en cuanto a dispositivos electrónicos robustos, más pequeños y más rápidos aumentan rápidamente en la actual *Era de la Información*. Por lo que, el bien conocido problema de transferencia de calor en electrónica sigue vigente desde la aparición de los circuitos integrados, y aún se considera como un problema abierto. En la mayoría de los casos prácticos, sin embargo, éste permanece parcialmente desatendido por especialistas y estudiantes relacionados con la electrónica debido a múltiples razones. Este trabajo presenta una nueva alternativa para la gestión térmica en microelectrónica, que implica, simultáneamente, el procedimiento de diseño óptimo para disipadores de calor basado en la segunda ley de la termodinámica y utilizando métodos modernos de optimización; y la medición de la potencia térmica de los dispositivos microelectrónicos empleando el prototipo de un calorímetro no-convencional. Este último fue propuesto, diseñado, construido y analizado en este trabajo de investigación.

## Résumé

Les nécessités numériques du monde en appareils électroniques robustes, plus petits et plus rapides augmentent rapidement à *l'Ère de l'Information*. Donc, le problème bien connu de gestion thermique en l'électronique reste valable depuis l'apparition de circuits intégrés, et est considéré comme un problème ouvert aujourd'hui. Dans la plupart des cas pratiques, cependant, ce reste partiellement sans attention pour les spécialistes et les étudiants en l'électronique pour plusieurs raisons. Ce travail présente une nouvelle alternative pour la gestion thermique en microélectronique, qui implique, simultanément, la procédure de désigne optimale pour les dissipateurs thermiques basée sur la deuxième loi de la thermodynamique et les méthodes d'optimisation modernes; et la mesure de la puissance thermique de la microélectronique en utilisant le prototype d'un calorimètre non conventionnel. Ce dernier a été proposé, conçu, construit et analysé dans ce travail de recherche.

## Abstract

The world's digital necessities of robust, smaller and faster electronic devices rapidly increase on the current *Information Age*. Hereto, the well-known electronic thermal management problem stills valid since Integrated Circuits appeared, and it is considered as an open problem yet. In most practical cases, however, it remains partially unattended by electronic-related specialists and students due to multiple reasons. This work presents a new alternative for the thermal management in microelectronics, which involves, simultaneously, the optimal design procedure for heat sinks based in the second law of thermodynamics and modern optimisation methods; and the microelectronics's heat power measurement by using the prototype of a non-conventional calorimeter. The latter was proposed, design, built and analysed in this research work.

# Contents

<b>1</b>	<b>Introduction</b>	<b>1</b>
<b>2</b>	<b>Heat Sinks</b>	<b>5</b>
2.1	Foundations . . . . .	7
2.1.1	Operating conditions . . . . .	7
2.1.2	Mathematical models . . . . .	8
2.1.3	Heat transfer problems . . . . .	11
2.2	Modern optimisation methods . . . . .	15
2.2.1	Unified Particle Swarm Optimisation . . . . .	15
2.2.2	Cuckoo Search . . . . .	16
2.2.3	Deterministic Spiral Optimisation Algorithm . . . . .	17
2.2.4	Stochastic Spiral Optimisation Algorithm . . . . .	17
2.3	Methodology . . . . .	19
2.4	Results and discussion . . . . .	21
2.4.1	Optimisation algorithm's tuning . . . . .	21
2.4.2	Case 1: Al-RMCHS with air & NH <sub>3</sub> . . . . .	21
2.4.3	Case 2: HTCG-RMCHS with air, NH <sub>3</sub> & H <sub>2</sub> O-TiO <sub>2</sub> . . . . .	23
2.4.4	Case 3: HTCG-RMCHS with H <sub>2</sub> O-Al & H <sub>2</sub> O-TiO <sub>2</sub> . . . . .	28
2.4.5	Case 4: Al- & HTCG-RMCHS with air & NH <sub>3</sub> . . . . .	31
2.5	Conclusions . . . . .	35
<b>3</b>	<b>Non-Conventional Calorimeter</b>	<b>37</b>
3.1	Foundations . . . . .	39
3.2	Design and construction . . . . .	42
3.3	Numerical simulation . . . . .	50
3.3.1	Mathematical model . . . . .	50
3.3.2	Methodology . . . . .	54
3.3.3	Results and discussion . . . . .	54
3.4	Experimental implementation . . . . .	65
3.4.1	Methodology . . . . .	65
3.4.2	Results and discussion . . . . .	66
3.5	Conclusions . . . . .	71
<b>4</b>	<b>Summary</b>	<b>73</b>
4.1	Future works . . . . .	73
4.2	Scientific production . . . . .	74

# List of Figures

2.1	Electronic cooling system to be analysed . . . . .	7
2.2	Direct and inverse heat transfer problems . . . . .	14
2.3	Optimal features achieved in the Case 1 . . . . .	23
2.4	Relative distribution of the optimal thermal resistances . . . . .	23
2.5	$\dot{S}_{gen,min}$ varying $G_{wf}$ and $\phi$ values . . . . .	24
2.6	Optimal features achieved in the Case 2 . . . . .	25
2.7	Optimal desing variables achieved in the Case 2 . . . . .	26
2.8	Min. entropy production varying nanoparticles' concentration in the Case 2 . . . . .	28
2.9	Minimal entropy production achieved in the Case 3 . . . . .	29
2.10	Optimal dimensionless correlation found in the Case 3 . . . . .	30
2.11	Optimal thermal resistance obtained in the Case 3 . . . . .	30
2.12	Optimal features found in the Case 3 . . . . .	31
2.13	Optimal design variables found in the Case 4 . . . . .	32
2.14	Minimal entropy production and its features obtained in the Case 4 . . . . .	33
2.15	Measured and estimated temperatures by varying the power in the Case 4 . . . . .	34
2.16	Film heat transfer coefficient estimated in the Case 4 . . . . .	34
3.1	System's Sketches . . . . .	39
3.2	Calorimeter's exploded view . . . . .	42
3.3	Enclosure's geometry . . . . .	43
3.4	Coat's geometry . . . . .	44
3.5	Tank's geometry . . . . .	44
3.6	Main chamber's geometry . . . . .	45
3.7	Cover's geometry . . . . .	45
3.8	3D scaled prototype . . . . .	46
3.9	Manufactured parts . . . . .	46
3.10	Data flow's diagram . . . . .	48
3.11	Calorimeter's final state . . . . .	49
3.12	Computational domain of the studied system . . . . .	50
3.13	Boundary conditions of the computational domain . . . . .	53
3.14	Implemented mesh of the reduced system . . . . .	54
3.15	Velocity fields under stationary conditions . . . . .	55
3.16	Thermal behaviour under stationary conditions . . . . .	56
3.17	Temperature distributions under stationary conditions . . . . .	57
3.18	Temperature distribution along the studied edge under stationary conditions . . . . .	57
3.19	Temperatures differences at several locations under stationary conditions . . . . .	58
3.20	Temperature values at the bottom vertex (Case 1) . . . . .	59



3.21	Temperature values at the bottom vertex (Case 2) . . . . .	60
3.22	Comparison of temperature values from Cases 1 and 2 . . . . .	60
3.23	Temperature values at the bottom vertex (Case 3) . . . . .	61
3.24	Temperature values at the bottom vertex (Case 4) . . . . .	61
3.25	Comparison of temperature values from Cases 3 and 4 . . . . .	62
3.26	Temperature values at the bottom vertex (Case 4) in a short testing time .	63
3.27	Determined heat power from temperature values . . . . .	63
3.28	Temperature values at the bottom vertex varying nanoparticle concentration	64
3.29	Determined power from temperature values varying nanoparticle concentration	64
3.30	Results from three long time experiments using the calorimeter . . . . .	67
3.31	Fitted curves for the water's average measurements per experiment . . . . .	67
3.32	Calorimeter's characteristics . . . . .	68
3.33	Determination of heat power using two approaches . . . . .	69

# List of Tables

2.1	Values used for the parameters of the heat sink. . . . .	20
2.2	Thermophysical properties for RMCHS design . . . . .	20
2.3	Considered parameters for tuning the optimisation methods . . . . .	21
2.4	Resulting values for the algorithms' control parameters . . . . .	22
2.5	Sensitivity analysis for CS with the Beale function . . . . .	22
2.6	Optimal desings found in the Case 1 . . . . .	24
2.7	Optimal desings obtained in the Case 2 . . . . .	27
2.8	RMSE of estimated film coefficient . . . . .	32
3.1	Calorimeter's specifications . . . . .	47
3.2	Temperature sensor's specifications . . . . .	47
3.3	Miniomputer's specifications . . . . .	48
3.4	Thermophysical properties of materials used in this work. . . . .	51
3.5	Assumed values for some parameters . . . . .	55
3.6	Cases studied in time dependent analyses . . . . .	55
3.7	Temperature measurements varying the total power . . . . .	58
3.8	Equivalent thermal resistances obtained in different points . . . . .	58
3.9	Power values considered for the experimental implementation . . . . .	65
3.10	Fitted data from the characterisation's results . . . . .	68
3.11	Determined heat power from several experiments varying the power source. . . . .	70

# Chapter 1

## Introduction

Scientific and industrial communities are focussed on new materials, devices, architectures, designs, and manufacturing processes for microelectronic systems to fulfil the world's digital necessities on this *Information Age*. Since the transistor's invention, humanity has observed how vacuum tube apparatuses preceded shrunk and enhanced systems, *e.g.*, Integrated Circuits (IC), Multi-Chip Modules (MCM) and, most recent, System-in-Package (SiP) components. Some enricher reads about microelectronics' history can be found in [1–7]. Nowadays, SiPs are part of a global innovation plan, called Heterogeneous Integration Roadmap (HIR), which is leading by different researcher's societies [8]. HIR aims to pursue industrial and scientific advances of silicon technologies, according to the well-known Moore's Law, looking for initiate a new age with, for example, connectivity and network platforms, Internet of Everything (IoE), Smart Devices, Cloud Data, Intelligent Automation and Autonomous Vehicles [9, 10]. However, for any silicon-based device, shrinking devices (miniaturisation), augmenting integration level and increasing operative clock-rates lead thermal repercussions, namely the so-called Joule's effect. This energetic interaction is impossible to avoid due heat transfer is inherent for practical physical systems, including microelectronic components [11–13]. Thus, the heat transfer is one of the important technical limitations, because microelectronic devices have a maximum operating temperature specified by their designers and manufacturers. It is well-known as the Electronic Thermal Management Problem, which has increased interest since ICs appeared (about 1960s) with their Medium-Scale-Integration (MSI) and further technologies [14–17]. The need for thermal management is justified and overviewed by Thammanna and Srivastav in [18], where they declare that heat fluxes of Very-Large-Scale-Integration (VLSI) electronic devices and the surface of a vehicle re-entering to the Earth's atmosphere, are almost the same. Hereto, thermal management in microelectronic components is a well-known problem for electronic designers, engineers or technicians. It is an open problem and the literature has plenty of documents that show different solving approaches [19–30]. Although, in most practical cases, this problem remains partially attended by electronic specialists and engineering students due to uncountable reasons. One of these could be related to an apparent lack of thermal science skills.

A solution still used in our days consists on implementing heat sinks, or fin arrays, attached to or embedded in the electronic components for enhance their rate and capability of thermal power dissipation [25, 31–35]. Numerous interesting works have been appearing aimed at the performance improvement of heat sinks, some of them are described as follows by using an observation window of ten years. Various researchers have employed gaseous working fluids for enhance thermodynamic properties, such as thermal conductivity and



heat capacity, taking care of negative environmental impacts [36–40]; others have used pure liquids as coolers with formidable thermal conductivities to improve film coefficients [41–49]; withal, several authors have mixed liquid fluids with additives to boost their properties avoiding a considerable increment of pumping work [50–59]. Furthermore, designers have explored geometrical variations (mainly in the heat sink cross-section) looking for expand the channels hydraulic diameter, which increases the Reynold’s number and, thus, leads the working fluid flow to turbulent regime [60–66]; others have studied the roughness of heat sink walls, for augment thermal coefficients and avoid the slip flow condition, with the rise of fluid–surface friction as side-effect [66, 67]. In the same manner, alternative materials have been explored to build heat sinking devices, showing thermal conductivities greater than aluminium or copper, which are traditionally employed on this application [68–74]. Unfortunately, these non-common materials still are considerably expensive for conventional uses.

Although, these mechanical solutions are effectively implemented on microelectronic devices with the previous knowledge of their thermal behaviours. In other words, the specific electronic power losses quantification gives designers information to optimally implement any thermal management mechanism. Measurement of electronic power losses, say net heat transfer power generation, is considered into design thermal management solutions for specific cases. In the literature exists multiple paths to accurately modelling the thermal behaviour of several engineering systems. For the case of electrical and electronic components, these strategies are categorised in two groups: *the electrical* and *the calorimetric methods* [75, 76]. A trade-off between results accuracy and implementation difficulty have been identified for these strategies. That is, the former method has results with high uncertainty but it is considerably easy to implement; conversely, the latter one has great accuracy with an associated high implementation complexity [77]. The electrical method founds on the estimation of power losses by employing electrical measured variables such as current and voltage. For example, the power that an analog device dissipates can be easily related to the electrical power definition, *i.e.*,  $P_e = V_e I_e$  [W], since  $V_e$  [V] is voltage and  $I_e$  [A] is current. In the case of electronic devices, digital signals and sampling frequency play an important role on the power estimation, hence the aforementioned formula is slightly modified. Other cases of sophisticated signals and systems, specialised power formulae are needed to ensure an accurate estimation. Besides, *the calorimetric method* consists on the directly determination of the power losses from a specific system [78]. It is a well-settled area in practical applications of biology and chemistry [79, 80]. Calorimetry principle is based on estimation of the heat transferred to a characterised substance, inciting changes in its measurable state variables. This heat transfer is due to a natural process, *e.g.*, biological, chemical, or physical processes. Likewise, notions of thermodynamics and heat transfer are required to implement this strategy. Thus, a *calorimeter* is chiefly composed by the system under test and the characterised substance, which are connected by a thermal conductive interface and inside a properly insulation coat. The substance is commonly a fluid, which could be in motion through the system [76], or stagnation inside a reservoir or cavity as an energy storage cell [81]. Both setups can be grouped utilising the thermodynamic definition of a system, *i.e.*, open and closed systems. In addition, the *double-jacketed calorimeters* constitute an special case of the closed type, which enhance accuracy and performance of an open type calorimeter by enclosing its surroundings in a closed system [75]. Thereby, the power dissipation can be obtained from a simple enthalpy analysis for systems. Multiple implementations of calorimeters are eager to be found in literature, however, calorimeters using fluid flows are in the spotlight. It is mainly because

their response time is shorter than the one of closed system. A downside of this feature is the required additional pumping power to move the fluid throughout heat exchangers. Some examples of calorimetric systems are presented as follows. Blaabjerg *et al.* in 2002 built and tested a measuring system for electrical devices with power losses till 50 W [82]. Once they improved the calorimeter accuracy, they proposed a higher power capabilities system for industrial and home devices. One year later, Malliband *et al.* enhanced the accuracy of a double-jacketed closed-type calorimeter for components from 0.5 to 200 W [83]. In this study the design was verified by quantifying the losses of an inverter at different switching frequencies. In 2010, Weier *et al.* implemented a calorimeter on the heat transfer estimation of phone chargers and lamp ballasts, with an accuracy of  $\pm 0.1$  W in 25 W. Results were compared against values from an oscilloscope [84]. In the same year, Christen *et al.* presented a calorimetry-based system for the measurement of losses in a power converter system [85]. They remarked their double-jacketed chamber calorimeter was capable to determine power losses from 10 to 200 W, with a deviation less than  $\pm 0.4$  W. This apparatus showed a special immunity to electromagnetic interference phase errors, commonly perceived in AC systems. More recently, Frost and Howey constructed a high-speed calorimeter for electronic elements operating at high clock frequencies. This device was capable of reach the steady state in less than 10 min using coolers based on Peltier's elements [86]. In addition, it was tuned by an artificial neuronal network and showed an accuracy of  $\pm 8$  mW for components with power losses from 0.1 to 5 W. The before mentioned calorimeters have been successfully implemented to determine the net heat transfer of electrical and electronic components with different sizes, power consumption and operating frequencies. These systems employed a common scheme, which includes insulated chambers and heat exchangers, to estimate heat power generation from variations on the temperature in a flowing coolant. However, Marin *et al.* in 2012 built a closed-calorimeter for small microelectronic circuits, with the immersion of the test chamber in a reservoir of distilled water [81]. The fluid filling the reservoir was homogenised by mixing with a mechanical system of a paddle-wheel. The authors claim an accuracy of  $0.03$  °C for components with a heat generation of 25 W, reaching the steady state in 43 min.

However, majority of the reported works of calorimetric systems have avoided a thermal behaviour analysis. Notwithstanding, Blaabjerg *et al.* in [82] analysed temperature distribution of the calorimeter using thermographic pictures. It was carried out to place the sensors where average temperature on the surface area remains. Weier *et al.* in [84] performed a numerical simulation of their measuring system using to obtain the temperature distribution of conducting walls. Authors implemented a spherical *device under test* (DUT), with a constant power generation, which emulated an unknown electronic device. As a result, they were able to located appropriately the heat exchanger for water circulation to quantify power losses. Lastly, Frost and Howey tackled a thermal simulation of their device using a three-dimensional model in a commercial software to determine the system's performance [86].

On the other hand, numerical simulations are considered as an alternative and powerful area, which help scientific research and implementations to approach relatively complex processes. Some of these procedures recurrently involve multiphysical phenomena or formulae hard to solve analytically. Thus, numerical simulations have been widely used to solve problems on several areas of knowledge; *e.g.*, to solve heat-functions and optimise a laminar forced convection heat transfer process of pin-fins and plate-fins [87, 88]; to maximise the thermal conductance between the plate and fluid flow in a pin-fin heat sink with impinging flow [89]; to verify a design based on the constructal law for a photo-

voltaic cell resistance minimisation [90]; to corroborate experimental data obtained from a low power single-phased transformer, which is cooled by a ferrofluid in a natural convection process [91]; to design NbTi superconducting solenoid magnet of 5 T cooled by a Gifford–McMahon closed-cycle cryocooler [92]; to solve a direct problem of the *in-situ* electrical resistivity thermography of concrete structures [93]; to design micro-actuators for micro-electromechanical systems (MEMs) [94]; and to design miniature devices, like micro-structured planar spiral power transformer, for chip-embedded core applications [95]. Moreover, some numerical studies have been focused on biomedical applications, for example, to solve the direct problem of thoracic electrical bio-impedance using electrocardiometry [96]; to analyse the thermal behaviour of an anatomic region that contains a tumour for eventual oncologic diagnoses [97]; to improve microwaves applicators for cancer treatments studies [98]; and to study the transport problem for different kind of drug molecules by using iontophoresis or an adaptive magnetic field source [99].

This research report proposes a new alternative for microelectronic thermal management, which involves, simultaneously, the optimal design procedure for heat sinks build with high thermally conductive materials, and the electronics's heat power measurement by using a non-conventional calorimeter. This optimal designing methodology is founded in the second law of thermodynamics and modern optimisation methods, and analysed under multiples scenarios. Afterwards, the non-conventional calorimeter's prototype is designed and analysed for obtaining information about the thermal power generated by an electronic device, which eventually shall be used into the proposed designing strategy. In this way, the present work's results contribute to the central research topic due to the current technology state, since energy dissipation is due to resistive heating, with an alternative methodology for the thermal management problem of microelectronic components.

This document is organised as follows. Second chapter details the optimal designing methodology for heat sinks and its numerous illustrative examples. Third chapter describes the non-conventional calorimetry since its design, numerical simulation and experimental implementation. Finally, Fourth chapter summarises the most relevant inferences of the entire document.



# Chapter 2

## Heat Sinks

### Introduction

Microelectronic cooling is a well-known problem for electronic designers and engineers. Many approaches have appeared aimed to research this kind of problem, *e.g.*, heat sinks, heat pipes, and thermoelectric coolers [33]; and their selection depends mainly on net thermal power and geometrical constraints of the microelectronic device. However, cooling systems fulfil the thermal requirements but exhibit a non-optimal performance, *i.e.*, they destroy exergy (useful work) or threat the environment. A particularly recurrent, and simple, solution for components with high thermal fluxes is to attach or embed Microchannel Heat Sinks (MCHSs) [100]. Tuckerman and Pease demonstrated this early in 1981, and they studied rectangular Microchannel Heat Sinks (RMCHSs) for very-large-scale integration (VLSI) devices [101]. Nowadays, MCHSs are an important part of the practical implementation of electronic devices in general.

MCHSs have been continuously improved to fulfil necessities of evolving microelectronic components by using numerous passive mechanisms [34]. One of the explored approaches considers different geometries for micro- and mini-channels, and some examples include multiple layers, constricted segments, wavy structures, inner roughness patterns and porous media [69, 102–105]. Other approaches focus on using manufacturing materials with excellent thermophysical properties, *e.g.*, aluminium, copper and graphite composites [105, 106]. Likewise, alternative multiphase fluids have been implemented as coolants, such as colloids with nanoparticles of, for example, copper oxide (CuO), titanium dioxide (TiO<sub>2</sub>), silicon carbide (SiC) and aluminium oxide (Al<sub>2</sub>O<sub>3</sub>) [105, 107]. Even so, most passive enhancement mechanisms for MCHSs could be considered harder to implement in most practical scenarios, where certain constraints exist, namely the excessive manufacturing and operating costs. But, passive improvements on structure, manufacturing material, and coolant are possible when the complete system has been previously designed to maximise its thermal performance. A conceptual design allows reaching a desired cooling system, on a given set of operating conditions and specifications, and these schemes are commonly integrated and solved as an optimisation problem. In the case of MCHSs, the design methodologies use different performance related to the figures-of-merit. The traditional method considers the equivalent thermal resistance model of all heat transfer phenomena involved on the operating cooling system [108]. Others consider the total pressure drop as an additional objective, giving place to a multi-objective optimisation problem [109]. Another strategy implements thermodynamic concepts to state a mono-objective multi-physics optimisation

problem, *i.e.*, the entropy generation minimisation (EGM) criterion.

EGM focuses on balancing entropy to obtain a model of irreversibilities in an operating system, which is subsequently minimised. This criterion was pioneered by Bejan [87], and employed in heat sinks for the first time by Culham and Muzychka [110]. It has been broadly applied for designing engineering systems as well as electronic cooling devices [105, 111]. Conversely, RMCHSs have a simple geometry that makes them relatively easy to manufacture in an unsophisticated laboratory. Thus, several works have been focused on improving RMCHSs performance [38, 105]. Some have studied and designed implementing the EGM powered with traditional gradient-based optimisation techniques, assuming flowing coolants in the laminar regime [111–113]. On the other hand, traditional optimisers for thermodynamic conceptual design applications usually require specialised computing platforms, to solve or simulate the associated highly non-linear problems. However, modern optimisation algorithms have shown good-enough capabilities to satisfy EGM requirements. These techniques, also known as evolutionary algorithms, feature versatility, flexibility and precision [114, 115]. For example, Simulated Annealing (SA), Genetic Algorithms (GA), Unified Particle Swarm Optimisation (UPSO), Deterministic Spiral Optimisation Algorithm (DSOA), Harmony Search (HS) and Cuckoo Search (CS) have been implemented as solvers of EGM for designing RMCHSs [40, 116–119]. The latter optimisation algorithm, *i.e.*, CS, has shown greater potential on solving applied engineering problems [120]. Nevertheless, literature lacks works regarding to EGM criterion for designing RMCHSs that include colloidal coolants, and also considering both laminar and turbulent hydrodynamic regimes, by using modern optimisation.

This chapter presents the alternative methodology of thermodynamic optimisation, based on the EGM criterion and the modern optimisation algorithm (*i.e.*, UPSO, CS and DSOA), for the conceptual design of RMCHSs for microelectronic cooling applications. Multiples illustrative examples are detailed and studied, varying the manufacturing materials, design specifications and operating conditions. The chapter's content is organised as follows: First section displays the foundations and key concepts related with the methodology, as well as the utilised heat sink model and its associated heat transfer problems. Second section describes the implemented modern optimisation algorithms. Next, Methodology carried out is specified in section three and, the achieved results are detailed in section four. At the end, Conclusions are summarised.

## 2.1 Foundations

This section details the attained three mathematical models for a microchannel heat sink, in steady-state operation, as a common solution for the electronic management problem. These models are based on concepts of the entropy generation rate ( $\dot{S}_{gen}$  [W/K]), the equivalent thermal resistance ( $R_{eq}$  [K/W]) and the pressure drop ( $\Delta P$  [Pa]). First, the assumed operating conditions and constraints are described, and then mentioned formulae are deduced. For simplicity, a rectangular geometry for channels is considered, but models can be extended for other geometries with ease.

### 2.1.1 Operating conditions

Figure 2.1 presents the conceptual system to be analysed, *i.e.*, a RMCHS, as well as its inlet and outlet supply ducts [116]. RMCHSs have a total volume determined as

$$V_{hs} = W_{hs}L_{hs}(H_c + t_b + t_t), \quad (2.1)$$

where  $W_{hs}$  [m] and  $L_{hs}$  [m] are the total width and length (respectively),  $H_c$  [m] is the height of channels. Furthermore,  $t_b$  [m] and  $t_t$  [m] are the thickness of bottom and top parallel plates. The number of channels of an RMCHS is given by

$$N_c = \frac{W_{hs}/2 - w_p}{w_c + w_p}, \quad (2.2)$$

where  $W_{hs}/2$ ,  $w_c$ , and  $w_p$  [m] are the heat sink, channels and walls' half widths.

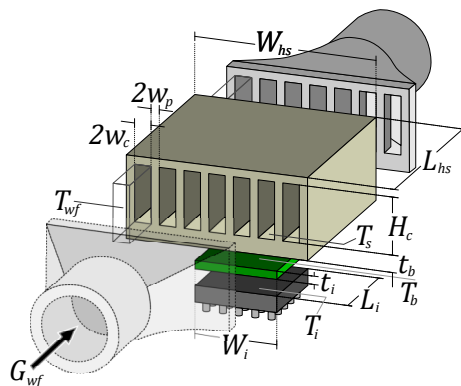


Figure 2.1. Electronic cooling system to be analysed: rectangular microchannel heat sink, thermal interface, and fluid flow supply pipes.

The mechanical component is attached to the bottom plate of the microelectronic device using a thermal paste. This interface has thickness  $t_i$ , and its effective area for heat transfer is  $A_i$  ( $= W_i L_i$ ) [m<sup>2</sup>]. At most,  $A_i$  equals the effective area of the heat sink base,  $A_b$  ( $= W_{hs} L_{hs}$ ) [m<sup>2</sup>], *i.e.*,  $A_i \leq A_b$ . Regarding, thermophysical properties, pastes are commonly presented in terms of thermal resistance times unit area,  $R_i A_i$  ( $= t_i/k_i$ ) [K·m<sup>2</sup>/W]. The system is made whole by the supply pipes, which have a length of  $L_{tu}$  [m] and an inner diameter of  $D_{tu}$  [m] [34].

The operating conditions to model, and eventually, optimise the system in Figure 2.1, based on reported works [121, 122], are defined as follows:

- Material, fluid and geometry conditions:

- Heat sink and interface’s materials are macroscopically isotropic and excellent thermal conductors.
  - Roughness of the channels’ inner walls and its related phenomena are disregarded, such as rarefied gas dynamics for gaseous coolants.
  - Heat sink base area is at least equal to the chip’s effective heat transfer area, and the chip’s and interface’s areas must be equal.
  - Working fluid’s mean free path is considered much less than the channels’ hydraulic diameter.
  - Coolant’s average thermophysical properties are considered constant inside the heat sink’s channels.
- Heat transfer and fluid motion conditions:
    - Thermal power generated by the microelectronic device is completely transferred to the coolant through the heat sink, via forced convection.
    - Generated heat flux is considered uniform and steady.
    - Heat transfer flux, from the chip’s effective surface, passes through the interface’s body and enters straight to the heat sinks by its bottom plate.
    - Thermal spread and contraction effects are considered since heat flows travel from one body to another with different cross-section area.
    - Changes in the kinetic and potential energies, heat transfer due to thermal radiation, and power’s leakages to the surroundings are neglected.
    - Coolant flow is assumed to be in a hydrodynamically completely developed regime, such as laminar and turbulent. The transition regime is disregarded.

### 2.1.2 Mathematical models

EGM criterion consists of analysing processes in any engineering system by employing classical thermodynamic concepts, such as: the mass flow conservation,

$$\left( \sum_i \dot{m}_i \right)_{in} - \left( \sum_j \dot{m}_j \right)_{out} = \left( \frac{\partial m}{\partial t} \right)_{sys}, \quad (2.3)$$

the first law of thermodynamics,

$$\left( \sum_i \dot{E}_i \right)_{in} - \left( \sum_j \dot{E}_j \right)_{out} = \left( \frac{\partial E}{\partial t} \right)_{sys}, \quad (2.4)$$

and second law of thermodynamics,

$$\left( \sum_i \dot{S}_i \right)_{in} - \left( \sum_j \dot{S}_j \right)_{out} + \dot{S}_{gen} = \left( \frac{\partial S}{\partial t} \right)_{sys}. \quad (2.5)$$

These expressions must be rewritten to describe the operating heat sink by applying the described conditions. Hence, mass transfer balance from (2.3) yields

$$(\rho_{wf} G_{wf})_{in} = (\rho_{wf} G_{wf})_{out} = (\rho_{wf} G_{wf})_{hs}, \quad (2.6)$$

where the mass transfer rate ( $\dot{m}$  [kg/s]) is calculated with the average density ( $\rho_{wf}$  [kg/m<sup>3</sup>]) and the volume flow rate ( $G_{wf}$  [m<sup>3</sup>/s]) of the working fluid. Subscript “*hs*” is used instead “*sys*” to clarify that the analysed system is a heat sink. Subsequently, the energy balance from (2.4) becomes

$$\dot{Q}_{hs} = (\rho_{wf} G_{wf})_{hs} \Delta h, \quad (2.7)$$

since  $\dot{Q}_{hs}$  [W] is the heat transfer rate entering to the heat sink, and  $\Delta h$  [J/kg] is the coolant’s specific enthalpy change. Likewise, the entropy balance in (2.5) gives

$$\frac{\dot{Q}_{hs}}{T_i} + \dot{S}_{gen} = (\rho_{wf} G_{wf})_{hs} \Delta s, \quad (2.8)$$

with  $T_i$  [K] as the boundary’s temperature where the thermal power ( $\dot{Q}_{hs}$ ) enters to the system, *i.e.*, the interface’s temperature,  $\dot{S}_{gen}$  [W/K] as the entropy generation rate due process’s irreversibilities, and  $\Delta s$  [W/kg·K] as the working fluid’s entropy change.

Additionally, it is required the second Gibbs’s equation,

$$\Delta h = T_a \Delta s - \frac{1}{\rho_{wf}} \Delta P, \quad (2.9)$$

to correlate the three previous expressions. Therefore, a function for the heat sink’s entropy generation rate is obtained by performing simple algebraic procedures, as shown,

$$\dot{S}_{gen} = \left( \frac{\Delta T}{T_i} \right) \frac{\dot{Q}_{hs}}{T_a} + \left( \frac{G_{wf}}{T_a} \right) \Delta P \quad (2.10)$$

since  $\Delta P$  [Pa] is the total pressure drop of the flowing coolant,  $T_a$  [K] is the surroundings’ temperature, and  $\Delta T = T_i - T_a$  is the temperatures difference between interface and ambient. The first and second right-hand side (RHS) terms of (2.10) are the entropy generation rate due to the heat transfer and fluid flow, respectively. However, it is possible to express the thermal irreversibilities in terms of the system’s geometry using the lumped circuit model, *i.e.*, by finding the equivalent thermal resistance to model the system ( $R_{eq} = \Delta T / \dot{Q}_{hs}$  [K/W]). Thus, the entropy production in (2.10) is rewritten as,

$$\dot{S}_{gen} = \left( \frac{\dot{Q}_{hs}^2}{T_a} \right) \frac{R_{eq}}{T_i} + \left( \frac{G_{wf}}{T_a} \right) \Delta P. \quad (2.11)$$

This expression, as a process performance quantification, is directly related to several transport phenomena, but heat transfer and fluid flow are chiefly involved on microelectronic cooling processes. Summarising, the first term of  $\dot{S}_{gen}$  depends of the net thermal power generated by the chip ( $\dot{Q}_{hs}$  [W]), of the equivalent thermal resistance of the heat sink ( $R_{eq}$  [K/W]), and of the average chip ( $T_i$  [K]) and surrounding ( $T_a$  [K]) temperatures. Likewise, the second term includes the net volume flow rate of the working fluid ( $G_{wf}$  [m<sup>3</sup>/s]), and the total pressure drop of the system ( $\Delta P$  [Pa]). Hence, to properly model a microchannel heat sink  $R_{eq}$  and  $\Delta P$  must be determined via either modelling or measuring. Other parameters such as  $T_a$ ,  $T_i$ ,  $G_{wf}$  and  $\dot{Q}_{hs}$  can be approached or measured from the setup conditions. Nonetheless, approximations for  $\dot{Q}_{hs}$  usually are very variant in practical applications. Therefore, it is assumed that  $T_a$ ,  $T_i$ ,  $G_{wf}$  and  $\dot{Q}_{hs}$  are known and,  $R_{eq}$  and  $\Delta P$  are obtained from a conceptual modelling process for a rectangular microchannel heat sink.

The model for the equivalent thermal resistance is obtained by considering heat transfer mechanisms for the heat flux throughout the system, as

$$R_{eq} = R_i + R_b + R_p + R_h + R_f, \quad (2.12)$$

where  $R_i, R_b, R_p, R_h$  and  $R_f$  are thermal resistances due to conduction at the interface, spreading in the base, constriction at the walls, convection at the inner walls of the channels, and calorific capacity of the coolant, respectively. The equivalent thermal resistance in (2.12) is rewritten in (2.13) based on models and concepts from reported works [106, 123]. RHS terms of (2.13) are ordered to match with the ones from (2.12).

$$R_{eq} = \frac{t_i}{k_i W_i L_i} + \frac{1}{k_{hs} \sqrt{W_i L_i}} \left( \frac{\varepsilon \tau}{\sqrt{\pi}} + \frac{\Phi_b}{2} (1 - \varepsilon)^{1.5} \right) + \frac{2(w_p + w_c)}{\pi k_{hs} W_{hs} L_{hs}} \cdot \ln \left[ \csc \left( \frac{\pi w_p}{2(w_p + w_c)} \right) \right] + \frac{1}{2\bar{h} N_c L_{hs} (w_c + \eta_p H_c)} + \frac{1}{\rho_{wf} G_{wf} c_{wf}}. \quad (2.13)$$

Hence, a more realistic model of the equivalent thermal resistance of microchannel heat sink ( $R_{eq}$  [K/W]) is obtained via (2.13). This expression depends on thickness ( $t_i$  [m]), thermal conductivity ( $k_i$  [W/m·K]) and effective area ( $W_i L_i$  [m<sup>2</sup>]) of the thermal paste; thermal conductivity ( $k_{hs}$  [W/m·K]), effective area at the bottom ( $W_{hs} L_{hs}$  [m<sup>2</sup>]), number of channels ( $N_c$ ), length ( $L_{hs}$  [m]) of the heat sink; and average density ( $\rho_{wf}$  [kg/m<sup>3</sup>]), volume flow rate ( $G_{wf}$  [m<sup>3</sup>/s]) and average specific heat capacity ( $c_{wf}$  [J/kg·K]) of the working fluid. Additionally, some parameters are required, such as the dimensionless heat source radius ( $\varepsilon$ ), the plate thickness ( $\tau$ ), and the correlation ( $\Phi_b$ ). Furthermore, it is important to know the average convective heat transfer coefficient ( $\bar{h}$  [W/m<sup>2</sup>·K]), which is correlated with the Nusselt's number ( $Nu_{D_h}$ ),

$$\bar{h} = Nu_{D_h} \frac{k_{wf}}{D_h}, \quad (2.14)$$

where  $D_h$  [m] is the hydraulic diameter and  $k_{wf}$  is the thermal conductivity of the working fluid. Nusselt's number is approached using (2.15) for a laminar and turbulent fluid flow regime, in accordance to the considered operating conditions and by applying the Reynolds's number ( $Re_{D_h}$ ) as selection criterion [40, 116, 124]. Correlations for  $Nu_{D_h}$  depend on parameters such as Prandtl's number ( $Pr$ ), kinematic viscosity ( $\nu_{wf}$  [m<sup>2</sup>/s]) and average bulk velocity ( $\bar{V}_{wf}$  [m/s]) of the coolant, as well as Darcy's friction factor of channels ( $f_c$ ).

$$Nu_{D_h} = \begin{cases} 2.253 + 8.164(1 + \alpha)^{-3/2}, & \text{if } Re_{D_h} \leq 2300, \\ \frac{(f_c/2)(Re_{D_h} - 1000)Pr}{1 + 12.7\sqrt{f_c/2}(Pr^{2/3} - 1)}, & \text{if } Re_{D_h} > 2300. \end{cases} \quad (2.15)$$

Similarly, the factor  $f_c$  depends of the hydrodynamic behaviour of the fluid flow. Hence, empirical correlations for  $f_c$  are given in (2.16), based on [125].

$$f_c = \begin{cases} Re_{D_h}^{-1} (C_1^{1.14} + C_2^2)^{0.5}, & \text{if } Re_{D_h} \leq 2300, \\ (0.79 \ln(Re_{D_h} - 1.64))^2, & \text{if } Re_{D_h} > 2300. \end{cases} \quad (2.16)$$

$$C_1 = 7.6953 Re_{D_h} D_h / L_{hs}, \quad \text{and} \quad C_2 = 24.34 - 39.28\alpha / (\alpha + 1)^2. \quad (2.17)$$

Moreover, total pressure drop ( $\Delta P$ ) of the system, in the entropy production model at (2.12), is determined as the sum of pressure drops due to the coolant flowing through

the supply tubes, and through the heat sink's channels.  $\Delta P$  can be obtained using (2.18), with  $f_{tu}$  being the Darcy's friction factor of supply ducts shown in (2.20) [125, 126].

$$\Delta P = \rho_{wf} \left( \frac{\bar{V}_{wf}^2}{2} C_3 + 16 \left( \frac{G_{wf}}{\pi D_{tu}^2} \right)^2 C_4 \right), \quad (2.18)$$

$$\begin{aligned} C_3 &= f_c L_{hs} / D_h + 1.79 - 2.32 C_5 + 0.53 C_5^2, \\ C_4 &= f_{tu} L_{tu} / D_{tu} + 1.42 - 1.21 C_6^2 + C_6^4, \\ C_5 &= w_c / (w_c + w_p), \quad \text{and} \quad C_6 = \pi D_{tu}^2 / (4 W_{hs} H_c). \end{aligned} \quad (2.19)$$

$$f_{tu} = \left( 0.3716 + 4.0645 \frac{D_{tu}}{L_{tu}} \right) \left( \frac{\pi \nu_{wf} D_{tu}}{4 G_{wf}} \right)^{C_7}, \quad (2.20)$$

$$C_7 = 0.268 + 0.3193 D_{tu} / L_{tu}. \quad (2.21)$$

Finally, the entropy generation model describing the steady-state operating system in (2.11) is completely defined with (2.12)–(2.21). Nevertheless, it is important to consider approximations given by (2.22)–(2.25) to obtain the average thermophysical properties of the working fluid, when it is a nanofluid (or a colloid) [107]. In these equations,  $\phi$  is the nanoparticle volume concentration; and  $\rho$ ,  $k$ ,  $\nu$ , and  $c$  are the average density, thermal conductivity, kinematic viscosity, and specific heat, respectively, of the working fluid ( $wf$ ), of nanoparticles ( $np$ ) and of the base fluid ( $bf$ ),

$$\rho_{wf} = \phi \rho_{np} + (1 - \phi) \rho_{bf}, \quad (2.22)$$

$$k_{wf} = k_{bf} \left( \frac{k_{np} + 2k_{bf} - 2\rho_{wf}(k_{bf} - k_{np})}{k_{np} + 2k_{bf} + \phi(k_{bf} - k_{np})} \right), \quad (2.23)$$

$$\nu_{wf} = \nu_{bf} (1 + 2.5\phi), \quad (2.24)$$

$$c_{wf} = \rho_{wf}^{-1} (\phi \rho_{np} c_{np} + (1 - \phi) \rho_{bf} c_{bf}). \quad (2.25)$$

### 2.1.3 Heat transfer problems

Thermal management solutions aim to control, directly or indirectly, the electronic packages' temperature for avoiding any possible failure. This temperature depends of the heat flux dissipated by the chip during its operation. In the case of using cooling systems based, for example, in MCHS, either temperature or heat flux must be known to estimate the other one. In much cases heat transfer power is hard and expensive to measure, thus it is approximated through Joule's law and thermodynamics' first law. Hence, using an approach, many designers and engineers can model and improve the behaviour of MCHS-based electronic cooling systems, either by design or tune.

A steady-state heat transfer process of any thermal mechanism, as well as a microchannel heat sink (MCHS) structure, can be effectively approached through its equivalent thermal resistance ( $R_{eq}$  [W/K]), such as

$$\dot{Q}_{hs} = \frac{\Delta T}{R_{eq}}, \quad (2.26)$$

since  $\dot{Q}_{hs}$  [W] is the net heat transfer rate entering to the system, and  $\Delta T$  [K] is the finite difference of temperatures between the system isothermal boundary ( $T_i$  [K]) and its surroundings ( $T_a$  [K]) [122, 127, 128].  $\dot{Q}_{hs}$  and  $T_a$  are measurable quantities, which allow



engineers to make decisions or control their cooling system. Specifically, the rectangular microchannel heat sink's (RMCHS) performance is directly related with  $\Delta T$  behaviour in electronic thermal management applications, where the components must operate below a threshold temperature to avoid any failure. Thus, the finite difference of temperatures between the chip–heat sink interface ( $T_i$  [K]) and the ambient ( $T_a$  [K]) can be expressed as,

$$\Delta T = T_i - T_a = \dot{Q}_{hs} R_{eq}, \quad (2.27)$$

and  $R_{eq}$  is a lumped model, conformed by several heat transfer mechanisms in RMCHS, corresponding to (2.13). Although, the simplest model for  $R_{eq}$ , in many practical applications, is used as

$$R_{eq} = \frac{t_i}{k_i W_i L_i} + \frac{1}{\rho_{wf} G_{wf} c_{wf}}, \quad (2.28)$$

since right hand terms of (2.28) correspond to resistances due convection inside channels ( $R_h$ ), and calorific capacitance of the working fluid ( $R_f$ ), respectively. These two thermal mechanism cannot be disregarded, even in the most idealistic analysis. More details about the thermal resistance model are given above (Section 2.1.2).

Once design specifications, thermophysical properties and correlations are defined (Sections 2.1.1 and 2.1.2), the temperature difference  $\Delta T$  can be obtained by using (2.27) in a heat sinking application. Thus, let  $\underline{x}$  be a vector containing all required parameters to obtain  $\Delta T$ ,  $\Delta T(\underline{x}) : \mathbb{R}^D \rightarrow \mathbb{R}$ . There are infinite possible values for  $\underline{x}$ , but their selection depend on the practical application setup and engineer expertise. However, one can say  $\underline{x}$  is formed by two parameters' vectors,  $\underline{x} = (\underline{y}; \underline{z})$ , where  $\underline{y}$  are the known parameters from a practical specification set, *e.g.*, size constraints, fluid flow pumping power and net heat flux; and  $\underline{z}$  are the parameters subject to the expert knowledge, whose values can enhance or jeopardise the system performance, *e.g.*, geometry, kind of material, nanoparticle concentration and volume flow rate. As an illustrative example,  $\underline{y}$  and  $\underline{z}$  could be:

$$\begin{aligned} \underline{y} &= (W_{hs}, L_i, L_{hs}, H_c, \rho_{hs}, \rho_{wf}, k_{hs}, k_{wf}, c_{wf})^\top, \\ \underline{z} &= (w_c, w_p, \phi, G_{wf})^\top. \end{aligned}$$

Nevertheless, it is possible to reduce any uncertainty by finding, objectively, the best configuration for variables in  $\underline{z}$ , *i.e.*, their optimal values  $\underline{z}_*$ . This configuration can be reached through several conceptual schemes, such as an optimisation procedure

$$\underline{z}_* = \arg \min_{\underline{z}} \{f(\underline{x})|_{\underline{x}=(\underline{y}; \underline{z})}\} \quad (2.29)$$

since  $f(\underline{x})$  is the figure–of–merit or cost function, related with the system's performance. This function could be stated in different senses, say, *e.g.*, the equivalent thermal resistance  $R_{eq}(\underline{x})$  in (2.13), the total pressure drop  $\Delta P(\underline{x})$  in (2.18), and the entropy production  $\dot{S}_{gen}(\underline{x})$  in (2.11). For further reads, few suggested documents are [39, 129, 130]. Notwithstanding, a recurrent and powerful methodology for finding these parameters, based on the thermodynamics' second law, is the Entropy Generation Minimisation (EGM) criterion. The RMCHS model according to the total entropy production ( $\dot{S}_{gen}$  [W/K]), is obtained in (2.11), but it is rewritten in function of  $\underline{z}$  for a given  $\underline{y}$ , such as

$$\dot{S}_{gen}(\underline{z}) = \left[ \left( \frac{\dot{Q}_{hs}^2}{T_a} \right) \frac{R_{eq}(\underline{x})}{T_i(\underline{x})} + \left( \frac{G_{wf}}{T_a} \right) \Delta P(\underline{x}) \right]_{\underline{y}}, \quad (2.30)$$

where  $T_a$  and  $T_i$  are correlated through (2.26).

Besides, there are situations where the thermal management systems are already built but, evidently, its performance needs improvements. For that, the estimation of unknown quantities, in an implemented real system, is required. This problem, also known as Inverse Heat Transfer Problem (IHTP), have been widely studied in the literature [131–139]. They uses measurements from an experimental setup implementing the traditional Least Squared Error (LSE) criterion, which consists on minimising  $\varepsilon(\underline{z})$  [140], such as

$$\min_{\underline{z}} \{\varepsilon(\underline{z})\} = \min_{\underline{z}} \left\| \underline{T}_m - T(\underline{x})|_{\underline{y}} \right\|_2^2, \quad (2.31)$$

since  $\underline{T}_m$  [K] are the measurements of temperatures, and  $T(\underline{x})$  [K] are values calculated for the same temperature using a known functional form (or model), a set of known parameters  $\underline{y}$ , and a set of candidate values for the unknown parameters  $\underline{z}$ , with  $\underline{x} = (\underline{y}; \underline{z})$ .  $\|\cdot\|_2^2$  is the ordinary Euclidian 2–norm.

Finally, all the above mentioned about the electronic thermal management scenarios, based on a microchannel heat sink, is summarised in three following heat transfer problems, *i.e.*, design, direct, and inverse problems.

### Design heat transfer problem

In a given practical scenario for an electronic thermal management implementation, a design problem is stated looking for enhancing the system's performance. In this work, the metric of goodness is the entropy production rate ( $\dot{S}_{gen}$  from (2.30)), as it was defined above, which requires specifications ( $\underline{y}$ ), design variables ( $\underline{z}$ ) and constraints ( $\underline{z}_l$  and  $\underline{z}_u$ ). Hence, the conceptual design of a rectangular microchannel heat sink is given as shown,

$$\begin{aligned} \underline{z}_* &= \arg \min_{\underline{z}} \{ \dot{S}_{gen}(\underline{x})|_{\underline{y}} \}, \\ \text{s.t. } \underline{z}_l &\preceq \underline{z} \preceq \underline{z}_u. \end{aligned} \quad (2.32)$$

since  $\underline{x} = (\underline{y}; \underline{z})$  is the vector of all parameters required for evaluate the objective function.

### Direct heat transfer problem

The direct heat transfer problem (DHTP) is laid out with the objective of calculating the temperature in chip's surface, for a specific heat sinking process. It is assumed a uniform and homogeneous heat power dissipation, and other known parameters and constrictions given by  $\underline{x} = (\underline{y}; \underline{z})$ , which are evaluated in the mathematical model from (2.27), as follows,

$$T_i(\underline{x}) = T_a + \dot{Q}_{hs} R_{eq}(\underline{x}). \quad (2.33)$$

Parameters of  $\underline{x} = (\underline{y}; \underline{z})$  are obtained from a designing process for a given specifications and constraints, or simply they are defined by an expert.

### Inverse heat transfer problem

In contrast, the inverse heat transfer problem (IHTP) is laid out with the objective of estimating some parameter values of  $\underline{x}$ , which are unrelated to the design specifications  $\underline{y}$ ,

say,  $\underline{z}$  as a part of  $\underline{x} = (\underline{y}; \underline{z})$ . In a practical microchannel heat sinking scenario, where at least one temperature is measurable, it can be achieved by solving

$$\begin{aligned} \underline{z}_* &= \arg \min_{\underline{z}} \{ \varepsilon(\underline{x}) |_{\underline{y}} \}, \\ \text{s.t. } \underline{z}_l &\preceq \underline{z} \preceq \underline{z}_u, \end{aligned} \quad (2.34)$$

since  $\underline{y}$  and  $\underline{z}$  are sets of known and unknown parameters, respectively, where  $\underline{x} = (\underline{y}; \underline{z})$  is the vector of all parameters from the direct problem formulation. The set of values of  $\underline{z}$  for the experimental setup can be obtained from a conceptual design, or from previous knowledge of the direct problem solution.

### Summary

The main objective of an electronic thermal management problem is to avoid higher temperatures than temperatures' threshold. Once an electronic component has been chosen, its operative heat dissipation can be approached using data from the manufacturer; however, that approach can be refined with practical data. Thus, assuming the electronic's heat power is accurate enough, a cooling system can be implemented for measure and control temperatures at component's surface, by solving an associated direct heat transfer problem (DHTP). To solve a DHTP, a model for the cooling system is required. It is common that these cooling systems are designed for generic implementations, *e.g.*, the plate–fin heat sinks, but sometimes it is required designed systems for very specific applications. Hence, other heat transfer problem must be tackled, *i.e.*, the design heat transfer problem. In the literature exists numerous objective functions to state a design problem, but one of the most complete, in sense of thermodynamics, is the entropy generation minimisation criterion, which incorporates models of thermal resistance and pressure drop as irreversibilities due to heat transfer and fluid flow, respectively. Finally, when one requires knowing some quantities, which are difficult to measure directly, for the tune or enhance an implemented system's performance, it is required to deal with an inverse heat transfer problem (IHTP). Therefore, Figure 2.2 summarises all mentioned in this subsection.

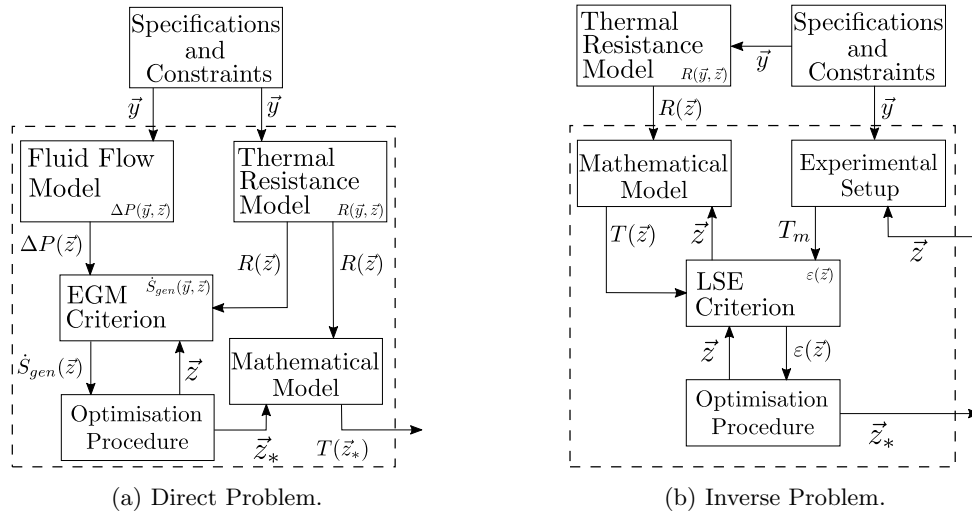


Figure 2.2. Heat transfer problems related to the electronic thermal management based on microchannel heat sinks.

## 2.2 Modern optimisation methods

In this section, some important concepts are presented. At first, three general definitions are displayed, subsequently, the optimization algorithms are defined.

**Definition 1.** Let  $\mathfrak{X}^n = \{\underline{x}_1^n, \underline{x}_2^n, \dots, \underline{x}_M^n\}$  be a finite set of candidate solutions for any optimisation problem in  $\mathbb{R}^D$ , with an objective function given by  $f : \mathbb{R}^D \rightarrow \mathbb{R}$ .  $D$  is the dimensionality of the problem, and  $M$  is the number of candidate solutions. Thus,  $\underline{x}_m^n = (x_{m,1}^n, x_{m,2}^n, \dots, x_{m,D}^n)^\top$  denotes the  $m$ -th candidate in  $\mathbb{R}^D$  at the time  $n$  of an iterative procedure, with a maximum number of iterations  $N$ .

**Definition 2.** Let  $\underline{x}_*^n \in \mathfrak{X}^n$  be the best solution found at the  $n$ -th iteration, i.e.,  $\underline{x}_*^n = \arg \min (\{f(\mathfrak{X}^n)\} \cup f(\underline{x}_*^{n-1}))$  with  $\{f(\mathfrak{X}^n)\} = \{f(\underline{x}_1^n), f(\underline{x}_2^n), \dots, f(\underline{x}_M^n)\}$ .

**Definition 3.** Let  $\mathfrak{X}^{n+1}$  represent the finite set of new candidate solutions. Each new candidate  $\underline{x}_m^{n+1}$  is obtained through an iterative procedure, namely, an optimisation algorithm.

### 2.2.1 Unified Particle Swarm Optimisation

Unified Particle Swarm Optimisation (UPSO) was proposed by Parsopoulos and Vrahatis in 2004 [141], and consists in a modification of the Particle Swarm Optimisation (PSO) algorithm [142]. This method is a swarm intelligence based technique widely used in engineering design applications [143–145]. The most important feature of UPSO is that its particles can be organised in neighbourhoods to enhance its exploration and exploitation features. All particles in the swarm have two basic components: position ( $\underline{x}_m^n \in \mathfrak{X}^n$ ) and velocity ( $\underline{v}_m^n \in \mathfrak{V}^n$ ). Before detail these components, it is needed to introduce three important definitions:

**Definition 4.** Let  $\mathfrak{Q}_m^n \subseteq \mathfrak{X}^n$  be the neighbourhood of the  $m$ -th candidate solution at the time  $n$ ,  $\underline{x}_m^n$ , with a given topology, e.g.,  $\mathfrak{Q}_m^n = \{\underline{x}_{m-1}^n, \underline{x}_m^n, \underline{x}_{m+1}^n\}$ .

**Definition 5.** Let  $\underline{x}_{m,l*}^n \in \mathfrak{Q}_m^n$  be the best candidate solution in the neighbourhood  $\mathfrak{Q}_m^n$ , i.e.,  $\underline{x}_{m,l*}^n = \arg \min (\{f(\mathfrak{Q}_m^n)\} \cup f(\underline{x}_{m,l*}^{n-1}))$ .

**Definition 6.** Let  $\underline{x}_{m,*}^n$  be the best solution which the  $m$ -th particle has found till the time  $n$ , i.e.,  $\underline{x}_{m,*}^n = \arg \min (f(\underline{x}_{m,*}^n), f(\underline{x}_{m,*}^{n-1}))$ .

Then, the new position for each particle,  $\underline{x}_m^{n+1}$ , is obtained with,

$$\underline{x}_m^{n+1} = \underline{x}_m^n + \underline{v}_m^{n+1}, \quad (2.35)$$

since the total velocity ( $\underline{v}_m^{n+1}$ ) calculated as a weighted sum between the global velocity ( $\underline{G}_m^{n+1}$ ) and the local velocity ( $\underline{L}_m^{n+1}$ ), such as

$$\underline{v}_m^{n+1} = (1 - \underline{u}) \odot \underline{L}_m^{n+1} + \underline{u} \odot \underline{G}_m^{n+1}. \quad (2.36)$$

where  $\underline{u} \in [0, 1]$  is the unification factor that balances the global and local displacement contributions. These velocity components are obtained as is shown,

$$\underline{G}_m^{n+1} = \chi [\underline{v}_m^n + \phi_1 r_1 \odot (\underline{x}_{m,*}^n - \underline{x}_m^n) + \phi_2 r_2 \odot (\underline{x}_*^n - \underline{x}_m^n)], \quad (2.37)$$

$$\mathcal{L}_m^{n+1} = \chi [\underline{v}_m^n + \phi_1 \underline{r}_3 \odot (\underline{x}_{m,*}^n - \underline{x}_m^n) + \phi_2 \underline{r}_4 \odot (\underline{x}_{m,l*}^n - \underline{x}_m^n)], \quad (2.38)$$

since  $\chi \in (0, 1]$  is the constriction factor,  $\underline{v}_m^n$  and  $\underline{x}_m^n$  are the current velocity and position for the  $m$ -th particle;  $\phi_1$  and  $\phi_2$  are the self and swarm confidence coefficients, respectively;  $\underline{r}_1, \underline{r}_2, \underline{r}_3$  and  $\underline{r}_4$  are vectors of i.i.d. random variables with  $\mathcal{U}(0, 1)$ ; and  $\underline{x}_{m,*}^n, \underline{x}_{m,l*}^n$  and  $\underline{x}_*^n$  are the best position found by each particle (Definition 6), by each neighbourhood (Definition 5) and by the entire swarm (Definition 2), respectively. Furthermore, a summarised description of the UPSO process is presented in Pseudocode 1.

---

**Pseudocode 1.** Unified Particle Swarm Optimisation (UPSO).

---

**Input:**  $f : \mathbb{R}^D \rightarrow \mathbb{R}$ ,  $M > 2$ ,  $\{u, \chi\} \in (0, 1)$ ,  $\phi_1 + \phi_2 > 4$ ,  $N \gg 1$ , topology for  $\mathfrak{Q}$ , and other stopping criteria

**Output:**  $\underline{x}_*^n$

1: Initialise  $\mathfrak{X}^0$  and  $\mathfrak{V}^0$ , find  $\underline{x}_*^0$  using Definition 2, and make  $n \leftarrow 0$ .

2: **repeat**

3:     Find  $\underline{x}_*^n$  using Definition 2.

4:     Find  $\underline{x}_{m,l*}^n$  using Definition 5.

5:     Find  $\underline{x}_{m,*}^n$  using Definition 6.

6:     Determine  $\mathfrak{X}^{n+1}$  with (2.35), and make  $n \leftarrow n + 1$ .

▷ Swarm Dynamic

7: **until** ( $n < N$ ) & (any stopping criterion is not reached)

---

## 2.2.2 Cuckoo Search

Cuckoo Search (CS) was proposed by Yang and Deb in 2009 as a methodology to exploit some features from metaheuristics, such as swarm intelligence and random walk through Lévy flight [146]. CS mimics brood parasitism behaviour of certain cuckoo species, which hide their eggs inside alien nests. At the first step, a limited number of nests are randomly chosen ( $\mathfrak{X}^n$ ). Thereafter, only the best nest (with the luckiest egg or the best actual solution) shall prevail for the next generation,  $\underline{x}_*^{n+1}$ . Whilst the nests with poorer solutions ( $\underline{x}_m^n$ ) are replaced with new eggs ( $\underline{x}_m^{n+1}$ ) using a Lévy flights, as

$$\underline{x}_m^{n+1} = \underline{x}_m^n + \zeta \underline{\nu} \odot (\underline{x}_m^n - \underline{x}_*^n), \quad (2.39)$$

where  $\zeta > 0$  is the spatial step size;  $\underline{x}_m^n$  is the  $m$ -th solution at generation  $n$  with  $D$  components, since  $D$  is defined as the dimension of search space;  $\underline{\nu}$  is a vector of i.i.d. random numbers obtained from Mantegna's algorithm using the symmetric Lévy stable distribution [147]; and  $\odot$  is the Hadamard–Schur's product.

Moreover, some cuckoo eggs may be in trouble because they are discovered by the host bird, who shall destroy the intruder's egg, then cuckoos have to find other available nests to hide their new eggs. That event shall happen with a probability of  $p_a \in \mathcal{U}(0, 1)$  for a set number of nests, and new solutions are calculated using,

$$\underline{x}_m^{n+1} = \underline{x}_m^n + \underline{u} \odot \mu(\underline{u} - p_a \underline{1}) \odot (\underline{x}_j^n - \underline{x}_k^n) \quad (2.40)$$

where  $\underline{u}$  is a vector of i.i.d. random variables with  $\mathcal{U}(0, 1)$ ;  $\mu(\cdot)$  is the multidimensional form of Heaviside function [147];  $\underline{x}_j^n$  and  $\underline{x}_k^n$  are two different solutions randomly chosen,  $j \neq k$ ; and  $\underline{1}$  is a dummy vector of elements equal to one.

The procedure of CS is presented in Pseudocode 2.

---

**Pseudocode 2.** Cuckoo Search (CS).

---

**Input:**  $f : \mathbb{R}^D \rightarrow \mathbb{R}$ ,  $M > 2$ ,  $p_a \in (0, 1)$ ,  $\zeta > 0$ ,  $N \gg 1$ , and other stopping criteria

**Output:**  $\underline{x}_*^n$

- 1: Initialise  $\mathfrak{X}^0$ , find  $\underline{x}_*^0$  using Definition 2, and make  $n \leftarrow 0$ .
  - 2: **repeat**
  - 3:     Determine  $\mathfrak{X}^{n+1}$  with (2.39) and Definition 3. ▷ Lévy flight
  - 4:     Update  $\mathfrak{X}^{n+1}$  with (2.40) and Definition 3. ▷ Eggs' discovery
  - 5:     Find  $\underline{x}_*^0$  using Definition 2, and make  $n \leftarrow n + 1$ .
  - 6: **until** ( $n < N$ ) & (any stopping criterion is not reached)
- 

### 2.2.3 Deterministic Spiral Optimisation Algorithm

Deterministic Spiral Optimisation Algorithm (DSOA) is a direct-solving metaheuristic procedure based on the logarithmic spiral dynamic [148, 149]. It is also known as Spiral Optimisation Algorithm (SOA) or just Spiral Optimisation (SPO or SO), according to [118, 150, 151]. The basic idea of this numerical process consists on rotating a set of points around a reference centre point, following a trajectory given by the logarithmic spiral. This reference is iteratively updated using a fitness criterion, *i.e.*, a location ( $\underline{x}_*^n$ ) given by an objective function  $f(\underline{x})$ ,  $\underline{x} \in \mathbb{R}^D$  (cf. Definition 2). Spiral dynamics have shown to strengthen diversification and intensification strategies, both common in metaheuristic methods [150]. The above mentioned idea is mathematically formulated by using Definitions 1 to 3, such as,

$$\underline{x}_m^{n+1} = r\mathbf{R}_D(\theta)\underline{x}_m^n - (r\mathbf{R}_D(\theta) - \mathbf{I}_D)\underline{x}_*^n, \quad (2.41)$$

where  $\mathbf{I}_D \in \mathbb{R}^{D \times D}$  is the identity matrix and,  $r \in (0, 1)$  and  $\theta \in (0, 2\pi)$  are the control parameters of spiral dynamics, which represent the convergence rate and the rotation angle, between a  $m$ -th point ( $\underline{x}_m^n$ ) and the centre point ( $\underline{x}_*^n$ ), respectively. Likewise,  $\mathbf{R}_D(\theta) \in \mathbb{R}^{D \times D}$  is the rotation matrix defined by the product of all possible combinations of 2D rotation matrices,  $\mathbf{R}(\theta) = e^{\theta \mathbf{L}_k} \in \mathbb{R}^{D \times D}$  in accordance with the Euler–Rodrigues's rotation formula [152], as shown

$$\mathbf{R}_D(\theta) = \prod_{k=1}^K e^{\theta \mathbf{L}_k}, \quad \text{and} \quad \mathbf{L}_k = \hat{u} \otimes \hat{v} - \hat{v} \otimes \hat{u}, \quad (2.42)$$

since the  $k$ -th plane,  $k \in \{1, 2, \dots, K\}$ , is formed by a vector pair  $\{\hat{u}, \hat{v}\}$  from the canonical basis of  $\mathbb{R}^D$ ,  $\{\hat{u}, \hat{v}\} \in \{\hat{e}_1, \hat{e}_2, \dots, \hat{e}_D\}$ , and  $\otimes$  is the outer product or the tensor product for two vectors.  $L_k$  is called the skew-symmetric matrix generator and  $K = D(D - 1)/2$  is the planes combination's number in  $D$ .

Subsequently, DSOA is summarised in Pseudocode 3.

### 2.2.4 Stochastic Spiral Optimisation Algorithm

Stochastic Spiral Optimisation Algorithm (SSOA) is a modification of DSOA proposed by Cruz–Duarte *et al.* in 2017 [153], which aims at tackling the major known drawbacks of the original strategy, *i.e.* its slow convergence. For that reason, some random disturbances are included in the spiral dynamics of each searching point or agent, alike the natural shaking behaviour of dust particles moving through the wind. This idea is formalised by restating

---

**Pseudocode 3.** Deterministic Spiral Optimisation Algorithm (DSOA).

---

**Input:**  $f : \mathbb{R}^D \rightarrow \mathbb{R}$ ,  $M > 2$ ,  $\theta \in (0, 2\pi)$ ,  $r \in (0, 1)$ ,  $N \gg 1$ , and other stopping criteria

**Output:**  $\underline{x}_*^n$

- 1: Determine  $\mathbf{R}_D(\theta)$  using (2.42).
  - 2: Initialise  $\mathfrak{X}^0$ , find  $\underline{x}_*^0$  using Definition 2, and make  $n \leftarrow 0$ .
  - 3: **repeat**
  - 4:   Update  $\mathfrak{X}^{n+1}$  with (2.41). ▷ Deterministic Spiral Dynamic
  - 5:   Find  $\underline{x}_*^{n+1}$  using Definition 2, and make  $n \leftarrow n + 1$ .
  - 6: **until** ( $n < N$ ) & (any stopping criterion is not reached)
- 

the DSOA kernel equation in (2.41) such as,

$$\underline{x}_m^{n+1} = \tilde{r} \mathbf{R}_D(\theta) \underline{x}_m^n - \underline{\delta}_x(n) \odot (\tilde{r} \mathbf{R}_D(\theta) - \mathbf{I}_D) \underline{x}_*^n, \quad (2.43)$$

where  $\tilde{r}$  is the stochastic convergence rate, defined as a uniformly distributed random value between  $r_l$  and  $r_u$ , *i.e.*,  $\tilde{r} \sim \mathcal{U}(r_l, r_u)$ ;  $\underline{\delta}_x(n) \in \mathbb{R}^D$  is the radius scale vector that depends of the current step ( $n$ ), and other additional metrics (previously defined); and  $\odot$  is the Hadamard–Schur’s product. Other parameters remain unchanged and follow definitions above. In this work, for the sake of simplicity, parameters  $\tilde{r}$  and  $\underline{\delta}_x(n)$  can be chosen as,

$$\tilde{r} \sim \mathcal{U}(r_l, 1.0), \quad (2.44)$$

$$\underline{\delta}_x(n) = \underline{u}, \quad (2.45)$$

since  $0 < r_l < 1.0$  is the lower limit of  $\tilde{r}$ , and  $\underline{u} \in \mathbb{R}^D$  is a vector of i.i.d. random variables with  $\mathcal{U}(0.0, 1.0)$ .

As with DSOA, the basic scheme of SSOA is presented in Pseudocode 4.

---

**Pseudocode 4.** Stochastic Spiral Optimisation Algorithm (SSOA).

---

**Input:**  $f : \mathbb{R}^D \rightarrow \mathbb{R}$ ,  $M > 2$ ,  $\theta \in (0, 2\pi)$ ,  $r_l \in (0, 1)$ ,  $N \gg 1$ , and other stopping criteria

**Output:**  $\underline{x}_*^n$

- 1: Determine  $\mathbf{R}_D(\theta)$  using (2.42)
  - 2: Initialise  $\mathfrak{X}^0$ , find  $\underline{x}_*^0$  using Definition 2, and  $n \leftarrow 0$
  - 3: **repeat**
  - 4:   Update  $\mathfrak{X}^{n+1}$  with (2.43) ▷ Stochastic Spiral Dynamic
  - 5:   Find  $\underline{x}_*^{n+1}$  using Definition 2, and  $n \leftarrow n + 1$
  - 6: **until** ( $n < N$ ) & (any stopping criterion is not reached)
-

## 2.3 Methodology

In this work, multiple scenarios of design were studied through the entropy generation minimisation (EGM) criterion, and powered by three non-conventional optimisation methods: Particle Swarm Optimisation (UPSO), Deterministic Spiral Optimisation Algorithm (DSOA) and Cuckoo Search (CS). This aim requires, however, a procedure integrated by two sequential phases or stages, *i.e.*, preparation and execution. Moreover, the statistical data presented in this document were calculated for one hundred of runs per optimisation process.

Preparation consisted on implementing the selected optimisation methods, using a numerical computing platform on an ASUS<sup>®</sup> laptop, S46C model, with an Intel<sup>®</sup> Core<sup>™</sup> i7-3537U CPU @ 2.00–2.50 GHz, 6 GB RAM and Microsoft<sup>®</sup> Windows<sup>™</sup>10 – 64 bit. The convergence criterion was considered as a maximum number of iterations without improving the solution (also known as stagnation); in this case, it is assumed a stagnation state at the thousandth step. This non-improving flag is raised when the following condition is reached,

$$(f(\underline{x}_*^n) - \langle f(X_*) \rangle)^2 \leq \langle f(X_*)^2 \rangle - \langle f(X_*) \rangle^2, \quad (2.46)$$

where  $f(\underline{x}_*^n)$  is the fitness value at last iteration  $n$ ,  $\langle f(X_*) \rangle$  is the historical average value and  $\langle f(X_*)^2 \rangle$  is the historical mean squared value, since  $f(X_*) = \{f(\underline{x}_*^1), f(\underline{x}_*^2), \dots, f(\underline{x}_*^n)\}$  is the set of found fitness values. In other words, the stagnation condition is met whenever the current fitness value falls within one standard deviation of historical fitness values.

Control parameters of the optimisation techniques were tuned via a parametric study performed with 17 benchmark functions from [154], using a tolerance error of  $1 \times 10^{-6}$  as the stop criterion. Several populations (*i.e.*, number of agents, particles or nests) were considered for all methods. Data showed that some strategies performed better with 25 agents, whilst others required 100. Thus,  $N$  was set to 100 for all of them, striving to use the same conditions for all cases.

The second stage consisted on defining and implementing the design problem using the objective function  $\dot{S}_{gen}$  found in (2.11), and by setting  $\alpha$ ,  $\beta$  and  $G_{wf}$  as design variables. Constraints of the design variables were selected based on previous works and manufacturing limitations [39, 51, 155, 156]. Applying the entropy generation minimisation criterion, the current problem can be stated as:

$$\begin{aligned} \min_{\alpha, \beta, G_{wf}} \dot{S}_{gen}(\alpha, \beta, G_{wf}) &= \frac{\dot{Q}_d^2 R_{eq}(\alpha, \beta, G_{wf})}{T_a T_i(\alpha, \beta, G_{wf})} + \frac{G_{wf}}{T_a} \Delta P(\alpha, \beta, G_{wf}), \\ \text{subject to } 0.001 &\leq \alpha \leq 0.1, 2 \leq \beta \leq 10, \\ 1 \times 10^{-5} &\leq G_d \leq 1 \times 10^{-2} \text{ m}^3/\text{s}. \end{aligned} \quad (2.47)$$

Moreover, this stage consisted in four illustrative cases varying their designing scenarios for rectangular microchannel heat sinks, employing the specifications given by Table 2.1 and the thermophysical properties in Table 2.2. Initially, the volumetric flow rate  $G_{wf}$  was selected as a design specification. Later on, it was incorporated as a design variable. Three first cases dealt with a designing problem in accordance with the EGM criterion, but the fourth case studied the inverse heat transfer problem, cf. Section 2.1.3. Each case is described as follow:

*Case 1.* The RMCHS is assumed made of aluminium is considered with air and ammonia gas (NH<sub>3</sub>) as feasible working fluids. In this case, DSOA was implemented as optimiser.



*Case 2.* The device is defined made of High Thermal Conductive Graphite (HTCG) with air, ammonia gas ( $\text{NH}_3$ ) and the nanofluid  $\text{H}_2\text{O-TiO}_2$  as working fluids were studied. The average thermophysical properties for the nanofluid were determined via (2.22) to (2.25), for different values of nanoparticle volume concentration ( $\phi$ ), [157]. In this part, all three optimisation algorithms were considered, *i.e.*, UPSO, CS, and DSOA.

*Case 3.* The RMCHS made of HTCG was specified and two different nanoparticles in water-based colloidal fluids were considered as coolants: aluminium (Al) and titanium dioxide ( $\text{TiO}_2$ ), *i.e.*,  $\text{H}_2\text{O-Al}$  and  $\text{H}_2\text{O-TiO}_2$ . For this case, CS was employed.

*Case 4.* Two materials were assumed for the RMCHS, *i.e.*, silicon (Si) and HTCG, and two working fluids studied in the Case 1, *i.e.*, air and  $\text{NH}_3$ , were explored. CS was also utilised but, in this case, an inverse heat transfer problem was analysed.

Table 2.1: Values used for the parameters of the heat sink.

Parameter	Value	Unit
$L_d, L_i$	51	mm
$W_d, W_i$	51	mm
$H_c$	1.7	mm
$t_b$	0.1	mm
$R'_i$	$27 \times 10^{-3}$	$\text{m}^2 \cdot \text{K}/\text{W}$
$\dot{q}$	$150 \times 10^3$	$\text{W}/\text{m}^2$

Table 2.2: Thermophysical properties of the heat sink materials and working fluids.

Material/Fluid	$\rho$ [ $\text{kg}/\text{m}^3$ ]	$k$ [ $\text{W}/\text{m} \cdot \text{K}$ ]	$c$ [ $\text{J}/\text{kg} \cdot \text{K}$ ]	$\nu$ [ $\text{m}^2/\text{s}$ ]
Silicon (Si)	2330	148	703	-
Aluminum (Al)	2707	237	910	-
High Thermal Conductive Graphite (HTCG)	1000	1900	742	-
Titanium dioxide ( $\text{TiO}_2$ )	4157	8.4	710	-
Air	1.1614	0.0261	1007	$1.58 \times 10^{-5}$
Ammonia gas ( $\text{NH}_3$ )	0.7	0.0270	2158	$1.47 \times 10^{-5}$
Water ( $\text{H}_2\text{O}$ )	994.2	0.6250	4178	$7.29 \times 10^{-7}$

## 2.4 Results and discussion

### 2.4.1 Preparation of the optimisation algorithms

Table 2.3 presents the selected control parameters (minus population size), as well as the values considered throughout the preliminary testing phase. Candidate values were chosen based on literature reports. Table 2.4 displays, as an illustrative example, the statistical results of all methods solving five benchmark functions with the selected parameters. Furthermore, an analysis of sensitivity was performed for all the implemented algorithms but, for the brevity's sake, few illustrative data are presented in Table 2.5. Data relate to the Cuckoo Search strategy optimising the Beale function and considering a 10% perturbation for  $p_a$  and  $\zeta$ . An inconclusive correlation was noticed between changes of the control parameter values and performing the optimisation method.

Table 2.3: Parameters considered as candidates, and selected for the studied optimisation algorithms. For all cases,  $N = 100$ .

Method	Parameter	Considered values	Selected value
UPSO	$\phi_1$	2.0, 2.5 and 3.0	2.0
	$\phi_2$	2.0, 2.5 and 3.0	2.5
	$\chi$	0.6, 0.7 and 0.8	0.6
	$u$	0.2, 0.5 and 0.8	0.5
DSOA	$r$	0.90, 0.95 and 0.99	0.99
	$\theta$	$\pi/8$ , $\pi/4$ and $\pi/2$	$\pi/8$
CS	$p_a$	0.25, 0.50 and 0.75	0.5
	$\zeta$	0.50, 0.75 and 1.00	1.0

### 2.4.2 Case 1: AI-based RMCHS with air and NH<sub>3</sub>

Figure 2.3a shows the minimal entropy generation rate ( $\dot{S}_{gen,min} = \dot{S}_{gen}(z_*)$  [W/K]), related to aluminium heat sinks with two different working fluids and for several volumetric flow rates ( $G_{wf}$  [m<sup>3</sup>/s]). It is evident that heat sinks using environmentally friendly ammonia (NH<sub>3</sub>) perform better than those using air. In fact, for all the studied values of  $G_{wf}$ , they generated an average of  $21 \pm 6$  % less entropy. Even so, Figure 2.3a also shows that in both cases the minimum entropy is generated for values of  $G_{wf}$  between 0.0040 and 0.0045 m<sup>3</sup>/s. This is coherent with the inverse dependency of the optimal equivalent thermal resistance ( $R_{eq}^*$  [K/W]) and the optimal total pumping power ( $\Phi^*$  [W]), in terms of  $G_{wf}$  (Figure 2.3b). Using air instead of ammonia as working fluid affects the MCHS performance in, mainly, two ways. The first one is evident from Figure 2.3b, observing an increase in  $R_{eq}^*$  and  $\Phi^*$  ( $15 \pm 2$  % and  $34 \pm 7$  %, respectively). These results share a strong link with the thermophysical properties of the working fluid and of the bulk material, as well as with the geometry of the channel array. The second one refers to the latter, and we found that the optimal design requires wider channels (at most 20 % on average) and slightly thinner walls (at most 9 % on average). Hence, it is easy to notice the strong influence that the working fluid has in this process.

Figure 2.4 shows the relative contribution of each thermal resistance considered during this study. The ones that provide most of the resistance relate to the interface ( $R_i$ ), to

Table 2.4: An illustrative example of benchmark functions solved by the optimisation techniques with found values of control parameters.

Function	Method	$f_{obj}(\underline{x}_*) \times 10^{-9}$	Steps	Time [s]
		Avg. $\pm$ St. Dev.	Avg. $\pm$ St. Dev.	Avg. $\pm$ St. Dev.
Beale	UPSO	405.91 $\pm$ 241.62	32 $\pm$ 9	0.43 $\pm$ 0.14
	DSOA	394.75 $\pm$ 298.04	481 $\pm$ 75	1.41 $\pm$ 0.23
	CS	306.69 $\pm$ 222.72	37 $\pm$ 28	0.32 $\pm$ 0.21
Bukin 2	UPSO	370.82 $\pm$ 254.43	33 $\pm$ 7	0.40 $\pm$ 0.11
	DSOA	420.22 $\pm$ 315.99	478 $\pm$ 73	4.26 $\pm$ 0.66
	CS	347.53 $\pm$ 294.30	75 $\pm$ 63	0.54 $\pm$ 0.42
Cube	UPSO	429.96 $\pm$ 301.14	333 $\pm$ 79	0.91 $\pm$ 0.22
	DSOA	396.53 $\pm$ 281.79	596 $\pm$ 79	6.66 $\pm$ 0.88
	CS	535.84 $\pm$ 279.39	692 $\pm$ 81	4.93 $\pm$ 4.82
Rosenbrock	UPSO	379.09 $\pm$ 260.22	186 $\pm$ 32	2.41 $\pm$ 0.75
	DSOA	443.73 $\pm$ 302.72	752 $\pm$ 73	2.04 $\pm$ 0.30
	CS	553.63 $\pm$ 294.07	677 $\pm$ 48	3.02 $\pm$ 0.42
Wayburn Seader 1	UPSO	413.00 $\pm$ 258.38	44 $\pm$ 7	0.44 $\pm$ 0.07
	DSOA	428.88 $\pm$ 275.11	140 $\pm$ 14	1.58 $\pm$ 0.16
	CS	421.89 $\pm$ 274.02	204 $\pm$ 32	0.45 $\pm$ 0.39

Table 2.5: An illustrative example of the sensitivity analysis performed for Beale function with CS using  $p_a$  and  $\zeta$  of  $0.5 \pm 10\%$  and  $1.0 \pm 10\%$ , respectively.

$p_a$	$\zeta$	$f_{obj}(\underline{x}_*) \times 10^{-9}$	Steps	Time [s]
		Avg. $\pm$ St. Dev.	Avg. $\pm$ St. Dev.	Avg. $\pm$ St. Dev.
0.50	0.90	370.86 $\pm$ 295.50	33 $\pm$ 16	0.52 $\pm$ 0.41
	1.00	306.69 $\pm$ 222.72	37 $\pm$ 28	0.32 $\pm$ 0.21
	1.10	299.91 $\pm$ 290.87	34 $\pm$ 45	0.25 $\pm$ 0.71
0.45		514.03 $\pm$ 263.54	44 $\pm$ 21	0.50 $\pm$ 0.81
0.50	1.00	306.69 $\pm$ 222.72	37 $\pm$ 28	0.32 $\pm$ 0.21
0.55		411.56 $\pm$ 311.12	28 $\pm$ 52	0.94 $\pm$ 0.46

convection ( $R_h$ ), and to the fluid ( $R_f$ ). The first one, *i.e.*,  $R_i$ , is tightly linked to the material used at the interface between the chip and the heat sink. For our study, we assumed a thermal paste with  $t_i/k_i = 27 \times 10^{-3} \text{ m}^2\cdot\text{K}/\text{W}$ . Nonetheless, this resistance can be easily dealt with by using another material with better thermal conductivity. The working fluid, however, provides most of the thermal resistance ( $52 \pm 16\%$ ). The resistance due to heat transfer by convection represents in average  $12 \pm 6\%$  of the total equivalent thermal resistance.

As a final approach, the optimisation problem in (2.47) was solved for  $\alpha (= 2w_c/H_c)$ ,  $\beta (= w_c/w_p)$  and  $G_{wf}$  as design variables. The resulting data is summarised in Table 2.6, where aluminium heat sinks with air and environmentally friendly ammonia as a working fluids, are presented. Using ammonia decreases the minimal entropy generation rate in about  $17\%$ . Consequently, the equivalent thermal resistance and the pumping power decrease in about  $18\%$  and  $25\%$ , respectively. This represents an average surface temper-

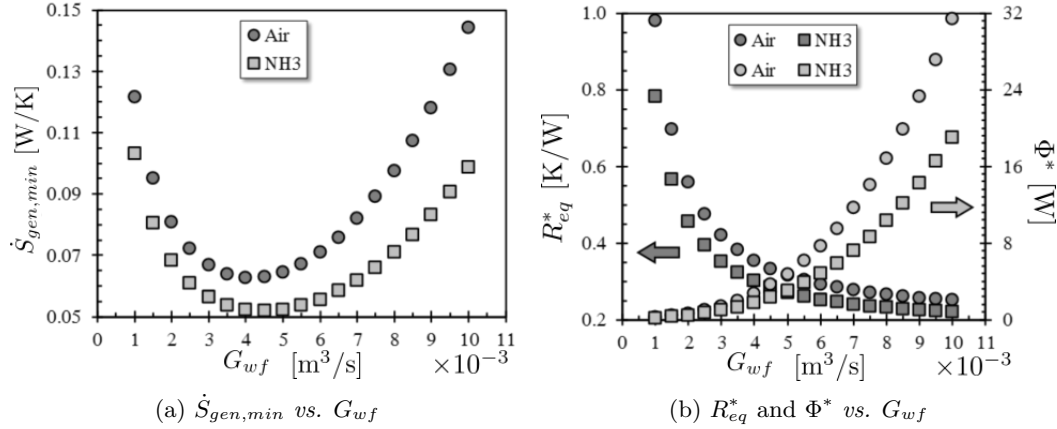


Figure 2.3. (a) Minimal entropy generation rate, and (b) optimal equivalent thermal resistance and total pumping power, for some volume flow rate values, as a design specification, using air and NH<sub>3</sub> as working fluids in an aluminium RMCHS.

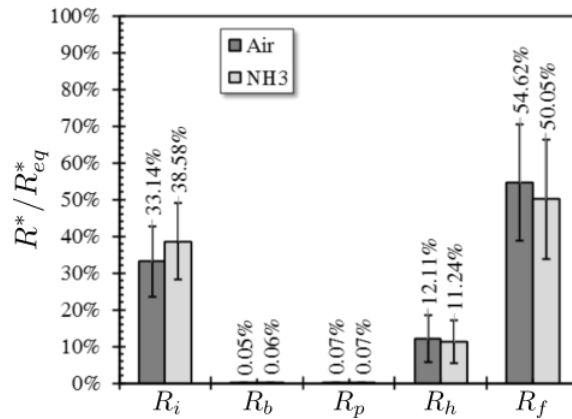


Figure 2.4. Relative distribution of the equivalent thermal resistance (Avg.  $\pm$  St. Dev.) per component, using air and NH<sub>3</sub> as working fluids in an aluminium RMCHS.

ature on the chip 7 K lower, and an average pumping power 0.78 W smaller. In spite of these benefits, it is worth mentioning that the ammonia heat sink requires 20 additional channels.

### 2.4.3 Case 2: HTCG-based RMCHS with air, NH<sub>3</sub> and H<sub>2</sub>O-TiO<sub>2</sub>

In spite of the vast amount of data available and for the sake of brevity, it is presented just the one related to the Cuckoo Search algorithm, because data slightly differ throughout the algorithms used in this case of study. Figure 2.5 shows the tendency of the minimal entropy generation rate ( $\dot{S}_{gen,min}$ ) as a function of the volume flow rate ( $G_{wf}$ ); the latter was considered as a design specification. Several working fluids were used, such as air, NH<sub>3</sub> and H<sub>2</sub>O-TiO<sub>2</sub> with different nanoparticles concentrations. The designs achieved for air and ammonia gas have a similar behaviour in terms of  $\dot{S}_{gen,min}$ , and both present a lower value whenever  $G_{wf}$  is about  $4.5 \times 10^{-3}$  m<sup>3</sup>/s. However, at same value of volume flow rate,  $\dot{S}_{gen,min}$  is higher when a nanofluid is used as working fluid. This effect is due, in large portion, to the big difference between the densities of the nanofluid ( $\approx 994$  kg/m<sup>3</sup>)

Table 2.6: Optimal designs for a rectangular microchannel heat sink (RMCHS) with aluminium as bulk material and, air and ammonia gas (NH<sub>3</sub>) as working fluids.

Parameter	Air	NH <sub>3</sub>	Unit
Entropy generation rate ( $\dot{S}_{gen,min}$ )	0.0627	0.0519	W/K
Equivalent thermal resistance ( $R_{eq}^*$ )	0.3450	0.2846	K/W
Total pumping power ( $\Phi^*$ )	3.10	2.32	W
Average film coefficient ( $\bar{h}^*$ )	457.80	553.81	W/m <sup>2</sup> K
Reynolds number ( $Re_{D_h}^*$ )	178	175	-
Number of channels ( $N_c^*$ )	118	138	-
Channel's width ( $2w_c^*$ )	296.34	253.49	$\mu\text{m}$
Wall's width ( $2w_p^*$ )	127.99	109.25	$\mu\text{m}$
Volume flow rate ( $G_{wf}^*$ )	4.21	4.48	m <sup>3</sup> /s

and the non-colloidal fluids ( $\approx 1 \text{ kg/m}^3$ ); that conclusion is based on the information available on Table 2.1. Heat sinks with nanofluids have minimal entropy generation rate at about  $9.0 \times 10^{-5} \text{ m}^3/\text{s}$ . For values of  $G_{wf}$  greater than  $1.0 \times 10^{-3} \text{ m}^3/\text{s}$ , we noticed that the nanoparticle volume concentration has a special effect over the total minimal entropy generation rate. We found that the  $\dot{S}_{gen,min}$  increase is due to the fluid flow irreversibility, and it is analysed below. Nevertheless, designs considering nanofluids have lower  $\dot{S}_{gen,min}$  than the ones with air and NH<sub>3</sub> (considered as traditional working fluids), for values of  $G_{wf} \leq 1.0 \times 10^{-3} \text{ m}^3/\text{s}$ . Therefore, for these  $G_{wf}$  values, we found that colloids represent a good alternative for lower volume flow rates.

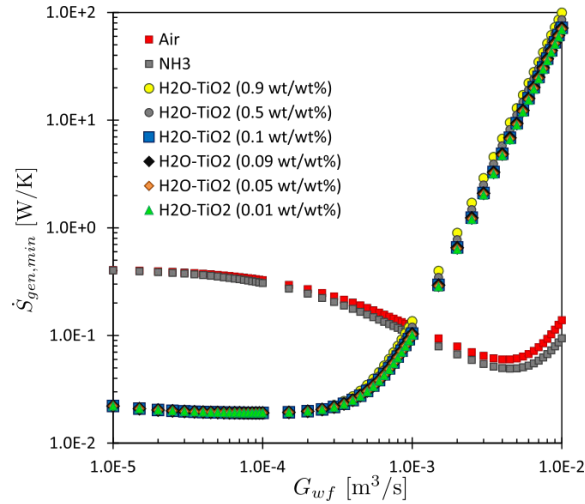


Figure 2.5. Minimal entropy generation rate,  $\dot{S}_{gen,min}$ , for several values of volume flow rate ( $G_{wf}$ ) and different working fluids, as design specifications of the HTCG-based RMCHS. Air, NH<sub>3</sub> and H<sub>2</sub>O-TiO<sub>2</sub> ( $\phi = 0.01, \dots, 0.9 \text{ wt/wt\%}$ ) were considered.

Figure 2.6 shows a measure of the irreversibilities present on heat sinks for several values of  $G_{wf}$  and different nanoparticle volume fractions at the working fluid. Figure 2.6a presents the optimal equivalent thermal resistance ( $R_{eq}^*$ ) as a function of the volume flow rate ( $G_{wf}$ ). This parameter is directly related to the irreversibility derived from heat trans-

fer of the heat sink. For all considered volume fractions, these irreversibilities exhibit a parabolic behaviour in the interval given by  $1 \times 10^{-5} \leq G_{wf} \leq 3.5 \times 10^{-3} \text{ m}^3/\text{s}$ , with a minimal value at  $G_{wf} \approx 2 \times 10^{-4} \text{ m}^3/\text{s}$ . However, a slight difference amongst the  $\phi$  values is observed. Although,  $R_{eq}^*$  presents a steady value starting at  $3.5 \times 10^{-3} \text{ m}^3/\text{s}$  due to the specified design constraints, *i.e.*,  $\alpha$  and/or  $\beta$  are equal to their established upper limits (maximum feasible values). Within the same region, the lowest thermal resistance is achieved with the highest considered value of nanoparticle concentration, *i.e.*,  $\phi = 0.9 \text{ wt/wt}\%$ . Nonetheless, the minimal equivalent thermal resistance value ( $R_{eq,min} = 113.531 \times 10^{-3} \text{ K/W}$ ) was obtained with  $0.01 \text{ wt/wt}\%$  of  $\text{H}_2\text{O-TiO}_2$  as working fluid. Afterwards, Figure 2.6b shows the tendency of the optimal total pressure drop ( $\Delta P^*$ ) as a function of the volume flow rate. This feature is narrowly related with the total flow pump power ( $\Phi$ ) and, indeed, with the irreversibility by fluid flow. In this case, the lowest value of  $\Delta P^*$  was  $519 \text{ Pa}$ , reached with a nanoparticle concentration of  $0.01 \text{ wt/wt}\%$  and  $G_{wf} = 5 \times 10^{-5} \text{ m}^3/\text{s}$ . Furthermore, we noticed that the lowest values of  $\Delta P^*$  for each considered value of  $\phi$ , lay in the interval  $4 \times 10^{-5} \leq G_{wf} \leq 5 \times 10^{-5} \text{ m}^3/\text{s}$ . Moreover, the increase of  $\Delta P^*$  is proportional to the nanoparticle concentration and to the volume flow rate. The former feature is mainly due to the higher viscosity of the nanofluid when compared to the base fluid used (*i.e.*, water) [55, 113]. Additionally, we noticed that the highest pressure drop required by a design using a traditional working fluid ( $3.088 \text{ kPa}$ )—air at  $0.01 \text{ m}^3/\text{s}$ —, is at least required in designs with nanofluids using a volume flow rate of  $3 \times 10^{-4} \text{ m}^3/\text{s}$ . In other words, we shall need  $1 \text{ W}$  of pumping power to maintain the flowing of nanofluid at  $3 \times 10^{-4} \text{ m}^3/\text{s}$ ; but the same amount of power could be used with a flow of gaseous fluid, like air or ammonia gas, passing inside the microchannels with  $3 \times 10^{-3} \text{ m}^3/\text{s}$ .

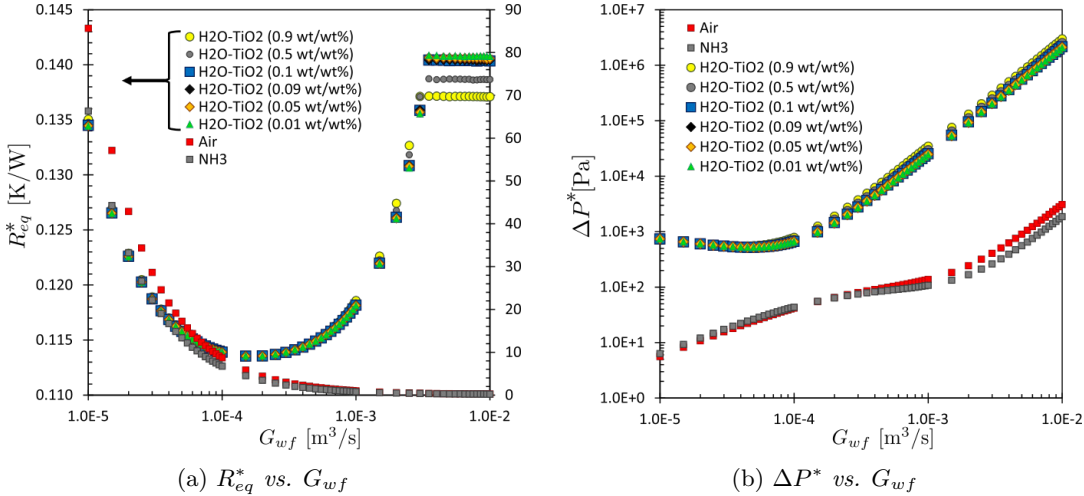


Figure 2.6. Optimal (a) equivalent thermal resistance, and (b) total pressure drop within channel, for several values of volume flow rate and different working fluids, as design specifications of the HTCG-based RMCHS.  $\text{H}_2\text{O-TiO}_2$  with  $\phi = 0.01, \dots, 0.9 \text{ wt/wt}\%$  were considered.

Figure 2.7 presents the incremental tendency of the optimal channel ( $\alpha^*$ ) and wall ( $\beta^*$ ) aspect ratios as functions of the volume flow rate ( $G_{wf}$ ). As a first look, for designs with colloids, both  $\alpha^*$  and  $\beta^*$  values have a greater slope with  $G_{wf} \geq 1.0 \times 10^{-4} \text{ m}^3/\text{s}$ , than the designs using traditional working fluids. It is useful to note that the upper constraints of  $\alpha$  and  $\beta$  are reached with  $G_{wf}$  values greater than  $3.0$  and  $1.5 \times 10^{-3} \text{ m}^3/\text{s}$ ,

respectively. This event, shown in Figure 2.7, relates to the steady  $R_{eq}^*$  value achieved with  $G_{wf} \geq 3.5 \times 10^{-3} \text{ m}^3/\text{s}$  (Figure 2.7a). It is perceived that the influence of microchannels geometry over the equivalent thermal resistance is higher than the volume flow rate. These values correspond to best solutions found at the boundary of the feasible region of the optimisation problem defined in (2.47). Moreover, it was observed that microchannels widen for increased volume flow rates, where  $H_c$  is a given design specification, and allow obtaining an optimal design (Figure 2.7a). Simultaneously, width of walls or inter-channel spacing tend to be thinner due to the increment of  $G_{wf}$  (Figure 2.7b). The aforementioned behaviour means that for a greater flow, the microchannel heat sink has to be composed by wider channels and thinner walls as to guarantee a minimal entropy generation rate. In case of gaseous working fluids, like air and ammonia gas, all designs obtained required optimal channel ( $2w_c^*$ ) and wall ( $2w_p^*$ ) widths lower than  $36.4 \mu\text{m}$  and  $5.5 \mu\text{m}$ , respectively.

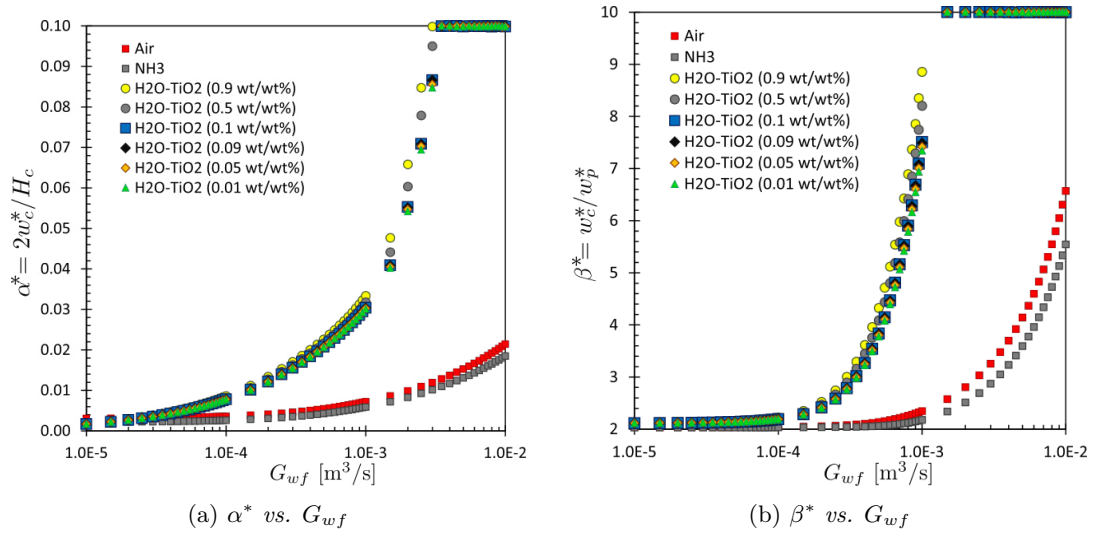


Figure 2.7. Optimal (a) channel aspect ratio and (b) wall aspect ratio, for several values of volume flow rate and different working fluids, as design specifications of the HTCG-based RMCHS.  $\text{H}_2\text{O-TiO}_2$  with  $\phi = 0.01, \dots, 0.9 \text{ wt/wt}\%$  were considered.

Furthermore, we solved the optimisation problem considering a different scenario with  $G_{wf}$  as an additional design variable. Table 2.7 shows optimal designs of a rectangular microchannel heat sink with  $\text{H}_2\text{O-TiO}_2$  as a working fluid, several nanoparticle volume concentrations ( $\phi$ ), and when using UPSO, DSOA, and CS. As a first observation, we found that concentration of nanoparticles is directly related to the minimal entropy generation rate in the heat sink. The lower values of  $\dot{S}_{gen}$  were achieved by using UPSO. This behaviour is due to the rising of viscosity in the working fluid, which flows through the rectangular microchannels. Also, this increases the pressure drop, so a higher pumping power is required to maintain the fluid motion, [54]. Further, volume fraction of nanoparticles enhances the optimal equivalent thermal resistance according to the EGM criterion. Nevertheless  $R_{eq}^*$  is close to its minimal value if the cost function is only  $R_{eq}$ . However, we can associate each design to the solution of a multi-objective problem given by two cost functions, *i.e.*,  $R_{eq}$  and  $\Delta P$ . In some cases, researchers prefer to employ a higher pumping power ( $\max \Phi = \max G_{wf} \Delta P$ ) to minimise the equivalent thermal resistance of the rectangular microchannel heat sink [39, 113]. It is noticed that the average and standard deviation of steps used by UPSO is about twice the ones required by the others meth-

ods. Oppositely, Cuckoo Search algorithm spent the lowest average of iterations to reach a well-approached design. This method performed the optimisation process about two and four times faster than the unified particle swarm and the spiral techniques, respectively. Therefore, CS is a considerably appropriate alternative method for solving thermal design problems, in this case focused to cooling electronic devices. This claim is supported by previous results like [39, 116, 156].

Table 2.7: Optimal design of the HTCG rectangular microchannel heat sink, using H<sub>2</sub>O-TiO<sub>2</sub> with  $\phi = 0.01, \dots, 0.9$  wt/wt% as working fluid, via three optimisation techniques such as Unified Particle Swarm Optimisation (UPSO), Deterministic Spiral Optimisation Algorithm (DSOA), and Cuckoo Search (CS) algorithm. Values in bold correspond to the best designs achieved.

$\phi$ [wt/wt%]	Time [s] Avg. $\pm$ St. Dev.	Steps	$\dot{S}_{gen,min}$ [W/K] $\times 10^{-3}$	$R_{eq}^*$ [K/W] $\times 10^{-3}$	$\Delta P^*$ [Pa]	$\alpha^*$ $\times 10^{-3}$	$\beta^*$	$G_{wf}^*$ [m <sup>3</sup> /s] $\times 10^{-6}$
UPSO								
0.01	2.05 $\pm$ 0.81	314 $\pm$ 127	<b>19.085</b>	114.065	608	7.1765	2.17177	89.30
0.05	2.32 $\pm$ 1.12	353 $\pm$ 176	<b>19.087</b>	114.073	612	7.1973	2.17289	89.03
0.09	2.29 $\pm$ 1.26	335 $\pm$ 197	<b>19.089</b>	114.082	615	7.2183	2.17402	88.76
0.10	2.70 $\pm$ 1.09	311 $\pm$ 112	<b>19.090</b>	114.084	616	7.2236	2.17430	88.69
0.50	2.63 $\pm$ 0.99	326 $\pm$ 128	<b>19.109</b>	114.171	653	7.4536	2.18532	86.27
0.90	2.77 $\pm$ 1.45	364 $\pm$ 177	<b>19.128</b>	114.260	688	7.7161	2.19606	84.19
DSOA								
0.01	1.32 $\pm$ 0.47	211 $\pm$ 78	19.086	113.995	629	7.1614	2.27303	91.94
0.05	1.23 $\pm$ 0.50	188 $\pm$ 71	19.095	113.939	685	6.4311	3.18633	92.01
0.09	1.30 $\pm$ 0.56	195 $\pm$ 89	19.090	114.098	600	7.4193	2.35236	90.08
0.10	1.22 $\pm$ 0.51	194 $\pm$ 82	19.092	114.011	642	7.0053	2.65195	91.40
0.50	1.38 $\pm$ 0.47	217 $\pm$ 75	19.110	114.077	694	7.2228	2.19240	87.96
0.90	1.16 $\pm$ 0.41	179 $\pm$ 63	19.129	114.247	687	7.7160	2.52404	85.54
CS								
0.01	0.56 $\pm$ 0.16	153 $\pm$ 40	19.086	114.029	623	7.1026	2.13075	89.90
0.05	0.53 $\pm$ 0.15	151 $\pm$ 41	<b>19.087</b>	114.081	609	7.1689	2.25024	88.84
0.09	0.50 $\pm$ 0.15	147 $\pm$ 40	19.090	114.031	634	7.1603	2.15441	90.02
0.10	0.56 $\pm$ 0.19	150 $\pm$ 51	<b>19.090</b>	114.111	604	7.2747	2.26619	88.43
0.50	0.56 $\pm$ 0.17	162 $\pm$ 52	<b>19.109</b>	114.171	653	7.4055	2.29641	86.38
0.90	0.62 $\pm$ 0.18	147 $\pm$ 38	19.129	114.271	684	7.8072	2.06731	83.97

Finally, Figure 2.8 is presented to analyse the performance of optimisation techniques when designing a rectangular heat sink using a nanofluid as working fluid. This results were obtained after executing 100 times the design procedure per each nanoparticle volume fraction and optimisation technique. Additional to the number of iterations spent by the optimisation methods, it was found that fitness values reached with UPSO and DSOA have a greater variance than the solutions achieved with CS. Although, from Table 2.7 we noticed that UPSO is capable of obtaining lower values of the cost function,  $\dot{S}_{gen}$ , than the ones achieved by the other two optimisation techniques. Therefore, it can be concluded



that CS is faster and more accurate than UPSO and DSOA, becoming it in an excellent alternative for thermal design, together with the entropy generation minimisation criterion.

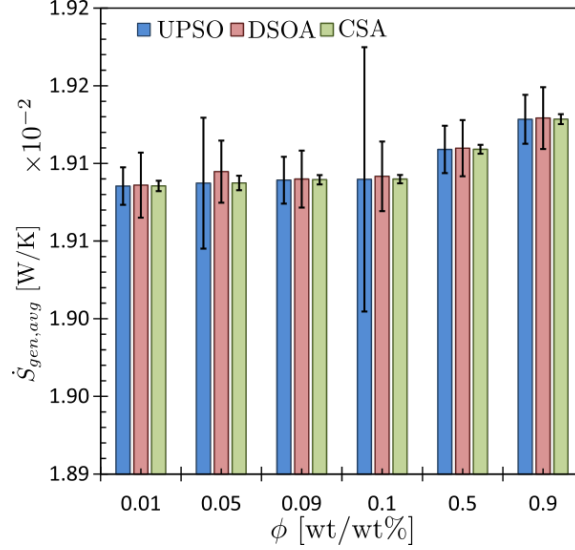


Figure 2.8. Average minimal entropy generation rate of a rectangular microchannel heat sink made up of High Thermal Conductive Graphite (HTCG) using a  $\text{H}_2\text{O-TiO}_2$  nanofluid with several values of  $\phi$  as working fluid, obtained via Unified Particle Swarm Optimisation (UPSO), Deterministic Spiral Optimisation Algorithm (DSOA) and Cuckoo Search (CS) algorithm.

#### 2.4.4 Case 3: HTCG-based RMCHS with $\text{H}_2\text{O-Al}$ and $\text{H}_2\text{O-TiO}_2$

Figure 2.9 presents designs obtained by solving the problem laid out in (2.47), where each marker represents a solution of the problem for a given design scenario. Results have an evident quadratic tendency for the minimal dimensionless entropy generation rate ( $\dot{S}_{gen,min}$ ) with the increment of the volume flow rate ( $G_{wf}$ ). Any value of  $\dot{S}_{gen,min}$  (or marker) in Figure 2.9 corresponds to an optimal geometry, which provides the minimal effect of irreversibilities on the microelectronic heat sinking process. A slope change is observed on Figure 2.9 whenever  $G_{wf} \approx 0.1062 \times 10^{-3} \text{ m}^3/\text{s}$ , which indicates the existence of a minimal value of  $\dot{S}_{gen,min}$  as a function of  $G_{wf}$ . Results show that both colloids gave the best designs for the smallest studied nanoparticles concentration, *i.e.*,  $\phi = 0.01 \text{ wt/wt\%}$ . Nonetheless,  $\text{H}_2\text{O-TiO}_2$  seems slightly better (thermal performance enhancement of 0.0005% against  $\text{H}_2\text{O-Al}$ ). Therefore, the best design was obtained using the former nanofluid with  $\dot{S}_{gen,min} = 19.1045 \times 10^{-3} \text{ WK/WK}$  at  $G_{wf}^* = 0.1062 \times 10^{-3} \text{ m}^3/\text{s}$ ,  $\phi^* = 0.01 \text{ wt/wt\%}$ ,  $\alpha^* = 8.0375 \times 10^{-3}$  and  $\beta^* = 2.1948$ . Also, it is observed an evident data spreading when  $G_{wf}$  increases its value, which is related to the turbulent regime onset of the coolant flow.

Optimal Bejan's number ( $Be^* = \dot{S}_{gen,\Delta T}^*/(\dot{S}_{gen,min})$ ) for obtained designs are presented in Figure 2.10a. This dimensionless correlation is useful for estimating the contribution of heat transfer to total entropy production ( $\dot{S}_{gen,\Delta T}^*$ ), evidencing that  $\dot{S}_{gen,\Delta T}^*$  is greater than entropy due to fluid flow ( $\dot{S}_{gen,\Delta P}^*$ ), when the working fluid is flowing in laminar regime, *i.e.*,  $G_{wf} < 0.6 \times 10^{-3} \text{ m}^3/\text{s}$ . Otherwise, *i.e.*, a turbulent coolant flow, a larger pressure

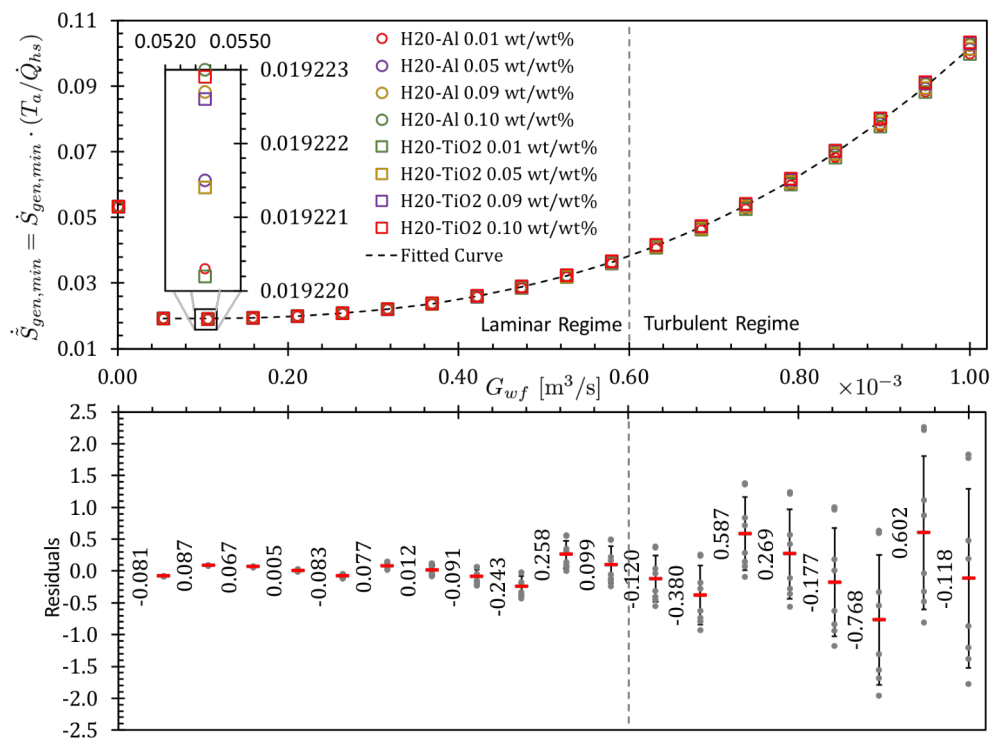


Figure 2.9. Minimal dimensionless entropy generation rate ( $\dot{S}_{gen,min}$ ) for some volume flow rate ( $G_{wf}$ ) values as design specifications, and using two colloids as coolants,  $H_2O-Al$  and  $H_2O-TiO_2$ , with different nanoparticle concentrations ( $\phi$ ).

drop appears throughout the system. Consequently, additional pumping power is required to maintain the coolant flowing at the specified volume flow rate. This means that an amount of entropy is generated due to fluid flow. In other words, the system wastes useful power. Hence, the coolant flows in turbulent regime ( $Be^* < 0.5$ ) for  $G_{wf} > 0.6 \times 10^{-3} \text{ m}^3/\text{s}$ . Moreover, Figure 2.10b presents Reynolds's numbers ( $Re_{D_h}^*$ ) for each design. There is an abrupt change in the behaviour of  $Re_{D_h}^*$ , as a function of  $G_{wf}$ , when the nanofluid flows in the turbulent regime. It is important to mention that the gap of  $Re_{D_h}^*$  from 1000 to 3000 can be attributed to the transition regime; although, in this work it was disregarded from the system operating conditions.

Subsequently, Figure 2.11 shows the optimal equivalent thermal resistance ( $R_{eq}^*$ ) of a RMCHS, for several designs found in this work. It is easy to notice a minimal value of  $R_{eq}(G_{wf})$  is  $0.113518 \pm 10^{-6} \text{ K/W}$ , when  $G_{wf} \approx 0.1587 \times 10^{-3} \text{ m}^3/\text{s}$ , in the laminar hydrodynamic regime, and for all used coolants. However,  $R_{eq,min}$  differs from the optimal value given by the  $\dot{S}_{gen}$  minimal value,  $R_{eq}^* = 0.113805 \pm 1.19 \times 10^{-6} \text{ K/W}$ . Moreover, in accordance with the common expectation, larger values of  $R_{eq}^*$  were found in turbulent regime. Lastly, Figure 2.12 presents the relationship between  $R_{eq}^*$  and optimal total pumping power ( $\Phi^* = G_{wf} \Delta P^*$ ) for each design scenario, yielding the designs displayed in Figure 2.9. This is an alternative representation based on a Pareto's front that highlights the  $R_{eq}^*$  and  $\Phi^*$  trade-off. The best reached results, according to the second law of thermodynamics, are observed in the zooming box of Figure 2.12.

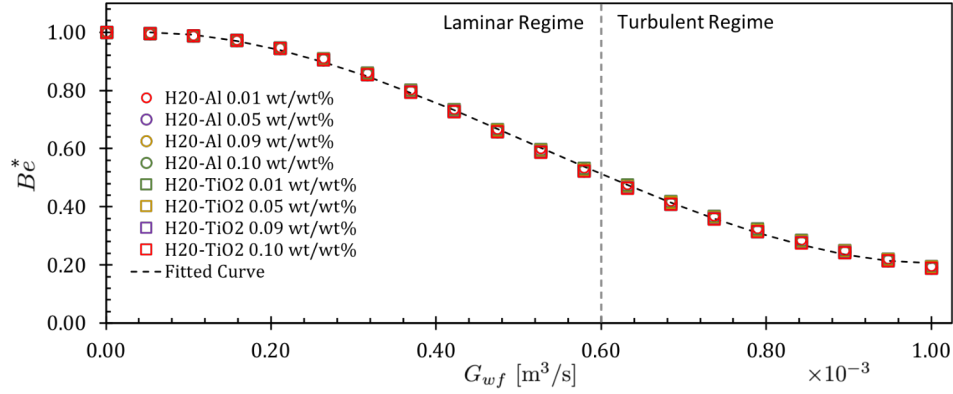
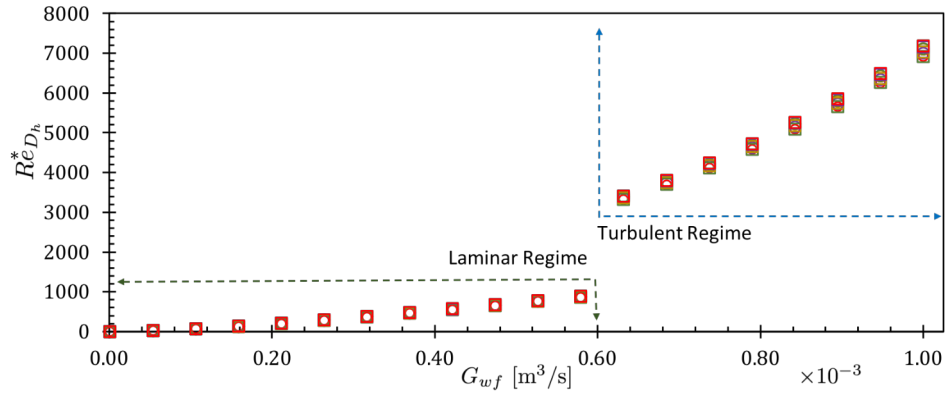
(a)  $Be^* = \dot{S}_{gen,\Delta T}^* / (\dot{S}_{gen,min}^*)$  vs.  $G_{wf}$ (b)  $Re_{D_h}^*$  vs.  $G_{wf}$ 

Figure 2.10. Optimal (a) Bejan's ( $Be^*$ ) and (b) Reynolds's ( $Re_{D_h}^*$ ) number, for some volume flow rate ( $G_{wf}$ ) values as design specifications, and using two colloids as coolants, H<sub>2</sub>O-Al and H<sub>2</sub>O-TiO<sub>2</sub>, with different nanoparticle concentrations ( $\phi$ ).

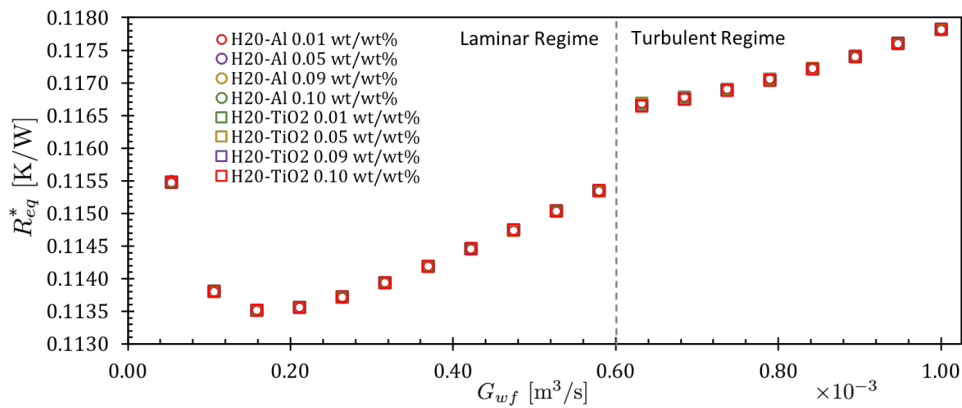


Figure 2.11. Optimal equivalent thermal resistance ( $R_{eq}$ ) of the rectangular microchannel heat sink for some volume flow rate ( $G_{wf}$ ) values as design specifications, and using two colloids as coolants, H<sub>2</sub>O-Al and H<sub>2</sub>O-TiO<sub>2</sub>, with different nanoparticle concentrations ( $\phi$ ).

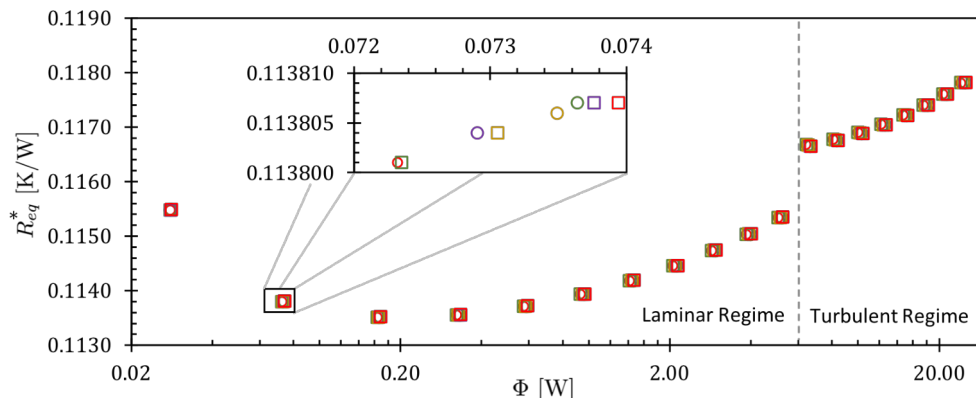


Figure 2.12. Optimal equivalent thermal resistance ( $R_{eq}^*$ ) compared against optimal total pumping power ( $\Phi^*$ ) of the system, for some volume flow rate ( $G_{wf}$ ) values as design specifications, and using two colloids as coolants,  $H_2O$ -Al and  $H_2O$ - $TiO_2$ , with different nanoparticle concentrations ( $\phi$ ).

#### 2.4.5 Case 4: Si- and HTCG-based RMCHS with air and $NH_3$

Figure 2.13 shows the optimal values of design parameters  $G_{wf}$ ,  $\alpha$  and  $\beta$ , corresponding to  $\dot{S}_{gen,min}$ . In other words, that such parameters minimise entropy production of the microchannel heat sink. Each one of the plotted markers correspond to an optimal design for all combinations of build materials, such as silicon (Si) and High Thermal Conductive Graphite (HTCG), and working fluids like air and ammonia gas ( $NH_3$ ).

Likewise, Figure 2.14a presents the minimal entropy generation rate ( $\dot{S}_{gen,min}$ ) for each one of the obtained designs. Values are plotted for different electronic power dissipation ( $\dot{Q}_{hs}$ ) levels. As observed, the entropy generation rate increases (as expected) whilst the net heat power is augmented. There is also a noticeable difference when choosing a different material (*i.e.*, Si or HTCG) to build the MCHS. This effect is also evident when choosing a different fluid (*i.e.*, Air or  $NH_3$ ) to act as a coolant. The combination HTCG- $NH_3$  laid out best results in terms of minimal entropy production, overcoming the traditional combination of Si-Air, which corroborates reported results in the literature. Moreover, Figure 2.14a evidences the influence of implementing a certain material or fluid. For high power applications, *i.e.*, beyond 60 W, this effect becomes more evident.

This influence is strongly reflected on the behaviour of the optimal equivalent thermal resistance ( $R_{eq}$ ). Figure 2.14b shows data for each fluid. In this figure,  $R_{eq}$  decreases when  $\dot{Q}_{hs}$  increases to avoid an excessive increment of temperature inside the electronic package, and reducing the overall effects due to irreversibilities in the MCHS. Furthermore, optimal difference temperature values of  $\Delta T$  can be calculated from the  $R_{eq}$  data (Figure 2.14b), using (2.33). These values are presented in Figure 2.14c. Such information complements the minimal entropy production reached from the design procedure. Besides, it is a practical and measurable quantity, which describes the thermal management system's performance.

Figure 2.15a displays results from the forward problem, in terms of  $\Delta T$ , contaminated with additive white Gaussian noise (AWGN), to emulate a measured dataset. We employed several values of signal-to-noise ratio (SNR [dB]) to analyse the performance of our approach under different scenarios. The measured temperature difference is identified as  $\Delta T_m$ . Figure 2.15b presents results from the inverse heat transfer problem, where  $\Delta T_e$  is the estimated temperature difference. Furthermore, estimated film coefficients are shown in Figure 2.16. Striving to complement our data, Table 2.8 summarises the root-mean-square

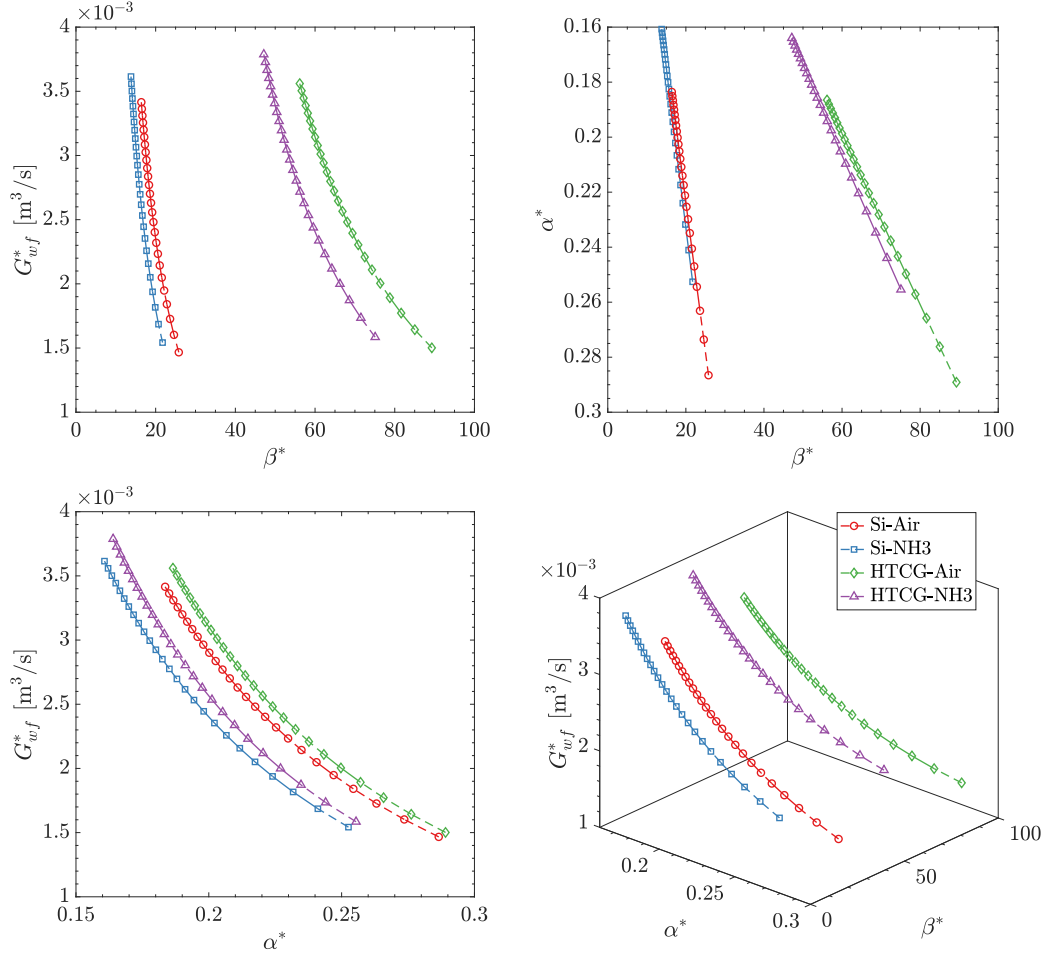


Figure 2.13. Optimal values reached for the design variables: the volume flow rate ( $G_{wf}^*$ ), channel aspect ratio ( $\alpha^*$ ), and channel-wall ratio ( $\beta^*$ ); assuming different scenarios varying the net heat power dissipation ( $\dot{Q}_{hs}$ ) from the electronic device.

error (RMSE) for each combination of material and fluid, and for all noise levels.

Table 2.8: Root-mean-square error of the estimated film heat transfer coefficient,  $RMSE\{h_e\}$  [ $\text{W}/\text{m}^2\cdot\text{K}$ ], varying the net heat power  $\dot{Q}$ , in different scenarios of heat sink material and working fluid.

SNR [dB]	$RMSE\{\bar{h}_e\}$ [ $\text{W}/\text{m}^2\cdot\text{K}$ ]			
	Si-Air	Si-NH <sub>3</sub>	HTCG-Air	HTCG-NH <sub>3</sub>
Noiseless	0.000	0.002	0.000	0.001
40	2.045	1.641	0.274	0.338
30	3.167	7.517	0.695	0.991
20	8.545	72.222	5.794	4.395
10	12.481	27.545	5.327	10.001
5	19.284	33.777	6.224	10.702

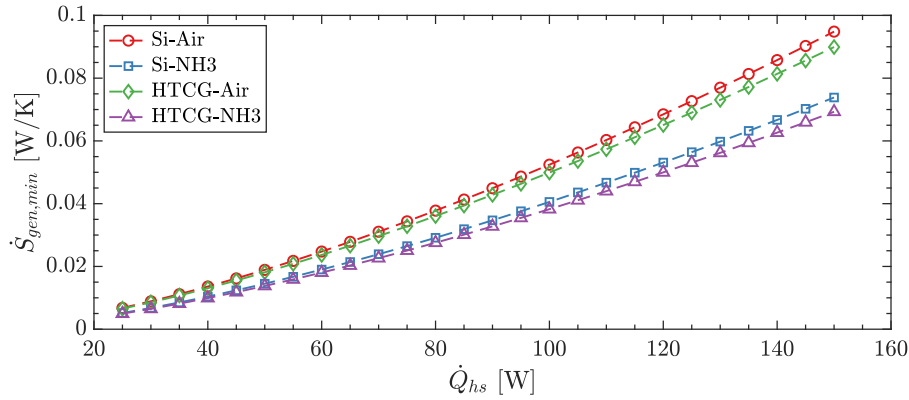
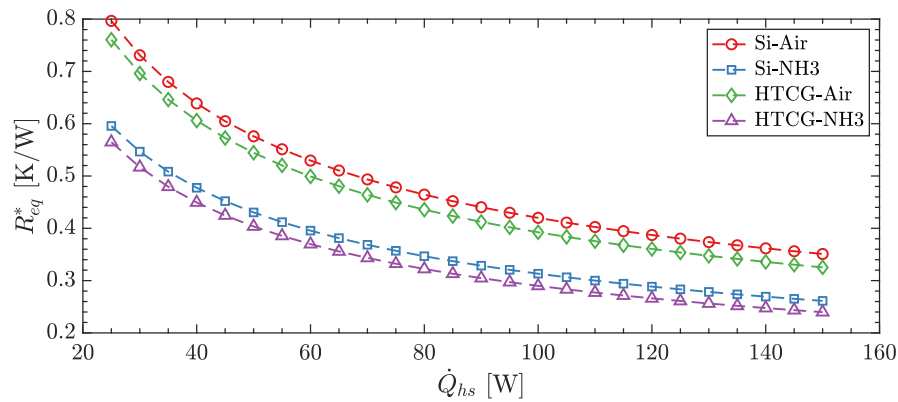
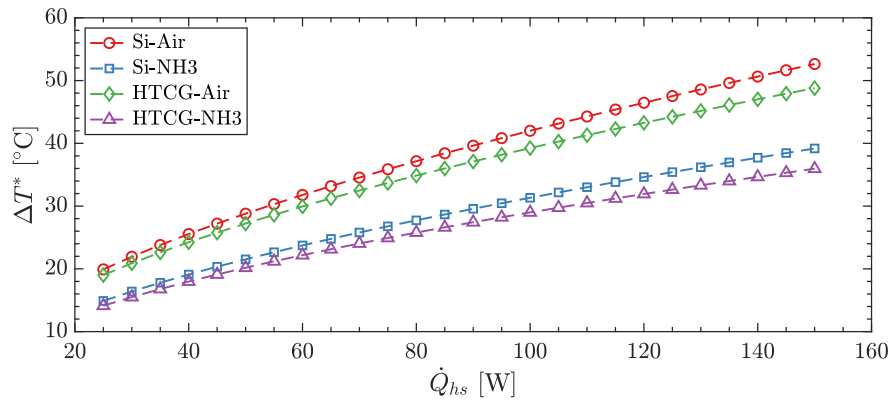
(a)  $\dot{S}_{gen,min}$  vs.  $\dot{Q}_{hs}$ (b)  $R_{eq}^*$  vs.  $\dot{Q}_{hs}$ (c)  $\Delta T^*$  vs.  $\dot{Q}_{hs}$ 

Figure 2.14. (a) Minimal entropy generation rate ( $\dot{S}_{gen,min}$ ), and optimal values of (b) the equivalent thermal resistance ( $R_{eq}^*$ ) and (c) the finite difference of temperatures ( $\Delta T^*$ ), assuming different scenarios varying the neat heat power dissipation ( $\dot{Q}_{hs}$ ) from the electronic device.

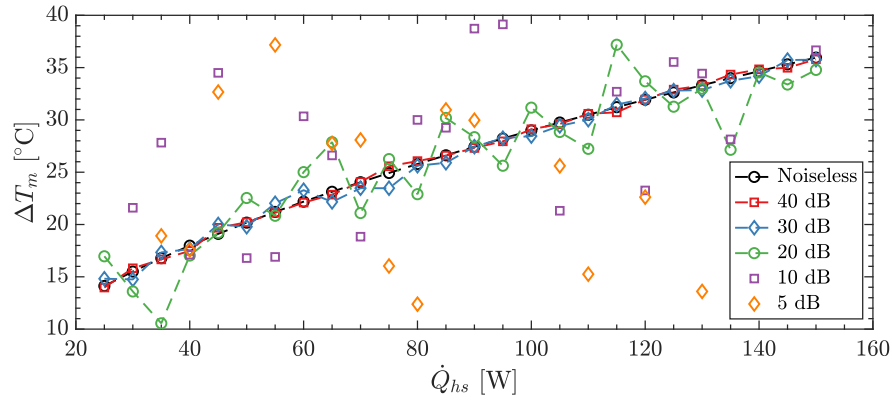
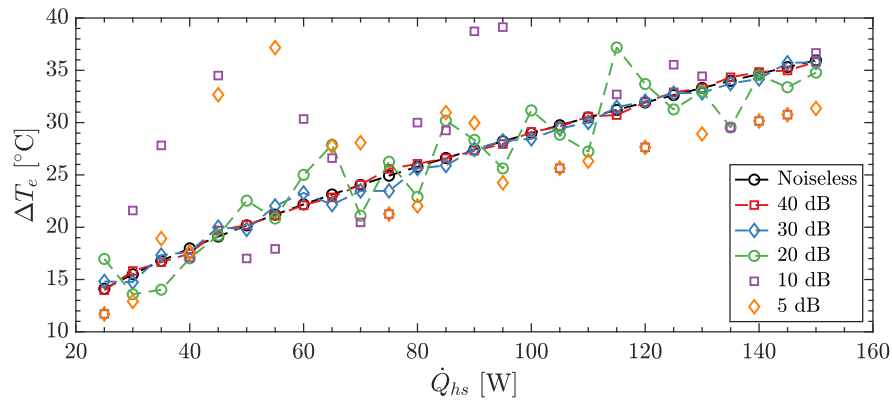
(a)  $\Delta T_m$  vs.  $\dot{Q}_{hs}$ (b)  $\Delta T_e$  vs.  $\dot{Q}_{hs}$ 

Figure 2.15. Finite differences of temperatures: (a) measured ( $\Delta T_m$ ) and (b) estimated ( $\Delta T_e$ ), assuming different scenarios varying the neat heat power dissipation ( $\dot{Q}_{hs}$ ) from the electronic device, and with several values of noise (SNR [dB]).

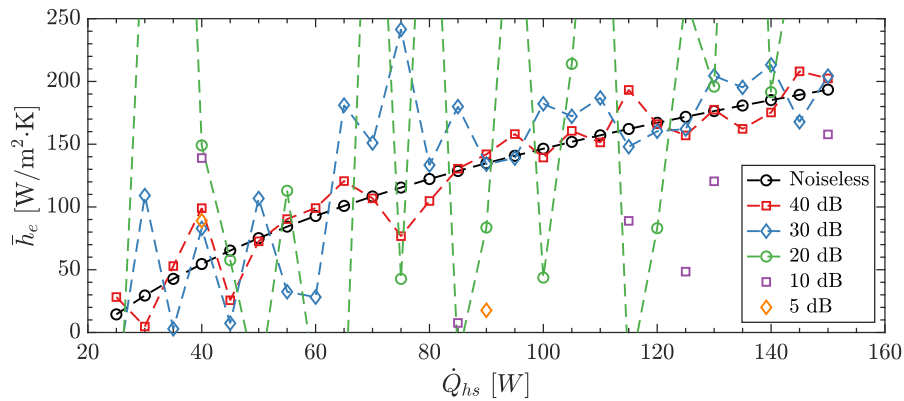


Figure 2.16. Estimated film heat transfer coefficient ( $\bar{h}_e$  [W/m<sup>2</sup>.K]) assuming different scenarios varying the neat heat power dissipation ( $\dot{Q}_{hs}$ ) from the electronic device, with several values of noise (SNR [dB]).

## 2.5 Conclusions

In this chapter, an optimal designing strategy for microelectronic thermal management applications was studied. This methodology is based on the entropy generation minimisation (EGM) criterion and modern optimisation methods, such as Unified Particle Swarm Optimisation (UPSO), Cuckoo Search (CS) algorithm, and Deterministic Spiral Optimisation Algorithm (DSOA). As an illustrative example, the conceptual design of an optimal microelectronic cooling system, a rectangular microchannel heat sink, was studied by using this alternative thermodynamic optimisation procedure, considering multiples conditions and scenarios. Those were grouped in four cases of study.

In *Case 1*, heat sinks made of aluminium that used air and environmentally friendly ammonia ( $\text{NH}_3$ ) as feasible working fluids, were analysed. Operating conditions were defined for different volume flow rates, and DSOA was implemented. It was observed that, under the scenarios we considered, optimal heat sinks using  $\text{NH}_3$  performed about 17 % better than those using air. Moreover, it is noticed that the thermal resistance related to the working fluid represents about  $52 \pm 16$  % of the total equivalent thermal resistance, whilst the thermal resistance related to convection phenomena only represents about  $12 \pm 6$  %. Hence, it is considered vital to select an appropriate working fluid to use in heat sinks, and also a material for the interface between the chip and the heat sink. Finally, it is important to remark that the proposed strategy stands as a good approach for determining the geometry and the volume flow rate that optimise the operation of a heat sink.

In *Case 2*, it was considered a heat sink body made of High Thermal Conductive Graphite (HCTG); air, ammonia gas ( $\text{NH}_3$ ) and  $\text{H}_2\text{O-TiO}_2$  as working fluids; nanoparticle volume fractions of 0.01, 0.05, 0.09, 0.1, 0.5 and 0.9 wt/wt%; and volume flow rates ( $G_{wf}$ ) between  $1.0 \times 10^{-5}$  and  $1.0 \times 10^{-2}$   $\text{m}^3/\text{s}$ . Besides, it was found too that, for the present case, entropy generation rate is minimal for  $G_{wf} \approx 4.5 \times 10^{-3}$   $\text{m}^3/\text{s}$  when using air and  $\text{NH}_3$  as coolants. However, whilst using  $\text{H}_2\text{O-TiO}_2$  the minimal value of  $\dot{S}_{gen}$  appeared around  $9.0 \times 10^{-5}$   $\text{m}^3/\text{s}$ , for all volume fractions considered.  $\dot{S}_{gen,min}$  obtained with nanofluids is lower, or at least equal to, values achieved with air and ammonia gas for  $G_{wf} \leq 1.0 \times 10^{-3}$   $\text{m}^3/\text{s}$ . Hence, it was also noticed that nanofluids represent a good choice of working fluid for designs with lower volume flow rates. For the opposite scenario, traditional fluids ensure efficient operation. Afterwards, it was observed that nanoparticle volume fraction is an important design specification, because it exhibited an crucial role on increasing entropy generation rate, or the system irreversibilities. Thus, the best design in terms of the second law of thermodynamics was achieved using a nanoparticle volume fraction of 0.01 wt/wt%, with channel aspect ratio of  $\alpha^* = 7.1765 \times 10^{-3}$ , channel-wall ratio of  $\beta^* = 2.17177$  and volume flow rate of  $G_{wf}^* = 89.30 \times 10^{-6}$   $\text{m}^3/\text{s}$ . Additionally, the performance of each optimisation technique for solving the thermal problem of designing was addressed in this case of study. Cuckoo Search algorithm showed to be more accurate and faster than the other two, but the Unified Particle Swarm Optimisation method still represents an alternative strategy to microchannel heat sink designing.

In *Case 3*, two colloidal fluids were studied as coolants, *i.e.*,  $\text{H}_2\text{O-Al}$  and  $\text{H}_2\text{O-TiO}_2$  with nanoparticle volume fractions ( $\phi$ ) of 0.01, 0.05, 0.09, and 0.10 wt/wt%, and volume flow rate ( $G_{wf}$ ) values between 0 and  $10^{-3}$   $\text{m}^3/\text{s}$ . Several optimal designs under different scenarios were found in laminar and turbulent flow regimes. Data shows, as is expected, that all studied flowing nanofluids in laminar regime minimise the entropy production of the system, when  $G_{wf}$  is considered as a design variable. This inference ratifies the importance of using coolants in laminar regime for microelectronic heat sinking applications. Colloidal flows



in a turbulent motion require an additional amount of pumping power to maintain higher values of  $G_{wf}$ . That fact noticeably increases the minimal entropy generation rate. It was also found that for both nanofluids, smaller nanoparticle concentrations enhance overall system performance, and reduces the chance of agglomeration inside microchannels. The presence of nanoclusters increases the pressure drop that directly affects system efficiency [158]. In addition, titanium dioxide nanoparticles in water ( $\text{H}_2\text{O-TiO}_2$ ) demonstrated to be a good choice for coolant. Thus, the best design was achieved with 0.01 wt/wt% of  $\text{H}_2\text{O-TiO}_2$ , an optimal channel aspect ratio ( $\alpha^*$ ) of  $8.0375 \times 10^{-3}$ , an optimal channel-wall ratio ( $\beta^*$ ) of 2.1948 and an optimal volume flow rate ( $G_{wf}^*$ ) of  $0.1062 \times 10^{-3} \text{ m}^3/\text{s}$ . Additionally, the EGM-CS strategy proved to be a useful alternative for thermodynamic design, even considering two different hydrodynamic regimes.

Lastly, in *Case 4*, an alternative strategy for estimating convection heat transfer coefficients in electronic thermal management applications was explored. Such a strategy solves the associated inverse heat transfer problem (IHTP). In the present case, it was tackled this IHTP via the Cuckoo Search (CS) algorithm (CS), by minimising a cost function based on the least square error. This methodology was illustrated with a microchannel heat sink with several design conditions. Average convective heat transfer coefficients were estimated from several synthetic temperature measurements, with different noise levels. The reference's temperature data were obtained by solving the forward problem, based on the equivalent thermal resistance model of a previously designed microchannel. Hence, these designs were achieved through the entropy generation minimisation (EGM) criterion, also powered by CS, employing several specifications (material, working fluid and net heat power dissipation). Results agreed remarkably well for signal-to-noise ratios (SNR) above 30 dB, which can be reached with any modern temperature sensors.

## Chapter 3

# Non–Conventional Calorimeter

Microelectronic components are present in almost all actions in our lives nowadays, and their robustness and performance are the main care features during design and manufacture stages. *Failure chances cannot be allowed!*, especially due thermal issues. To avoid that, the heat power dissipation inherited to operating electronic components is attended by implementing specialised mechanical devices, *e.g.*, heat sinks. They were described in previous section, which included an alternative design methodology, several study scenarios and illustrative simulations. However, generic thermal power generation values are commonly assumed as a design condition, which makes an optimally designed heat sink *not-so-optimal* in the exergetic sense. This issue can be fulfilled if the microelectronic's practical heat power generation is measured and, hence, a heat sink or any thermal management device is specially designed for such component. There are multiples means for accomplish that task, as it was mentioned in Introduction. The directly determination of the power losses from a specific system is possible via *the calorimetric method* [78]. Many calorimeters have been implemented in the literature, most of them are specialised in the analysis of substances and their variations for biology, pharmaceuticals and chemistry applications [159, 160]. Those are employed for measuring energy changes on significantly small samples, for example: the heat produced by burning 3 g of glucose ( $C_6H_{12}O_6$ ) is about 50 kJ [79, 80]. Others are used for high energy particles such as the ATLAS calorimetry system at the Large Hadron Collider (LHC), with measurements in the range of 15 to 180 GeV (1 GeV equals  $1.6 \times 10^{-19}$  J), excessively high manufacturing/operating costs, and hugest dimensions [161]. Specifically, in the measurement of the microelectronic power dissipation, some enthalpy-based calorimeters have been proposed, mainly because their response time is shorter than the one of closed system [75, 76, 83]. This could be considered as a drawback because an additional pumping power to move the fluid flow(s) along heat exchangers is primordial. Nonetheless, a closed-calorimeters for small microelectronic circuits, with the test chamber immersed in a reservoir of distilled water, has been proposed in [81]. This device was based on the bomb calorimeter traditionally used for studying chemical reactions [159].

This chapter proposes a non-conventional calorimeter for the measurement of microelectronic power dissipation. The system consists in a horizontal cylindrical concentric cavity, based on the constant-volume calorimetry principle widely used in biology and chemical applications [79], and firstly implemented in electronic devices by Marin [81]. This system is entirely based on heat transfer due natural convection as a first approach and avoiding the use of external power sources. The system's design and its prototype construction are described, as well as the numerical simulation and the experimental implementation.

Several simulations were conducted chiefly to find locations for temperature sensors, and to observe the heat transfer behaviour inside the system. Results obtained were used in the implementation and instrumentation of the calorimeter. Then, the practical experiment corroborated the expected behaviour and gave us a device capable of determine power dissipation values from 1 W to 20 W of microelectronic devices. The non-conventional calorimeter completes the alternative microelectronic thermal management strategy proposed in this research work.

The chapter is organised as follows: First section describes basic concepts related with calorimetry; Second one presents the proposed design and its construction; Third section discusses the numerical simulations; subsequently, the system's implementation is described; finally, the most remarkable inferences are summarised as Conclusions.

### 3.1 Foundations

The principle of calorimetry is based on a generalisation of the classic Joule’s paddle-wheel experiment, which showed the relationship between thermal and mechanical energy, and the notion of the specific heat discovered by J. Black [162]. Hence, it is appropriate start remembering with the specific heat value ( $c$  [J/kg·K]) of a substance or system, at a given reference temperature ( $T_a$ [K]),

$$c \triangleq \left( \frac{\partial u}{\partial T} \right)_{T_a}, \quad (3.1)$$

since  $u$  [J/kg] is the specific internal energy, and  $T$  [K] is its absolute temperature. This notion describes the how much energy (heat) is required to raise the temperature of an body (*e.g.* water) per unit of mass, or volume (under certain conditions). Therefore, *calorimetry* consists of determining the power generated in a real process, by measuring changes of temperature in a “energy storage” body with known thermophysical properties [78–81]. It can be assumed as uniformly and isothermally in function of time to simplify its analysis, with a insignificant loss of accuracy [127]. Thus, the substance behaviour is modelled by using the lumped capacitance method, which consists on represent the thermal system as an electrical circuit [125, 163]. It is represented by a parallel  $RC$ -circuit, where  $\dot{Q}$  [W] is the effective thermal power inwarding the system (current source),  $\theta = T - T_a$  [K] is the temperature difference of the working fluid (voltage), and  $C$  [J/K] is the thermal capacity model. The fluid temperature,  $T$  [K], is assumed time-dependent, and  $T_a$  [K] indicates the ambient temperature. In a more detailed conceptualisation of this system an equivalent thermal impedance  $Z$  [K/W] could be defined. However, a simplest model which includes an equivalent thermal resistance  $R$  [K/W] is implemented in this work, mainly due to the expected slow thermal behaviour. Figure 3.1 depicts the studied system under two points of view, such as the thermodynamic closed-system sketch and the circuit analogy diagram.

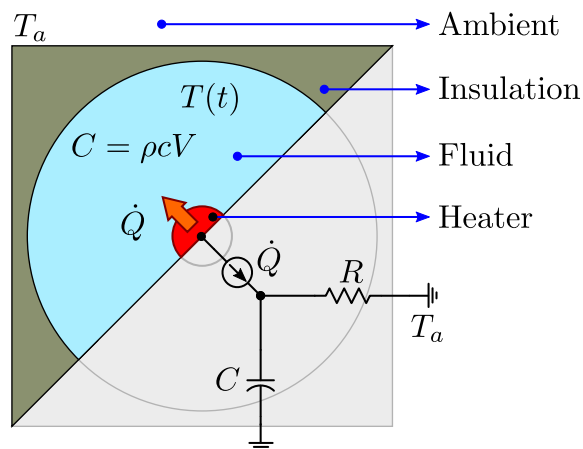


Figure 3.1. Sketches of the studied system and its circuit analogy.

It is natural to obtain an alternative version of the first law of thermodynamics by analysing the main node  $\theta$ , under the circuit theory sense, such as,

$$C \frac{d\theta(t)}{dt} + \frac{\theta(t)}{R} = \dot{Q}h(t), \quad (3.2)$$

since  $\mathfrak{h}(t)$  is the Heaviside step function. A well-known ordinary differential equation is reached by rearranging (3.2), as

$$\frac{d\theta(t)}{dt} + \frac{\theta(t)}{\tau} = \frac{\dot{Q}}{C}\mathfrak{h}(t), \quad (3.3)$$

where  $\tau = RC$  [s] is the time constant, and  $\dot{Q}/C$  [K/s] is the source magnitude. With the initial condition  $\theta(t=0) = 0$  s, this differential equation has the solution given by

$$\theta(t) = \frac{\tau\dot{Q}}{C} \left(1 - e^{-t/\tau}\right) \mathfrak{h}(t). \quad (3.4)$$

Now, it is possible to find two important features of this expression. The first one is the final value of (3.4),  $\theta_\infty$ , given by

$$\theta_\infty = \lim_{t \rightarrow \infty} \theta(t) = \frac{\tau\dot{Q}}{C} = \dot{Q}R. \quad (3.5)$$

That value is the steady-state response of the system, and it can be also reached from the traditional electrical circuit analysis. Whereas, the second feature is observed from the first derivative of  $\theta(t)$  at  $t = 0$  s, such as,

$$\left. \frac{d\theta(t)}{dt} \right|_{t=0 \text{ s}} = \frac{\theta_\infty}{\tau} = \frac{\dot{Q}}{C}. \quad (3.6)$$

It says that the first slope of  $\theta(t)$  contains information about its time constant and final value, directly related with the heat power magnitude and the thermal capacity. This is important fact could be used for practical implementations where the entire system has been previously characterised, *i.e.*,  $C$  [J/K] is known. Plus, by writing (3.4) in terms of  $\theta_\infty$  from (3.5), and approximating the exponential function with its Maclaurin series truncated at two terms, it yields

$$\theta(t) \approx \frac{\theta_\infty}{\tau}t, \quad t \ll \tau, \quad (3.7)$$

which is the tangent line linked to the first slope described in (3.6).

Straightforward, the above mentioned features give place to relationships concerning with thermal resistance and capacitance models. The equivalent thermal resistance ( $R$  [K/W]) is calculated from (3.5), as shown,

$$R = \frac{\theta_\infty}{\dot{Q}}. \quad (3.8)$$

Its value can be approached by experimental or numerical data, or by using a comprehensive theoretical model based on heat transfer concepts. Many works have demonstrated that  $R$  chiefly includes heat transfer mechanisms as convection and conduction [125, 127]. Nonetheless, expression from (3.8) only describes the thermal resistance when the characterised substance is fully charged, *e.g.*, overheated water vapour.

Subsequently, the thermal capacity ( $C$  [J/K]) model can determined from its correlation with  $\tau$  in (3.6),

$$\left. \frac{d\theta(t)}{dt} \right|_{t=0 \text{ s}} = \frac{\theta_\infty}{\tau} = \frac{\dot{Q}}{C}, \quad (3.9)$$

taking in mind that  $\dot{Q} = \delta Q/dt$ ,  $d\theta/dt = dT/dt$ , and  $T_a = T(t = 0 \text{ s})$ , such as,

$$C = \left. \frac{\delta Q}{dT} \right|_{T_0}, \quad (3.10)$$

which is an equivalent form of the heat capacity definition (3.1) [163]. On that,  $C$  is interpreted as the incremental change of the system thermal energy ( $\delta Q$  [J]) due to a change on its temperature ( $dT$  [K]) [163]. Equation (3.10) can be simplified to a more practical formula by employing thermodynamic foundations, *i.e.*, the first law. Hence, representing the calorimeter as a closed quasi-static thermodynamic system the energy balance is given by,

$$dU = \rho V c dT = \delta Q, \quad (3.11)$$

where  $dU = \rho V du$  [J] is the internal energy change due to the amount of  $\delta Q$  entering to the system. Therefore, a simple expression of  $C$  is found by using (3.11) and (3.10), as shown,

$$C = \rho c V. \quad (3.12)$$

It was assumed that the properties like volume ( $V$  [m<sup>3</sup>]), mass density ( $\rho$  [kg/m<sup>3</sup>]), and specific heat ( $c$  [J/kg·K]), are known at a reference temperature  $T_a$  [K]. Also, the system was supposed as an incompressible substance with constant volume, *i.e.*, a liquid fluid like water, and its boundaries were considered as adiabatic, impermeable, and rigid.

In addition, it is important to observe the above discussed model when the system is assumed isolated, *i.e.*, an ideal performance. Isolation is reached when  $R \rightarrow \infty$ , then (3.3) becomes in

$$\frac{d\theta(t)}{dt} = \frac{\dot{Q}}{C} \mathfrak{h}(t), \quad (3.13)$$

with  $\theta(t = 0) = 0$  K,  $\dot{Q}/C \geq 0$  K/s, and  $C = \rho c V$  from (3.12). It indicates the temperature slope is directly related with the heat power entering to the known system, with  $\rho$ ,  $V$  and  $c$ , without any power leakage. Therefore, the ideal performance of a calorimeter allow us to determine directly the power losses using only thermophysical properties of the working fluid, and the temperature variations in a finite time test, primarily to avoid an inevitable blow-up. This behaviour is impossible to be reached in practical engineering, nonetheless, a good insulated system could be near this performance.

### 3.2 Design and construction

Multiple geometries and sensing methodologies have been implemented since the first calorimeter was reported in 1780 by Lavoisier and Laplace [160], but the general principle of calorimetry remains the same as it was discussed in the prior section. A calorimeter is composed by two essential parts: the sample or device under analysis (DUA) and the surroundings or absorber body. In physics, the simplest and optimum geometry for almost all structures is a sphere, thus it is easy to figure out a calorimeter formed by two concentric spheres. This geometry is considered idealistic due to the associated difficulty to build it in practice and, even more complicated, due to the almost impossible means to measure the temperature changes inside the absorber body. Another crucial fact from this simplest geometry is how the DUA is going to be placed inside the apparatus, and how the Earth's gravity would interact with the whole system. Sacrificing a little simplicity, the cylindrical geometry is laid out as the feasible and optimal one in practical engineering terms. The vertical cylinder or bomb calorimeters are commonly used in several applications with small substances [159, 160], otherwise, for greater samples or DUAs the rectangular parallelepiped structures are preferred [76, 81, 84, 85, 164]. Nonetheless, those calorimeters work based on forced convection and measuring the enthalpy variation of a flowing coolant. In this work, we propose a non-conventional calorimeter using a horizontal cylindrical geometry and based on natural convection, without external power sources for the system's operation. This position was chosen to take advantage of the Earth's gravity and the surface's symmetry to "adsorb" the heat flux. Such geometry is also used by LHC's calorimeters, but the operating principle is quite different. Figure 3.2 shows the proposed non-conventional calorimeter for the power dissipation measurement of electronic devices.

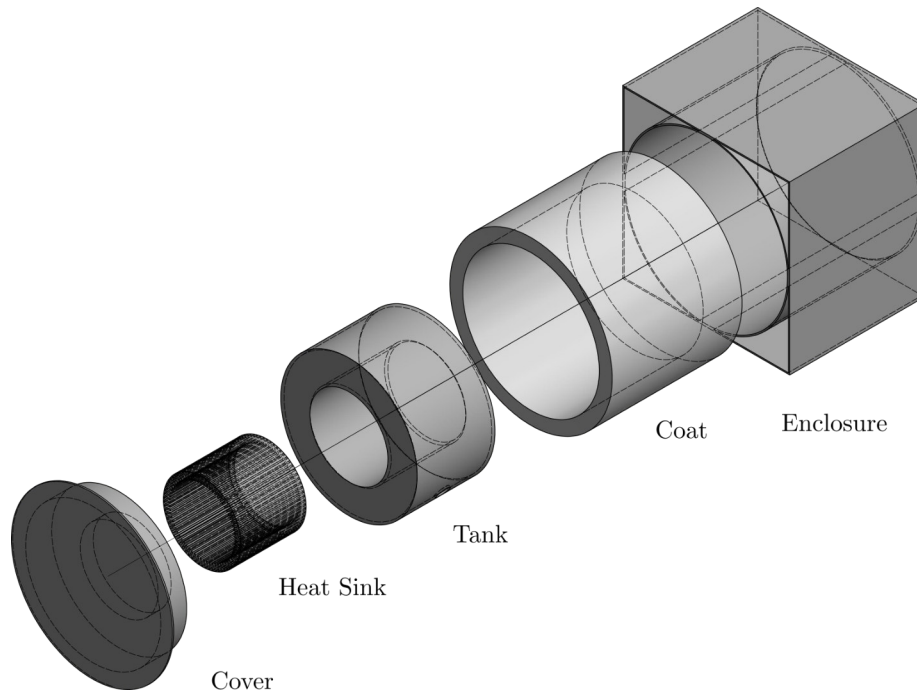


Figure 3.2. Exploded view of the proposed non-conventional calorimeter

The system is composed of five main parts (Figure 3.2), which are detailed as follows.

*Enclosure*: it is the outer part of the entire system in contact with the ambient, and serves as its structural support. This component is a rectangular parallelepiped with an inner cylinder to contain the system's components, and made of a high structural resistance material. Figure 3.3 presents the geometry defined for the *Enclosure*.

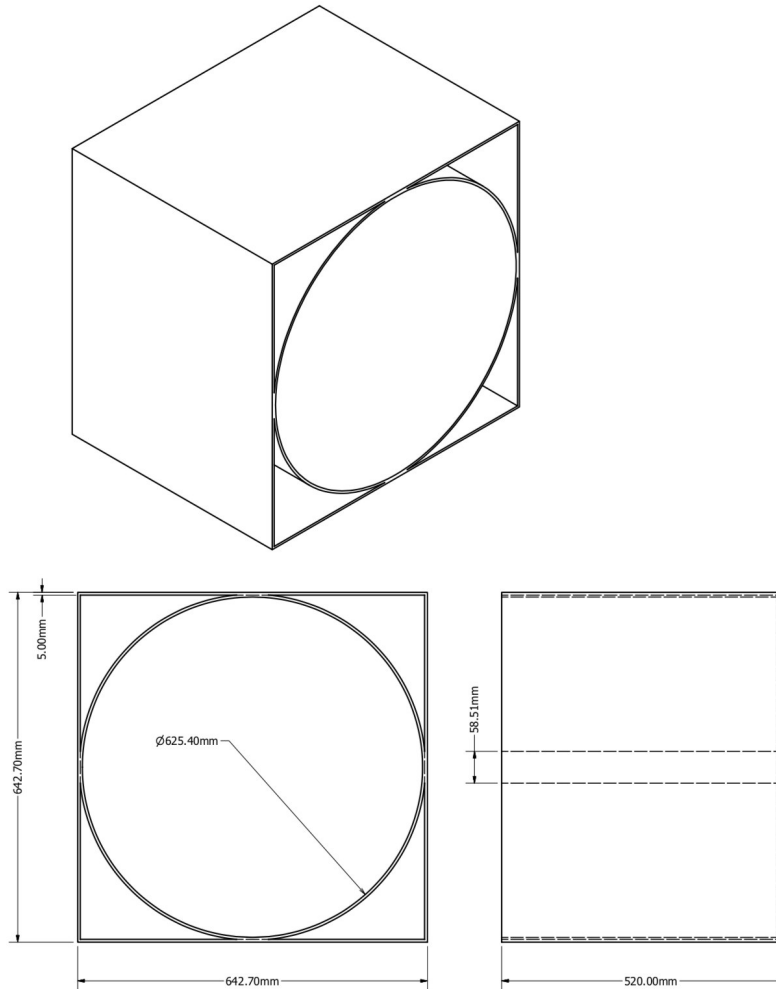


Figure 3.3. Detailed geometry of the *Enclosure*: the calorimeter's component, which contains the other parts and gives structural resistance for the entire system. All units are in millimetres [mm].

*Coat*: it is the main thermal insulation layer between the *Tank* filled with the heat absorbing fluid and the *Enclosure*. It is made of expanded polyurethane and expanded polystyrene foams Figure 3.4 displays the geometry designed for the *Coat*.

*Tank*: it is an annular cylinder with its annulus volume empty to be filled by the working fluid and its centre contains the *Heat Sink* or *Core*. This part is made of an impermeable and high thermal conductive material, and it has the geometry specified in Figure 3.5a. Additionally to this part, a *Cap* to seal properly the *Tank* and to allow the pass of the waterproof temperature sensor's cables, was designed as Figure 3.5b shows.

*Heat Sink*: it is the main chamber or core, which consists on a radial plate-fin heat sink inside and concentric to the *Tank*. Its plate-fins are radial-uniformly spaced along the *Tank*'s inner radius. This component is made of a thermal conductive material to enhance



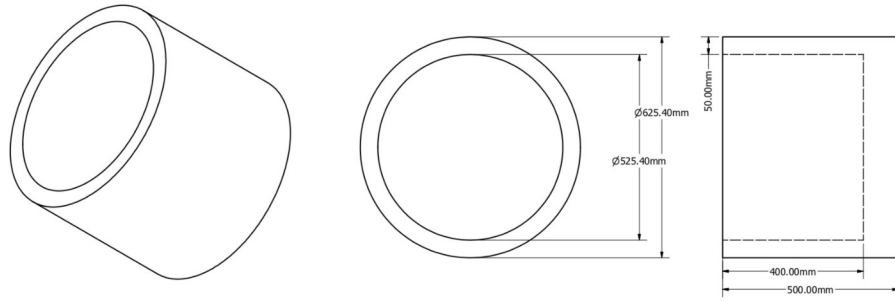


Figure 3.4. Detailed geometry of the *Coat*: the calorimeter's component, which thermally insulates the internal parts of the calorimeter. All units are in millimetres [mm].

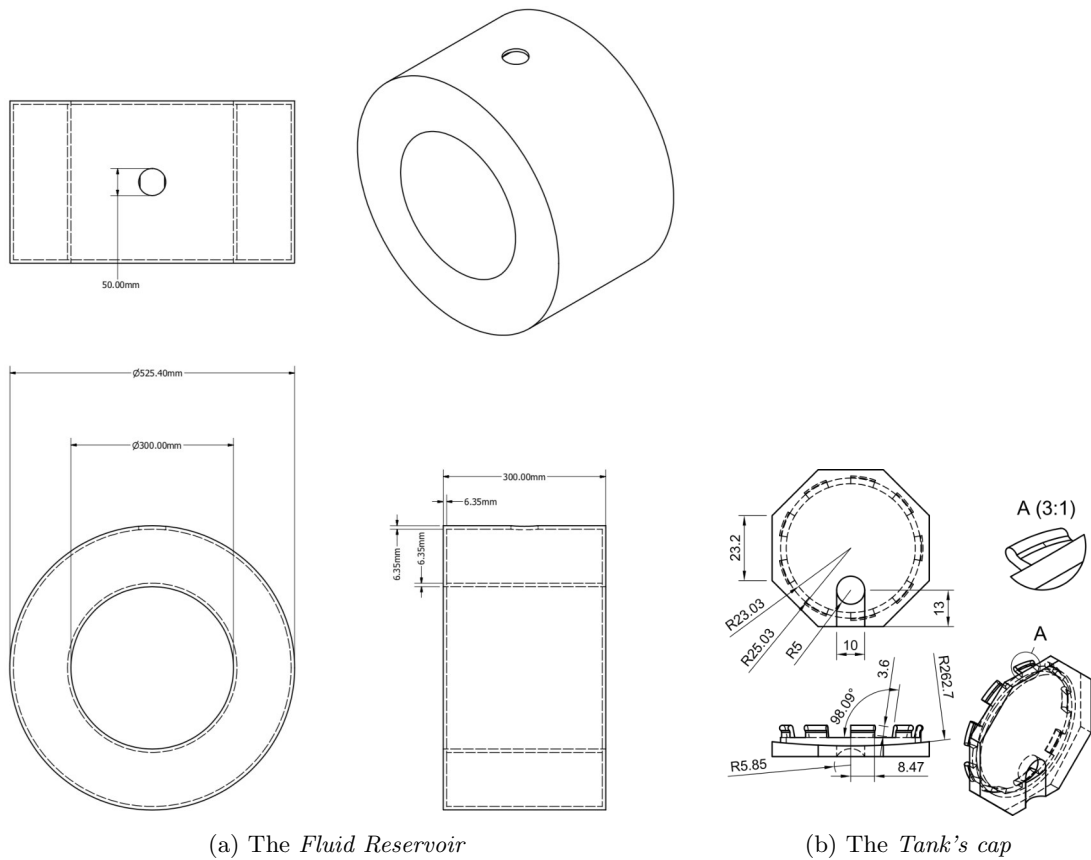


Figure 3.5. Detailed geometry of (a) the *Tank* or the *Fluid Reservoir*, and (b) the *Tank's cap*: the calorimeter's components, which contain the working fluid to be heated and avoid leakages. All units are in millimetres [mm].

the heat transfer from the DUA to the working fluid, since the former is placed inside this component. The detailed geometry for this part is plotted in Figure 3.6.

*Cover*: it is the thermal insulation between the main chamber (where is placed the DUA) and the exterior environment, it also serves as the system's entrance and contains the ports to supply the electrical power required by the DUA. It is made, at least, of two materials: a structural resistant and an insulator material, *e.g.*, laminated steel sheet and

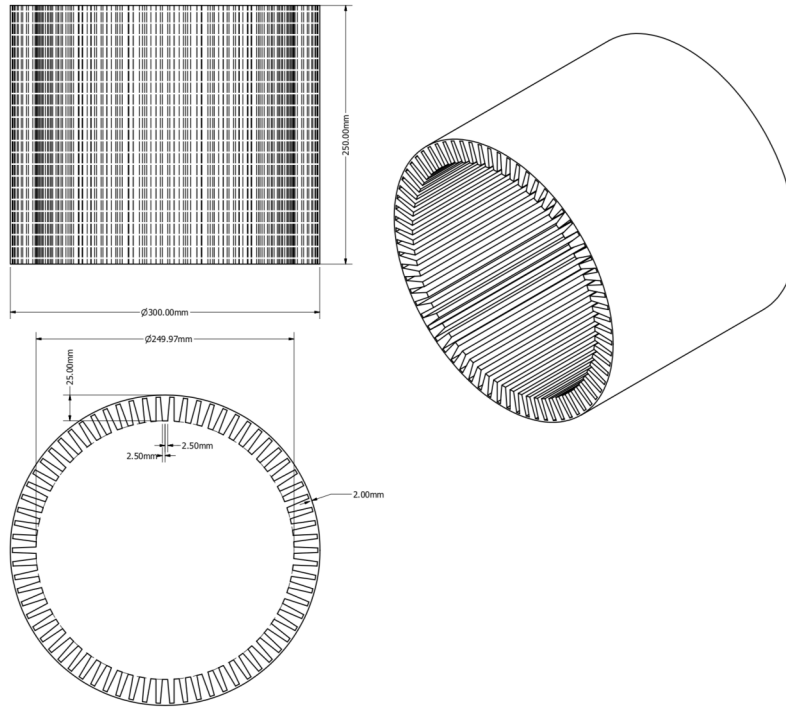


Figure 3.6. Detailed geometry of the *Main Chamber* or the *Radial Plate-Fin Heat Sink*: the calorimeter's component, which eases the heat transfer from the analysed electronic device to the working fluid. All units are in millimetres [mm].

expanded polystyrene foam, respectively.

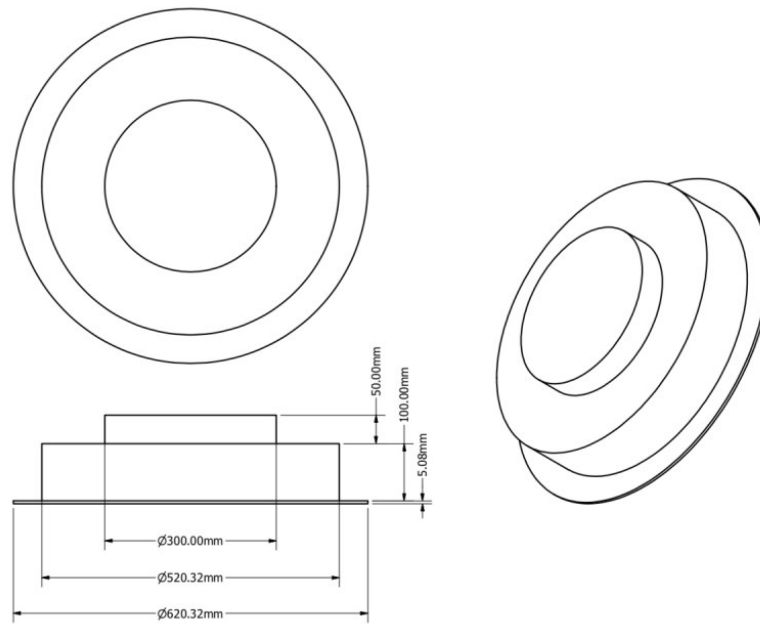


Figure 3.7. Detailed geometry of the *Cover*: the calorimeter's component, which thermally insulates the main chamber (the *Core*'s inside) of the calorimeter and, also serves as the door to place the DUA. All units are in millimetres [mm].

In an intermediate step between designing and manufacturing, the non-conventional calorimeter was prototyped in a scaled version for its revision and as illustrative purposes. It was done by utilising a MakerBot™ Replicator® Desktop 3D Printer (5th Generation), and polylactide (PLA) material. The main purpose of this stage was to revise and refine the structure and final assembly of the prototype. Figure 3.8 shows the 3D printed version of the calorimeter's components. The *Cap* to seal the *Tank* was fully built in real scale through additive manufacturing.

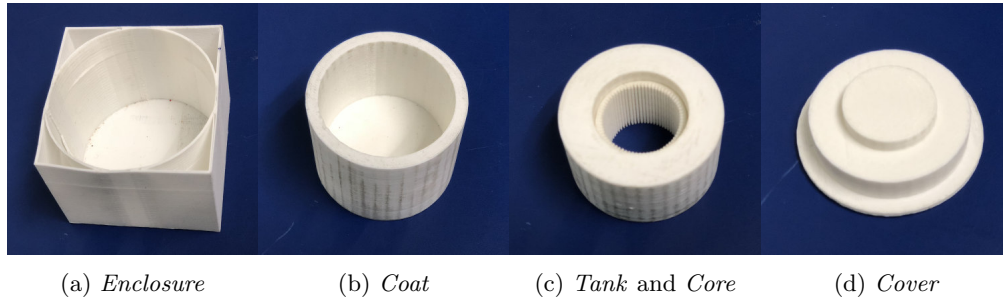


Figure 3.8. The designed non-conventional Calorimeter in a scaled version printed in polylactide (PLA) via additive manufacturing.

Subsequently, the Calorimeter's metal-based structures (*i.e.*, *Enclosure*, *Tank*, and *Core*) were manufactured by the *Grupo MADIVER SA de CV*, with headquarters in León (Guanajuato), employing the designs and specifications given above, and financially supported by the *Rectoría del Campus Irapuato-Salamanca*. Figure 3.9 shows the parts built just when they were delivered. Withal, the insulation parts such as *Cover* and *Cap* were constructed leaving the Calorimeter's plant ready to be instrumented. More details about the plant are presented in Table 3.1. The Calorimeter's plant was instrumented using six temperature sensors, Maxim Integrated™ DS18B20; three of them covered with waterproof stainless steel sheaths; and a minicomputer Raspberry Pi Zero W. Three sensors were installed in the main chamber (*Core*), to measure the temperature of air surrounding the DUA, and the others were submerged into the *Tank* filled with water. Specifications for these components are displayed in Tables 3.2 and 3.3.

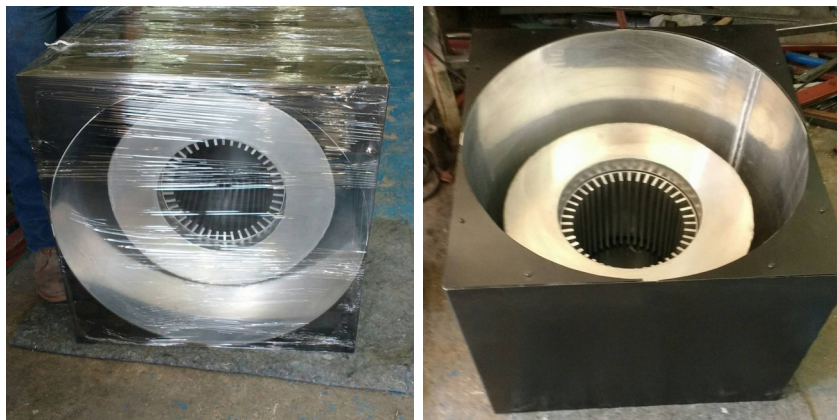


Figure 3.9. The manufactured calorimeter's parts: the *Enclosure* in Steel A36, and the *Tank* and *Core* in Aluminium 6061. Manufactured by the *Grupo MADIVER SA de CV*, León (Guanajuato).

Table 3.1: Specification of the Calorimeter's plant

Total volume	64.27 cm × 64.27 cm × 52.00 cm (214.79 dm <sup>3</sup> )
Chamber's size for DUT	25.56 cm of diameter and 30 cm of long (15.939 dm <sup>3</sup> )
Working fluid volume	41.431 L
Working fluid	Liquid Water
<i>Enclosure's</i> materials	Steel A36
<i>Coat's</i> materials	Expanded polystyrene and expanded polyurethane foams
<i>Tank</i> and <i>Core's</i> materials	Aluminium 6061
<i>Cover's</i> materials	Expanded polystyrene foam and laminated steel sheet

Table 3.2: Specification of the employed temperature sensor

Name	Programmable Resolution 1-Wire Digital Thermometer
Reference	DS18B20
Type	IC
Manufacturer	Maxim Integrated <sup>TM</sup> , Inc.
Range	from -55 °C to +125 °C
Accuracy	±0.5 °C from -10 °C to +85 °C
Resolution	Programmable from 9 Bits (0.5 °C) to 12 Bits (0.0625 °C)
Communication	1-Wire® using Only One Port Pin
Query time	750 ms for a 12 Bits resolution (0.0625 °C)
Power-on reset value	0x0550h (+85 °C)
Power supply	3.0 V to 5.5 V, parasitic power Mode with only 2 pins for operation
Multidrop capability	Each device has a unique 64-Bit serial code stored in On-Board ROM
Available packages	8-Pin SO, 8-Pin μSOP, and 3-Pin TO-92 (used)
Water proof package	Waterproof stainless steel sheath of 6 mm diameter and 35 mm long

Figure 3.10 depicts the acquisition, preprocess and distribution data system. As mentioned above, the device under analysis (DUA) is placed inside the *Core* and connected to the outside via the cords, which pass throughout the insulation *Cap*. During the DUA's operation, it heats the air enclosed in the chamber, and such energy is transferred from the DUA to the water stagnated in the *Tank*, due to the radial plate-fin heat sink and the *Tank* and *Core's* good thermally conductive material. Whilst this occurs, the sensors are reading temperature's changes in the *Core's* air and *Tank's* water, such information is registered by the minicomputer using Raspbian as the operating system, and a Python's program (running as a daemon). Then, an Octave's script is preprocessing the raw data and the Apache HTML server is publishing the experiment's current state to the local network. Parallely to the described procedure, users can access to such minicomputer using the SSH protocol for download the experiment's data, or any web browser (*e.g.*, Mozilla Firefox) for visualising the experiment's evolution. Therefore, the non-conventional calorimeter system has been built and the source codes developed in its implementation are available at the GitHub Repository: <https://github.com/jcrvz/cal-sys>. Figure 3.11 presents the internal structure of the constructed prototype (Figure 3.11a) and its external view whilst it is operating (Figure 3.11b)

Table 3.3: Specification of the minicomputer

Name	Raspberry Pi Zero W
Operating System	Raspbian (Debian optimised for the Raspberry Pi hardware)
SoC	Broadcom BCM2835
CPU	ARM1176JZF-S @ 1.0 GHz single-core
GPU	Broadcom VideoCore IV @ 250 MHz
SDRAM	512 MB (shared with GPU)
Storage Type	Flash storage (MicroSDHC)
Storage Capacity (Extendable)	8 GB
USB 2.0 ports	1 Micro-USB
Video outputs	Mini-HDMI, 1080p60
Audio outputs	Mini-HDMI, GPIO
Network	802.11 b/g/n wireless LAN, Bluetooth 4.1 (BLE)
Low-level peripherals	17x GPIO and HAT ID bus
Power source	5 V via MicroUSB or GPIO header
Power rates	from 100 mA (0.5 W) to 350 mA (1.75 W)
Dimensions and Weight	65 mm × 30 mm × 5 mm, 9 g
Accessories	Canakit™ Case and plate-fin heat sink

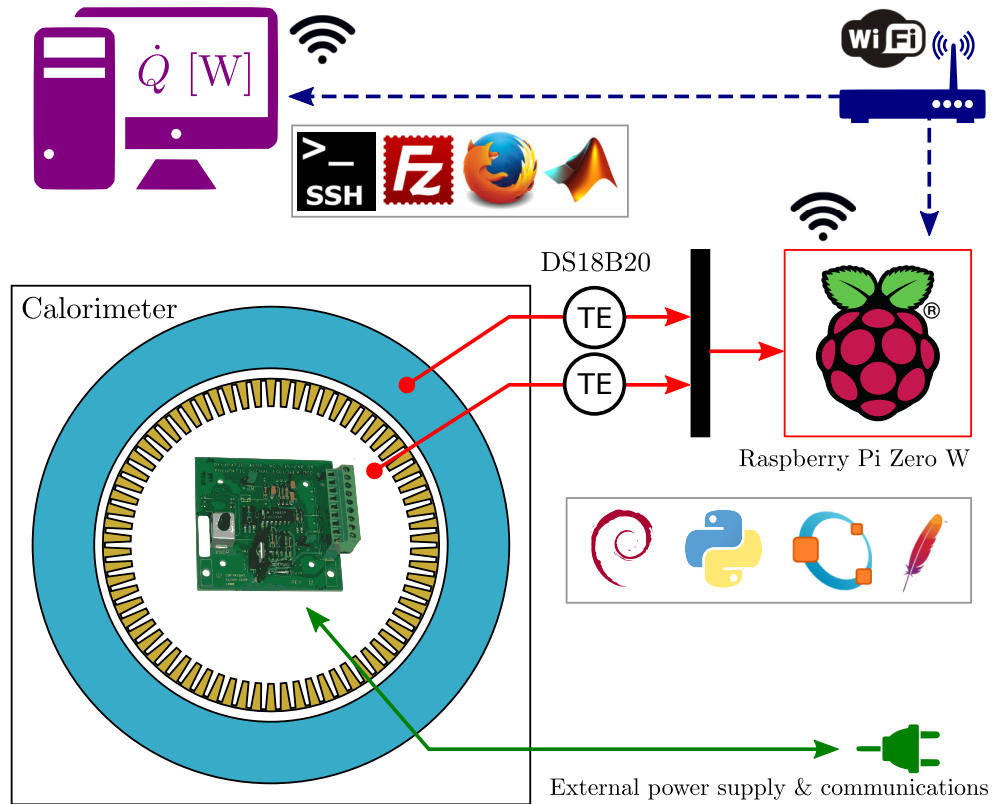
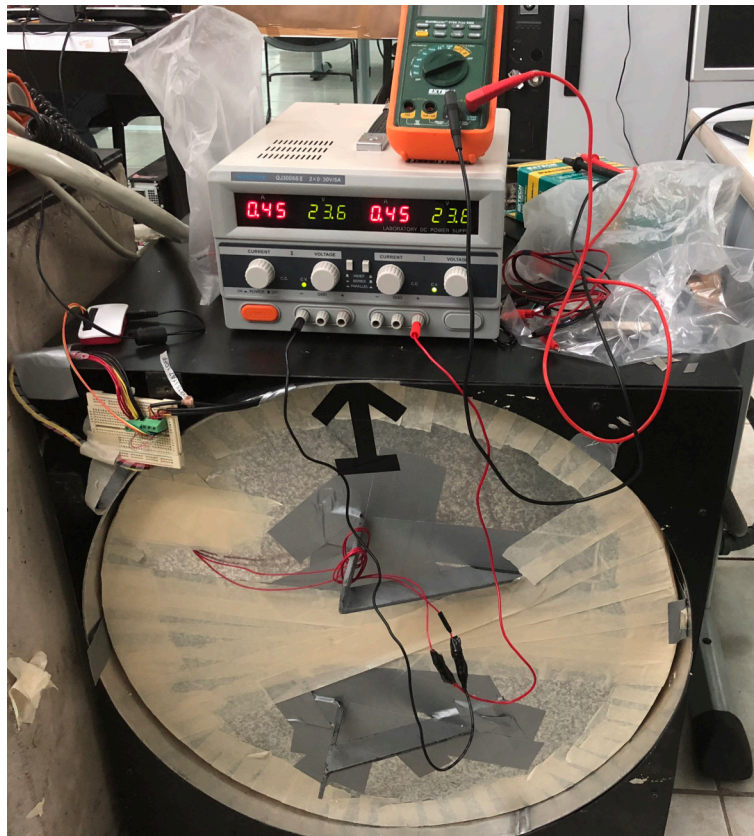


Figure 3.10. Diagram of the acquisition, preprocess and distribution data system.



(a) Calorimeter mounted and instrumented



(b) Calorimeter in operation

Figure 3.11. Final assembly of (a) the non-conventional calorimeter using (b) a mini-computer to read the temperature sensors.



### 3.3 Numerical simulation

#### 3.3.1 Mathematical model

Figure 3.12 shows the entire system (*i.e.*, the proposed non-conventional calorimeter device) prior described, and the symmetry-based reduced system, both studied in this work. The latter is defined as a slice of the entire system, which contains a half fin and half channel of the radial plate-fin structure at the main chamber.

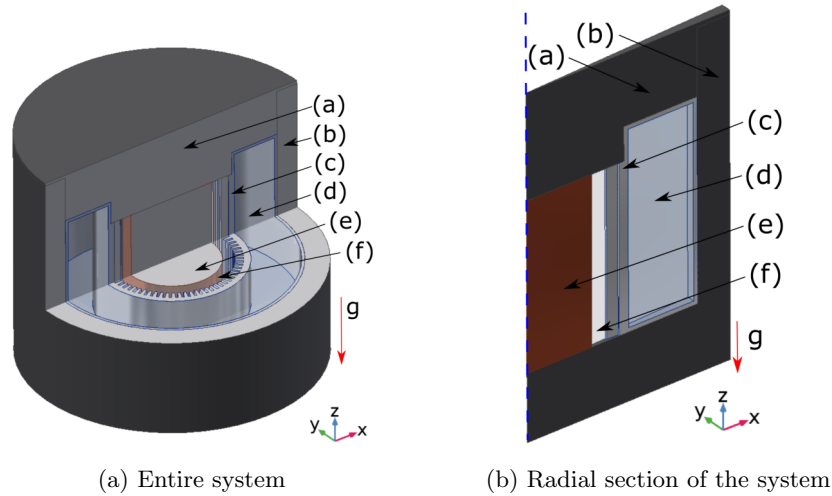


Figure 3.12. Computational domain of the studied system: a non-conventional calorimeter for electronic devices.

All subdomains of the system, in Figure 3.12, are described as follows:

- (a) *Insulation cover* allows locate the electronic device to be analysed in the main chamber and, also, serves as an insulation wall.
- (b) *Insulation coat* protects the process of any external thermal perturbation.
- (c) *Conductive core* is the thermal conductive metallic body, which is made by a radial plate-fin heat sink (the main chamber) and a fluid reservoir.
- (d) *Working fluid* exerts as a thermal energy storage body.
- (e) *Heat source* is the unknown electronic device under analysis inside the main chamber. In this work, it is assumed as a cylindrical body for illustrative purposes
- (f) *Air gap* is the space, filled with air from surroundings, between the electronic device and the main chamber.

In addition, Table 3.4 presents thermophysical properties of materials and fluids, linked to the above-mentioned subdomains, considered in this work. The material in last row of Table 3.4, copper, is used for nanoparticles in a complementary analysis of the system, that is by employing a water-based nanofluid.

On mathematical modelling of practical engineering systems, it is common to start analysing the process employing the mass conservation principle, also known as the continuity equation [162, 165]. In this work, the mass density ( $\rho$  [kg/m<sup>3</sup>]) for both fluids in the

Table 3.4: Thermophysical properties of materials used in this work.

Subdomain	Material	Property	Value
(a)–(b)	Polystyrene (PS)	$\rho$	28 kg/m <sup>3</sup>
		$k$	0.033 W/m·K
		$c$	1500 J/kg·K
(c)	Aluminium (Al)	$\rho$	2700 kg/m <sup>3</sup>
		$k$	238 W/m·K
		$c$	900 J/kg·K
(d)	Water (H <sub>2</sub> O)	$\rho$	998.2 kg/m <sup>3</sup>
		$k$	0.615 W/m·K
		$c$	4182.6 J/kg·K
		$\mu$	8.5×10 <sup>-4</sup> Pa·s
		$\beta$	2.75×10 <sup>-4</sup> 1/K
		$\gamma$	1
(e)	FR4	$\rho$	1900 kg/m <sup>3</sup>
		$k$	0.3 W/m·K
		$c$	1369 J/kg·K
(f)	Air	$\rho$	1.1839 kg/m <sup>3</sup>
		$k$	0.25 W/m·K
		$c$	1004 J/kg·K
		$\mu$	1.4×10 <sup>-5</sup> Pa·s
		$\beta$	3.355×10 <sup>-3</sup> 1/K
		$\gamma$	1.4
(d)	Copper (Cu)	$\rho$	8960 kg/m <sup>3</sup>
		$k$	400 W/m·K
		$c$	385 J/kg·K

system (*i.e.*, air and water) is assumed constant, hence,

$$\rho(\nabla \cdot \underline{u}) = 0, \quad (3.14)$$

which indicates that the mass inside the system remains invariant in both stationary and transient states. This expression is associated to the incompressible flow condition.

Following step consists on modelling the energetic interaction in the operating system, that is through the first law of thermodynamics [125, 163, 166, 167]. It is important to remember that heat transfer is the main physical phenomenon of the studied system. Other interactions like changes on the kinetic and potential energy are neglected. Thus, the energy balance per unit volume for all domains of the computational model (Figure 3.12.2) is presented as,

$$\frac{1}{\alpha} \frac{DT}{Dt} = \nabla^2 T - \frac{q_e}{k}, \quad (3.15)$$

with

$$\frac{DT}{Dt} = \frac{\partial T}{\partial t} + (\underline{u} \cdot \nabla)T, \quad (3.16)$$

where  $\alpha = k/\rho c$  [m<sup>2</sup>/s] is the thermal diffusivity; and  $c$  [J/kg·K] and  $k$  [W/m·K] are the constant values for heat capacity at constant pressure, and thermal conductivity, respectively. These local properties depend of the materials of each subdomain in the system. Moreover,  $DT/Dt$  [K/s] is the material derivative of the local temperature,  $T$  [K] and  $\underline{u}$  [m/s] is the



velocity field.  $q_e$  [W/m<sup>3</sup>] is the heat power flux generated by an electronic device inside the system. For the entire model  $q_e = P_e$ , and for the reduced model  $q_e = P_e/V_s$ . Since  $P_e$  [W] is the total heat power produced by the unknown device with volume  $V_t$  [m<sup>3</sup>]. This volume is sliced in  $N_s$  symmetrical volumes ( $V_s = V_t/N_s$  [m<sup>3</sup>]) for the reduced computational domain.

The first l.h.s. term of (3.15) represents the temperature changes of the system. Whilst, the r.h.s. terms refer to the heat transfer rate into the system due to the conduction mechanism (Fourier's law), and the energy generation rate inside the system. Also, it is important to notice that the process is analysed in steady state, when the first r.h.s. term of (3.16) equals zero. Further, the second one is only relevant for fluid subdomains, *i.e.*, the working fluid (d) and the air gap (f) in Figure 3.12.2.

Besides mass and energy conservation balances in (3.14) and (3.15), it is needed to describe the behaviour of fluids through their velocity fields. This associated physical problem is coupled with the heat transfer problem for an accurate description of the natural or free convection process. Hence, in this work any external source of motion for fluids is disregarded and only the gravitational effect is considered. The fluid mechanic problem is stated by using Navier–Stokes equations [167, 168], with the Boussinesq approximation and assuming Newtonian and laminar fluids, as,

$$\rho \left[ \frac{\partial \underline{u}}{\partial t} + (\underline{u} \cdot \nabla) \underline{u} \right] = -\nabla p + \mu \nabla^2 \underline{u} + \beta \underline{g}(T - T_0), \quad (3.17)$$

since  $\rho$  [kg/m<sup>3</sup>] is the mass density at the reference temperature  $T_0$  [K],  $p$  [Pa] is the pressure field,  $\beta$  [1/K] is the coefficient of thermal expansion,  $\mu$  [Pa·s] is the dynamic viscosity,  $\underline{g}$  [m/s<sup>2</sup>] is the local gravitational acceleration vector. The inertial forces in the l.h.s. term of (3.17) are balanced with the r.h.s. terms: pressure, viscous, and external forces, respectively. This latter term is also known as the buoyancy force due to the gravity.

Summarising, the mathematical model is defined by the equations (3.15)–(3.17), and their three unknown variables,  $T$ ,  $p$ , and  $\underline{u}$ . The required boundary conditions to solve these stationary and transient problems are presented as follows. Figure 3.13 displays boundary conditions for the reduced model such as: symmetry, isothermal, adiabatic, heat source, and slip conditions.

The first set of boundary conditions, which deals with the reduced model symmetry at its internal boundaries (Figure 3.13), is

$$\hat{n} \cdot \underline{q} = 0, \quad (3.18)$$

$$\hat{n} \cdot \underline{u} = 0, \quad (3.19)$$

where  $\hat{n}$  is the normal unit vector of an internal face. Similarly, the adiabatic conditions, akin to (3.18), are defined at the axial symmetric edge, and at the bottom boundary of the system (Figure 3.13). Latter is assumed perfectly insulated. The external faces of the system are established with the isothermal condition (Figure 3.13) as

$$T = T_a, \quad (3.20)$$

since  $T_a$  [K] is the ambient temperature. The conditions of the fluid subdomains at their external faces, or inner walls (Figure 3.13), are set as slip boundaries as,

$$\hat{n} \cdot \underline{u} = 0. \quad (3.21)$$

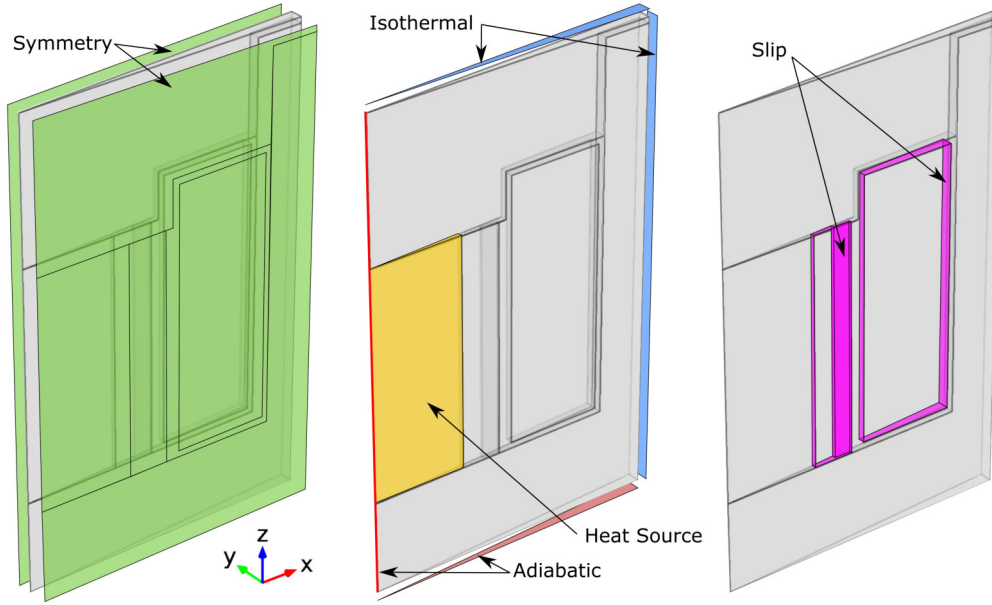


Figure 3.13. Boundary conditions of the computational domain: (left) symmetry, (centre) isothermal, adiabatic, heat source, and (right) slip conditions. Non-slip condition is assumed for solid boundaries.

No slip condition is assumed for solid boundaries. Moreover, the subdomain (e) from Figure 3.12.2 represents the heat source.

Lastly, initial conditions for the transient studies are defined as

$$T(t = 0) = T_a, \quad (3.22)$$

$$\underline{u}(t = 0) = \underline{0}, \quad (3.23)$$

$$p(t = 0) = p_0. \quad (3.24)$$

Additionally, sometimes the employed working fluid has a colloidal nature to enhance the overall heat transfer process. In that case, average values of thermophysical properties are determined by correlations from literature [107, 157, 169], such as

$$\rho_{nf} = \phi\rho_p + (1 - \phi)\rho_f, \quad (3.25)$$

$$\rho_{nf}c_{nf} = \phi\rho_p c_p + (1 - \phi)\rho_f c_f, \quad (3.26)$$

$$\rho_{nf}\beta_{nf} = \phi\rho_p\beta_p + (1 - \phi)\rho_f\beta_f, \quad (3.27)$$

$$\frac{k_{nf}}{k_f} = \frac{2k_f - 2\phi(k_f - k_p) + k_p}{2k_f + \phi(k_f - k_p) + k_p}, \quad (3.28)$$

$$\frac{\mu_{nf}}{\mu_f} = (1 - \phi)^{-2.5}. \quad (3.29)$$

where  $\phi$  [wt/wt%] is the volume nanoparticle concentration, and subscripts mean: base fluid ( $f$ ), nanoparticle ( $p$ ), and nanofluid ( $nf$ ). In this work, a water-based copper nanofluid (H<sub>2</sub>O–Cu) is regarded as an illustrative example for a complementary study.

### 3.3.2 Methodology

The mathematical problem stated above, for stationary and transient state, was solved numerically via the finite element method, with the computational domain mesh presented in Figure 3.14. This mesh was conformed for 26155 tetrahedral elements, 13017 triangular elements, 1027 edge elements, and 40 vertex elements. Numerical tasks were ran in a CPU with Dual Core AMD Opteron™ Processor 275, 3 out of 4 cores, using Linux as operating system. This supercomputer is hosted in the *Departamentul de Maşini, Materiale şi Acţionări Electrice, Facultatea de Inginerie Electrică* at the *Universitatea Politehnica din Bucureşti* (UPB), Romania, and administrated by Prof. Alexandru M. Morega.

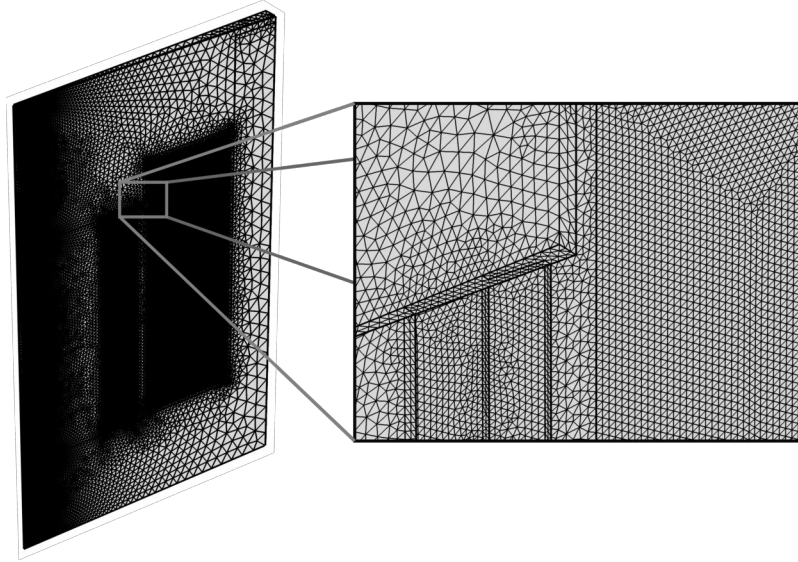


Figure 3.14. Implemented mesh of the reduced system.

All simulations were performed using assumed values for some parameters, which are displayed in Table 3.5. These studies corresponded to the reduced computational domain in Figure 3.12b. Then, for initial simulations associated to the *stationary study*,  $P_e$  was established equal to 0.1 W, and  $\phi$  equals 0 wt/wt% (only water as working fluid). Later, a parametric study was carried out varying the value of  $P_e$  in the range defined in Table 3.5. Similar parametric analyses were subsequently implemented assuming time dependency (the *transient study*). Specifically, four cases were adopted for these analyses as is specified in Table 3.6. On those cases, insulation means the kind of material employed for subdomains (a) and (b) from Figure 3.12, where practical means Polystyrene, and Fluid Motion column describes whether Navier–Stokes equations were considered in the simulation. Hereby, the most idealistic case consists on ideal insulation (adiabatic boundaries) and heat transfer process (disregarding fluid motion). Thereafter, the influence of employing the water–based copper nanofluid was explored for several values of  $\phi$ , Table 3.5.

### 3.3.3 Results and discussion

#### Stationary study

Figure 3.15 presents the velocity field of the air in the main chamber, and the water in the reservoir, under stationary conditions with  $P_e = 0.1$  W. It is noticed the well-known

Table 3.5: Assumed values for some parameters

Parameter	Value	Unit
$\underline{g}$	$(0, 0, -9.81)^\top$	$\text{m/s}^2$
$N_s$	140	–
$T_0, T_a$	298.15	K
$p_0$	101325	Pa
$P_e$	$[0, 0.1]$	W
$\phi$	$[0, 0.2]$	wt/wt

Table 3.6: Cases studied in time dependent analyses

Case	Insulation	Fluid Motion
1	Practical	Included
2	Practical	Disregarded
3	Ideal	Included
4	Ideal	Disregarded

convection cell due to the thermal power flux passing through the system. Moreover, this motion has a smaller scale at the reservoir filled with the working fluid in Figure 3.15.b—its maximum value is  $2.01 \times 10^{-3}$  m/s compared against 0.28 m/s from the air velocity field.

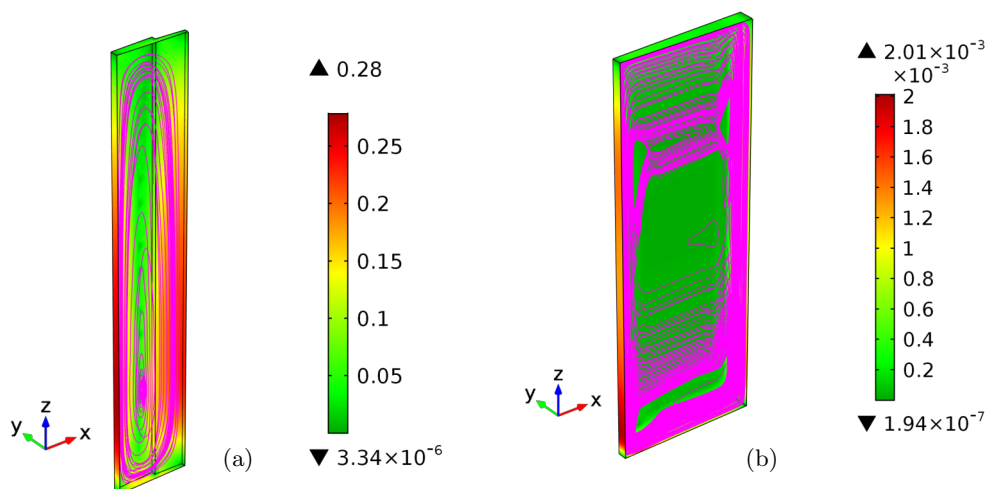


Figure 3.15. Velocity ( $\underline{u}$  [m/s]) fields of (a) the air in the main chamber, and (b) the working fluid in the reservoir, under stationary conditions with  $P_e = 0.1$  W.

Figure 3.16.a presents how the heat power ( $P_e$ ) is distributed per unit area, heat flux magnitude ( $q''$  [ $\text{W}/\text{m}^2$ ]), inside the system under stationary conditions. It is observed that this flux reaches the working fluid, as a thermal reservoir, as is expected in a calorimetry-based apparatus. Altogether, velocity and heat flux magnitude fields have a narrow relationship with a measurable quantity, *i.e.*, the temperature. Figure 3.16.b shows the temperature difference ( $\theta = T - T_0$ ) distribution of the reduced computational domain. It is observable an almost homogeneous  $\theta$  value approximately equals  $27^\circ\text{C}$  for the working fluid, unlike temperature values in the main chamber containing air. Temperature

difference distribution and isothermal surfaces in the reservoir are detailed in Figure 3.17.

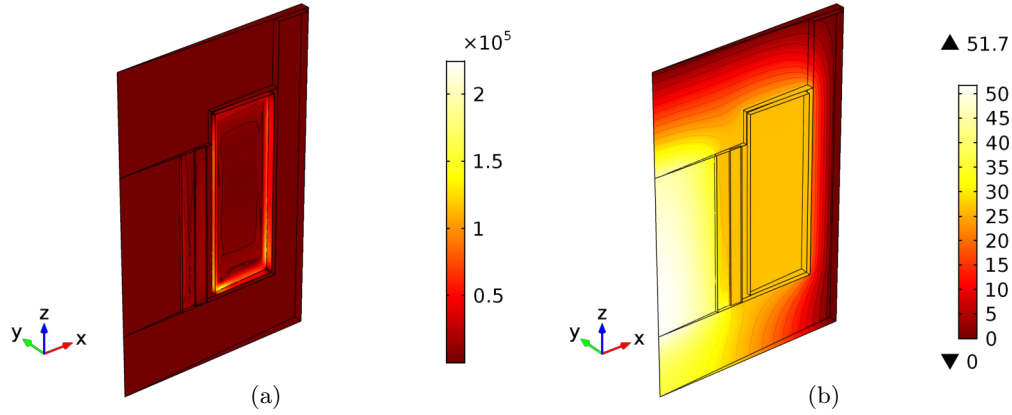


Figure 3.16. (a) Heat flux magnitude ( $q''$  [ $\text{W}/\text{m}^2$ ]) field, and (b) temperature difference ( $\theta = T - T_a$  [ $^{\circ}\text{C}$ ]) distributions in the system, under stationary conditions with  $P_e = 0.1$  W.

The described thermal behaviour in Figure 3.17 allows us realise its heterogeneous nature in the working fluid, with a temperature span of  $0.3$   $^{\circ}\text{C}$ . Hence, it is required find adequate locations of temperature sensors for the eventual implementation of the studied system. That is, in order to obtain accurate measurements and eventually determine the heat power, which an electronic device is generating. At first, the placement of those sensors is constrained to the external edge, at left-side in  $y$ -axis direction, of the working fluid inside the reservoir. Further, additional sensors could be located inside the main chamber to enhance the data acquisition process. Figure 3.18 shows the rescaled temperature difference ( $\tilde{\theta} \in [0, 1]$ ) distribution along the studied edge, for several values of total heat power ( $P_e$ ). Rescaling was performed in the data processing sense, *i.e.*,  $\tilde{\theta} = (\theta - \theta_{\min})/(\theta_{\max} - \theta_{\min})$ , and edge length extrema correspond to its vertices at bottom and top. It is easy to recognise that bottom vertex has the maximum temperature value, due to the gravity direction on the natural convection process. Besides, the top vertex reaches minimum temperature values when the total power increases. Moreover, it is noticed that temperatures along the edge tend the same distribution when the heat power is increased, but the bottom vertex maintains the maximum value of temperature.

A further analysis is displayed in Figure 3.19, which exhibits a comparison of temperature point values in the bottom vertices at the main chamber ( $\tilde{\theta}_{\text{MC,b}}$ ), and the reservoir ( $\tilde{\theta}_{\text{R,b}}$ ). These values were rescaled to  $[0, 1]$  employing average values for air ( $\langle \tilde{\theta} \rangle_{\text{air}}$ ), and water ( $\langle \tilde{\theta} \rangle_{\text{water}}$ ) as extrema. Latter corresponds to the vertex analysed in Figure 3.18. These values spread when the total power is increased, with average temperatures of air and water as maximum and minimum, respectively. Reservoir information has a lower dispersion than the ones of the main chamber, which says us that measuring the temperature at the edge bottom vertex is a good approach to the average value. More details are shown in Table 3.7. It is imperative to remark that if  $\theta_{\text{R,b}}$  values exceed the boiling point of water at atmospheric pressure, say  $P_e > 0.1$  W, results would be erroneous because the water phase change process has been disregarded in this work. Nonetheless, a calorimetric analysis is specified as a finite time process, thus, it is expected to get a good-enough estimation before it reaches those temperatures.

Now, it is easy to use the data from Table 3.7 to calculate the slope of each curve

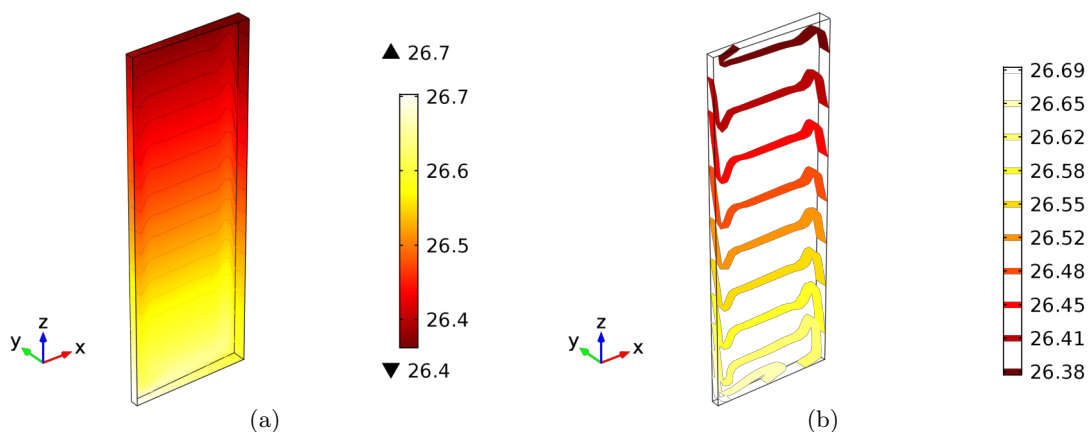


Figure 3.17. (a) Temperature difference ( $\theta = T - T_a$  [°C]) distribution, and (b) isothermal surfaces ( $\theta$  [°C]) of the working fluid in the reservoir, under stationary conditions with  $P_e = 0.1$  W.

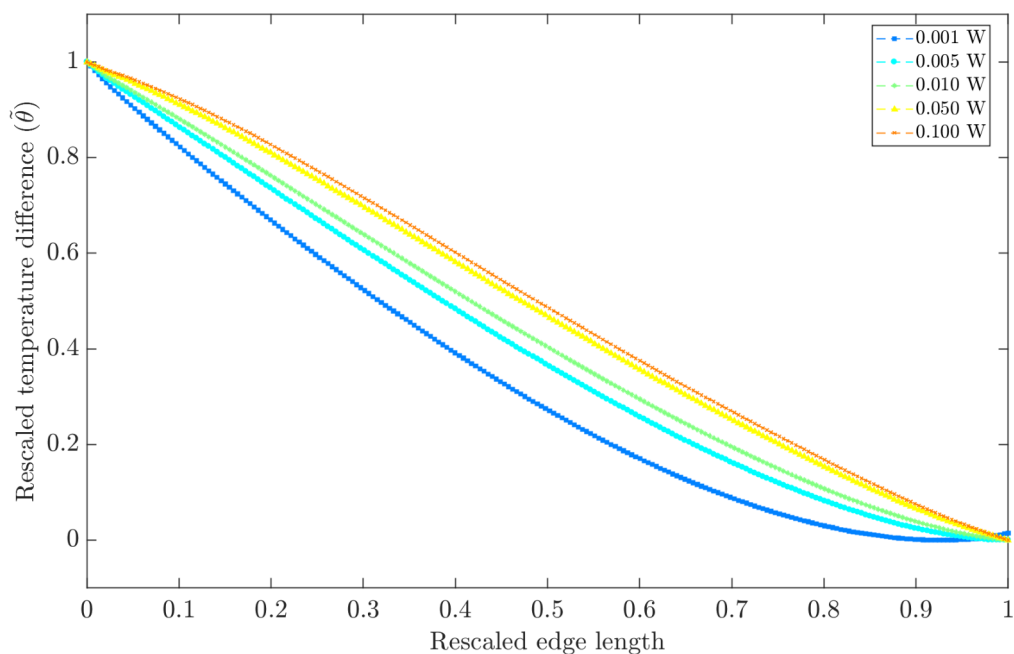


Figure 3.18. Rescaled difference temperature ( $\tilde{\theta} \in [0, 1]$ ) distribution along the studied edge of the working fluid, varying the total heat power ( $P_e$  [W]), and under stationary conditions.

from Figure 3.19, *i.e.*, the thermal resistance model in (3.8). Thus, Table 3.8 contains the obtained  $R$  values determined between different points of the system for the same stationary conditions. The value of  $R$  [K/W] is a numerical approach to the equivalent thermal resistance of the entire system under stationary condition. It represents a first approximation to the real process, which can be eventually employed to obtain the thermal power generated by an electronic device, using the measured temperature in a working fluid.

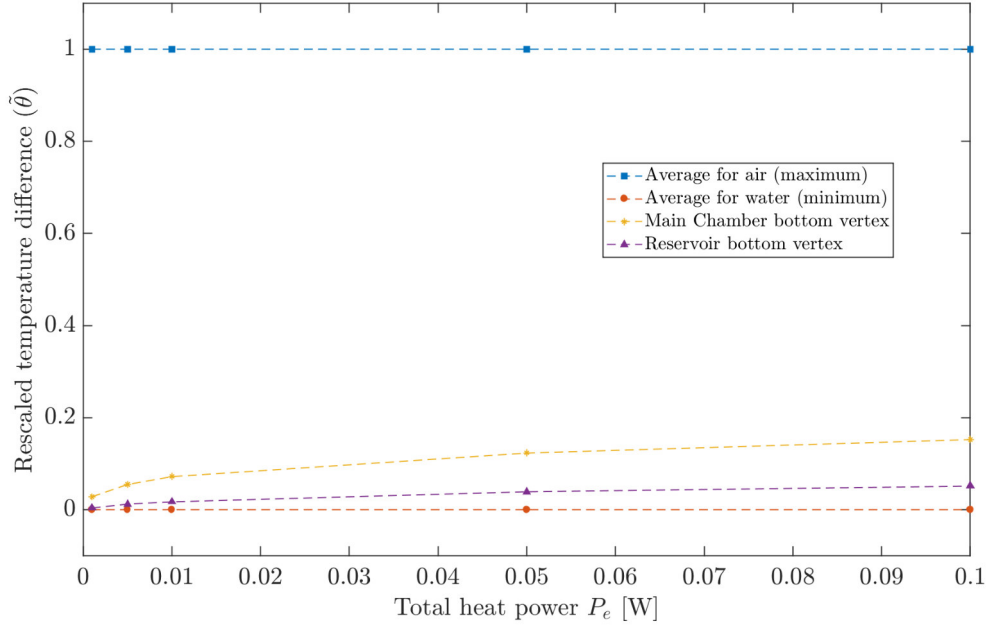


Figure 3.19. Rescaled temperature difference ( $\tilde{\theta} \in [0, 1]$ ) values at different locations in the working fluid, amongst air and water average values, by varying the total heat power ( $P_e$  [W]), and under stationary conditions.

Table 3.7: Temperature difference values of several measurements for different values of total heat power ( $P_e$ ). These are average values for air ( $\langle \theta \rangle_{\text{air}}$ ), and water ( $\langle \theta \rangle_{\text{water}}$ ); and point values in the bottom vertices at the main chamber ( $\theta_{\text{MC,b}}$ ), and the reservoir ( $\theta_{\text{R,b}}$ ).

$P_e$ [W]	$\langle \theta \rangle_{\text{air}}$ [ $^{\circ}\text{C}$ ]	$\langle \theta \rangle_{\text{water}}$ [ $^{\circ}\text{C}$ ]	$\theta_{\text{MC,b}}$ [ $^{\circ}\text{C}$ ]	$\theta_{\text{R,b}}$ [ $^{\circ}\text{C}$ ]
0.001	0.3756	0.2643	0.2675	0.2647
0.005	1.6128	1.3107	1.3273	1.3142
0.010	3.0814	2.6312	2.6638	2.6391
0.050	14.3030	13.1095	13.2570	13.1556
0.100	28.3445	26.5027	26.7839	26.5983

Table 3.8: Equivalent thermal resistance ( $R$  [K/W]) values determined between different points of the system under stationary conditions.

Location	$\theta$ [ $^{\circ}\text{C}$ ]	$R$ [K/W]
Air in the Main Chamber	$\langle \theta \rangle_{\text{air}}$	281.7559
Main Chamber bottom vertex	$\theta_{\text{MC,b}}$	267.6173
Water in the Reservoir	$\langle \theta \rangle_{\text{water}}$	264.8150
Reservoir bottom vertex	$\theta_{\text{R,b}}$	265.7795

### Transient study

For the first case from Table 3.6, Figure 3.20 shows the temperature difference,  $\theta(t)$  [ $^{\circ}\text{C}$ ], behaviour for several values of heat power,  $P_e$ . This temperature corresponds to the mea-

sured one at the bottom vertex of the working fluid. Subsequently, results from case 2 are presented in Figure 3.21. Both two first cases are achieved by utilising a real material (Polystyrene) as insulation. Their main difference lays on whether the influence of fluid motion in the heat transfer process is considered; *i.e.*, case 1 is a multiphysics problem and case 2 is a purely heat transfer problem. That assumption was made because the maximum value of  $\underline{u}$  equals  $2.01 \times 10^{-3}$  m/s at  $P_e = 0.1$  W, for the working fluid in the stationary state analysis (Figure 3.15), which could be assumed as a *motionless* process for practical purposes. For both cases, the temperature variation is almost similar as is observed in Figure 3.22. Those differences increase with the heat power (Figure 3.22), due to the fluid motion is strengthened (case 1), which enhances the heat transfer through the system. Hence, it is noticed that the system could be simplified as motionless for lower power losses.

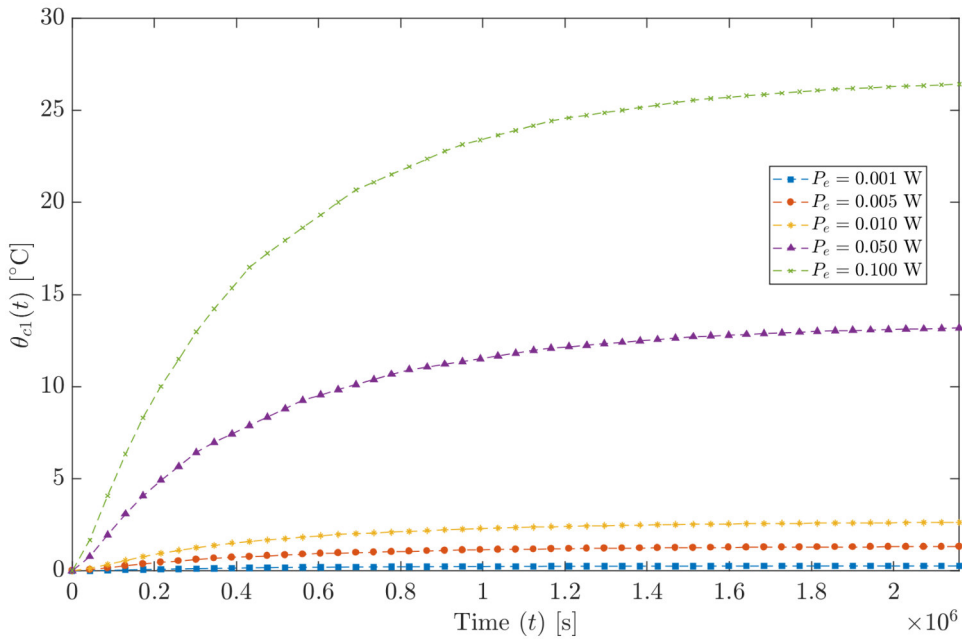


Figure 3.20. Temperatures difference ( $\theta_{c1}(t)$  [°C]) values at the bottom vertex in the working fluid, varying the total heat power ( $P_e$  [W]), and under time dependent conditions. Case 1: A multiphysics problem with an insulation material.

Temperature variation for cases 3 and 4, which regard with ideal insulation boundaries, are showed in Figures 3.23 and 3.24, respectively. Similarly to the others cases, Figure 3.25 displays the differences between these two cases, whose have an ideal insulation. Also, it is notorious a gain augment related to the heat power whose can be determined in a tuning process, or avoided in a dimensionless analysis. In both cases, it is recognised the ideal insulation gave place to unstable responses, which eventually are going to destroy the system in practise. However, for practical experiments with a delimited time, insulate the system as much as possible might be guarantee of accurate and faster results. Besides, when the insulation is poor, *i.e.* there exists a relatively great amount of leaking heat power, the determination process fails.

Following the idea of a finite experimental test, and performing additional simulations for more values of  $P_e$ , Figure 3.26 was obtained. On that, temperatures rise faster when



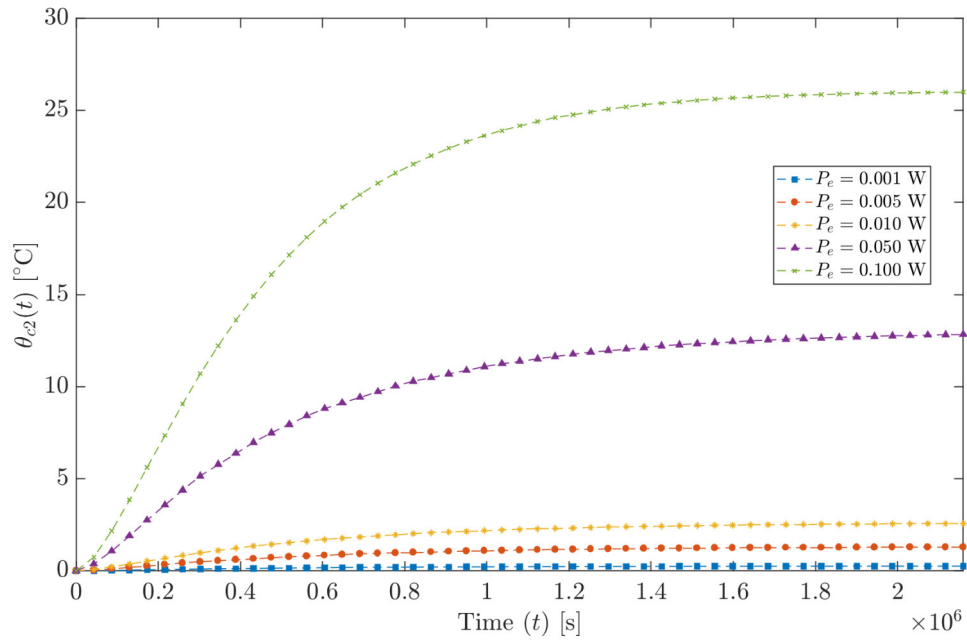


Figure 3.21. Temperatures difference ( $\theta_{c2}(t)$  [ $^{\circ}\text{C}$ ]) values at the bottom vertex in the working fluid, varying the total heat power ( $P_e$  [W]), and under time dependent conditions. Case 2: A heat transfer problem with an insulation material.

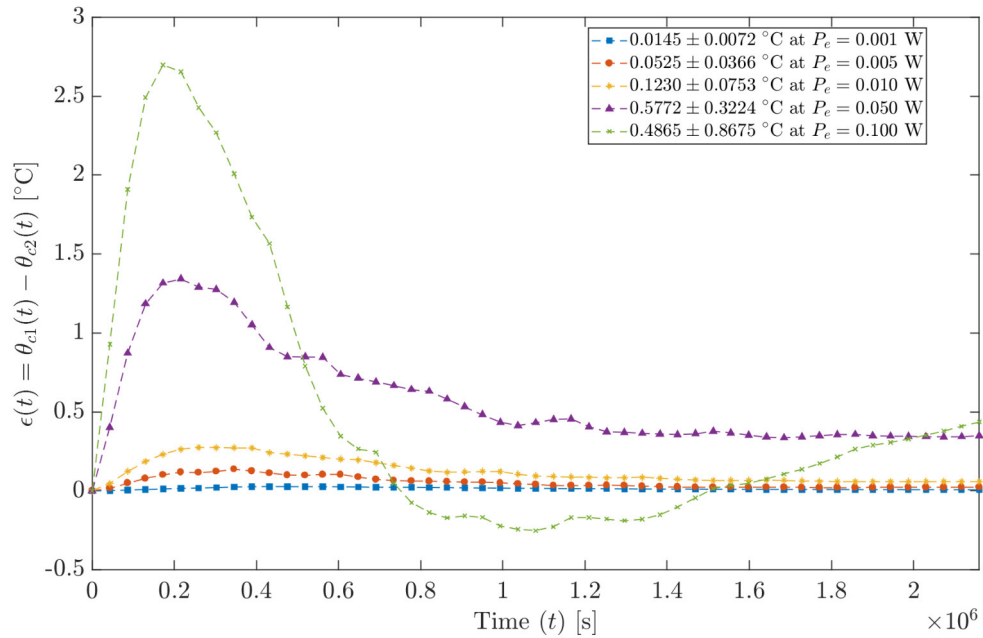


Figure 3.22. Difference between temperatures values at the bottom vertex in the working fluid ( $\epsilon = \theta_{c1} - \theta_{c2}$ ), from Case 1 ( $\theta_{c1}$ ) and Case 2 ( $\theta_{c2}$ ), varying the total heat power ( $P_e$  [W]).

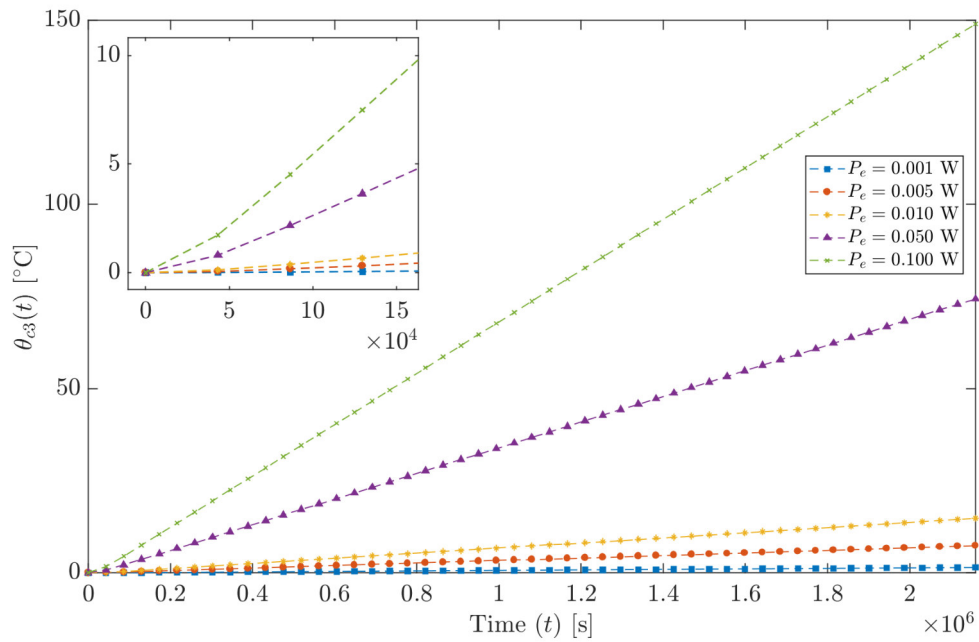


Figure 3.23. Temperatures difference ( $\theta_{c3}(t)$  [°C]) values at the bottom vertex in the working fluid, varying the total heat power ( $P_e$  [W]), and under time dependent conditions. Case 3: A multiphysics problem assuming ideal insulation.

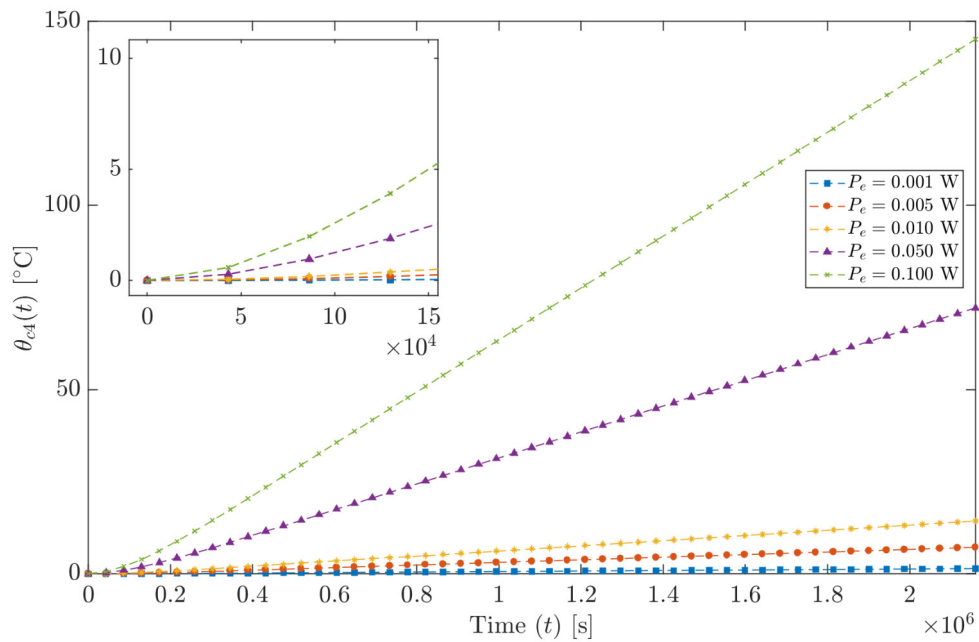


Figure 3.24. Temperatures difference ( $\theta_{c4}(t)$  [°C]) values at the bottom vertex in the working fluid, varying the total heat power ( $P_e$  [W]), and under time dependent conditions. Case 4: A heat transfer problem assuming ideal insulation.

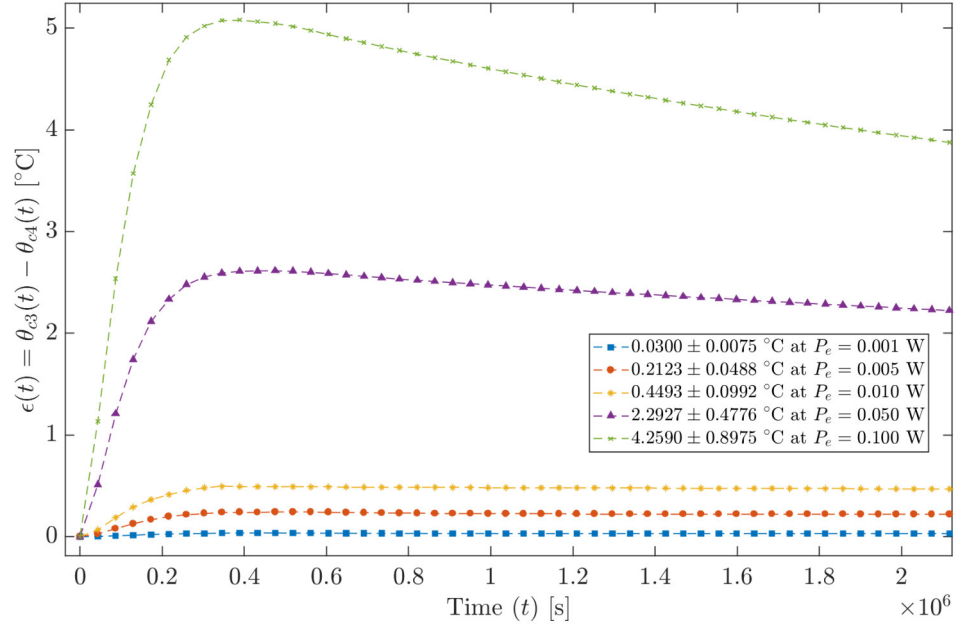


Figure 3.25. Difference between temperatures values at the bottom vertex in the working fluid ( $\epsilon = \theta_{c3} - \theta_{c4}$ ), from Case 3 ( $\theta_{c3}$ ) and Case 4 ( $\theta_{c4}$ ), varying the total heat power ( $P_e$  [W]).

the heat power is greater, but slow enough to measure them before the system blow-up. Therefore, the power generated by an electronic device can be found from (3.13), using the thermophysical properties of the fluid, as is plotted in Figure 3.27. These results are approximations with errors dependent of  $P_e$ , which can be tuned finding an off-set level in a practical implementation. Also, the determination can be enhanced by using a system identification process whilst measurements are acquired, by taking advantage of its well-known exponential form.

In addition, the influence of using a water-based copper nanofluid was explored as a mechanism to enhance the heat transfer process in the calorimetric system. For this analysis,  $P_e$  was defined equals 0.1 W, and several values of the nanoparticles volume concentration  $\phi$  [wt/wt%], amongst 0 and 20%, were employed. Difference temperature variations are showed in Figure 3.28. There is observed a slightly increment in the temperature value related with  $\phi$ , as it was expected. Nevertheless, this enhancement is only perceived in the magnitude of  $\theta$ . Also, Figure 3.29 displays the determined values of the heat power, where the best results correspond to the initial fluid, water without nanoparticles. This could be due the slow motion of the working fluid, and the average heat capacity tends to the solid material. It is important to continue researching in this kind of implementation by including external electromagnetic fields to enhance thermal process.

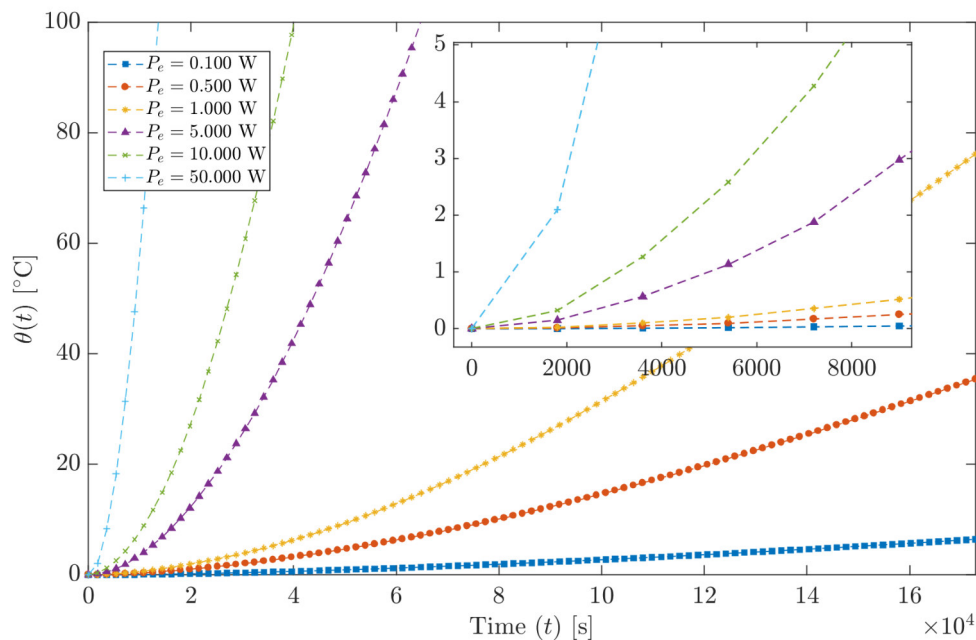


Figure 3.26. Temperatures difference ( $\theta_{c4}(t)$  [°C]) values at the bottom vertex in the working fluid, varying the total heat power ( $P_e$  [W]), and under time dependent conditions. Case 4 with more values for  $P_e$  and a shorter elapsed time.

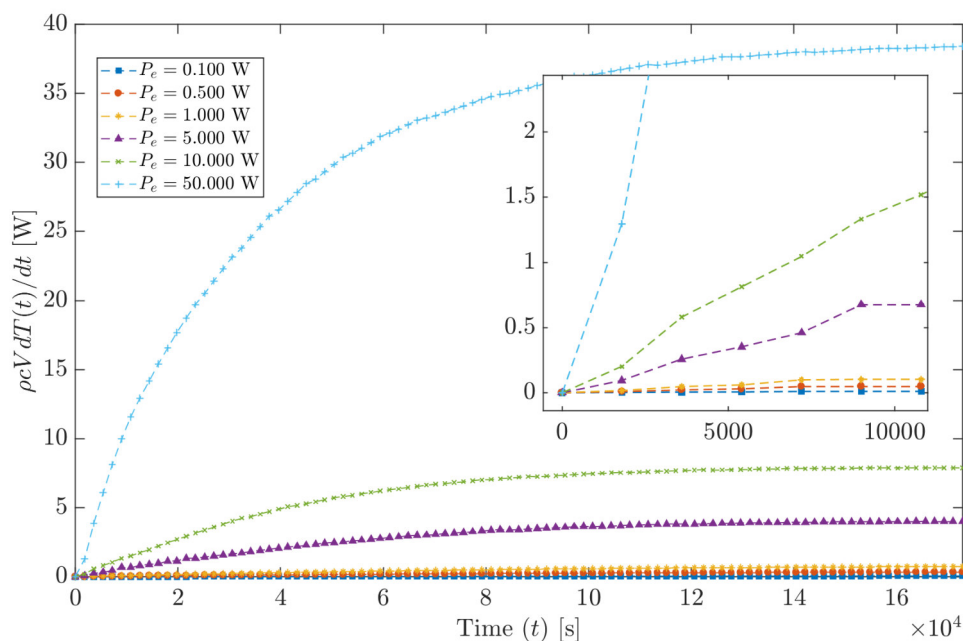


Figure 3.27. Determined heat power ( $\dot{Q} = \rho c V dT(t)/dt$  [W]) from temperature values at the bottom vertex in the working fluid, varying the total heat power ( $P_e$  [W]), disregarding Navier–Stokes equations, assuming ideal insulation boundary conditions, and under time dependent conditions.

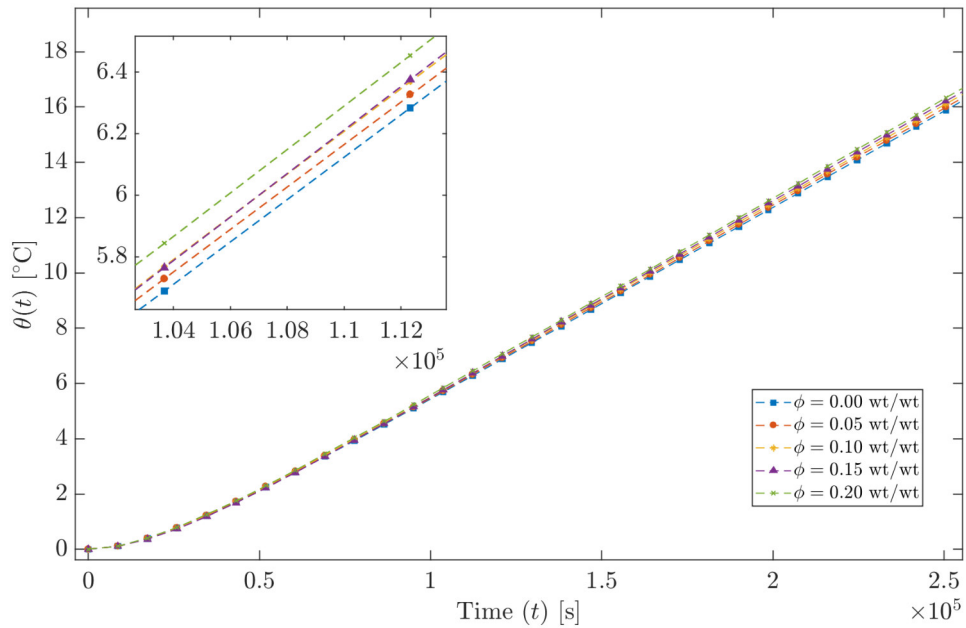


Figure 3.28. Temperatures difference ( $\theta_{c4}(t)$  [ $^{\circ}\text{C}$ ]) values at the bottom vertex in the working fluid, varying the nanoparticles volume concentration ( $\phi$  [wt/wt%]), at  $P_e = 0.1$  W, considering a multiphysics problem, assuming ideal insulation boundary conditions, and under time dependent conditions.

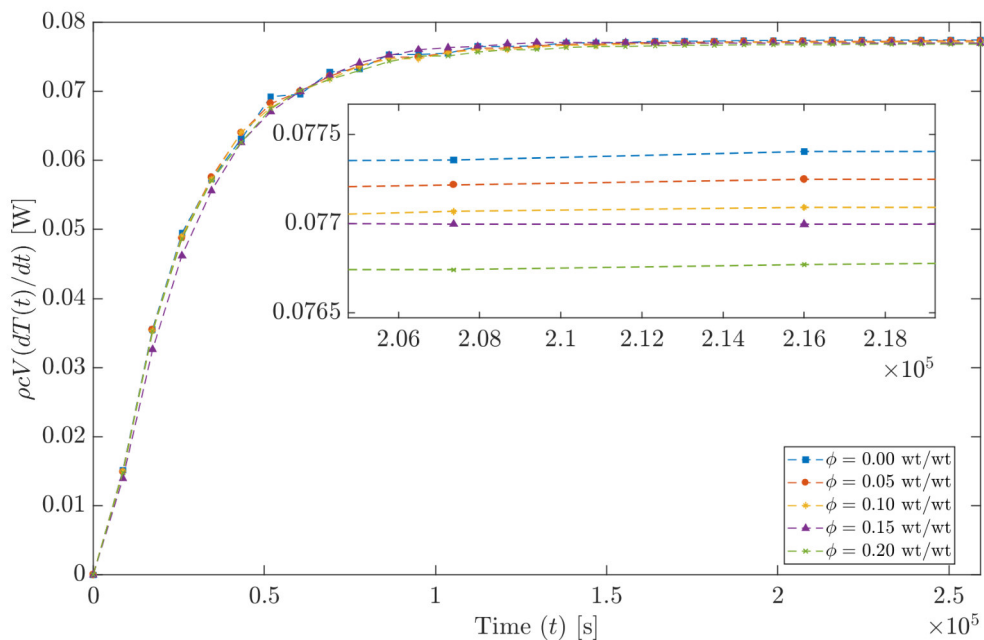


Figure 3.29. Determined heat power ( $\dot{Q} = \rho c V dT(t)/dt$  [W]) from temperature values at the bottom vertex in the working fluid, varying the nanoparticles volume concentration ( $\phi$  [wt/wt%]), at  $P_e = 0.1$  W, considering a multiphysics problem, assuming ideal insulation and under time dependent conditions.

## 3.4 Experimental implementation

### 3.4.1 Methodology

The experimental implementations were performed in two stages, such as Characterisation and Calibration. It was required well-known power dissipation values for these stages. Thus, an electrical resistance of  $100 \Omega \pm 10\%$ , 25 W max, and a Laboratory DC Power Supply, Nov@tek<sup>TM</sup> QJ3005SII,  $2 \times 0\text{-}30\text{V}/5\text{A}$ , were employed. Table 3.9 shows the power's values defined to carry out the experiments, as well as voltage's and resistance's ones, plus their real values measured after the practical implementation.

Table 3.9: Power values set-up for both characterisation and calibration procedures, using an electrical resistance of  $100 \Omega \pm 10\%$ .

Theoretical			Practical		
$P$ [W]	$V$ [V]	$R$ [ $\Omega$ ]	$P$ [W]	$V$ [V]	$R$ [ $\Omega$ ]
1.0	10.000	100	<b>1.00</b>	10.01	100.11
5.0	22.361	100	<b>4.91</b>	22.34	101.55
10.0	31.623	100	<b>9.80</b>	31.61	101.97
15.0	38.730	100	<b>14.72</b>	38.73	101.92
20.0	44.721	100	<b>19.24</b>	44.75	104.80

For the calorimeter characterisation, implementations with known powers from Table 3.9 were used, and the corresponding measurements were acquired during at least 40 h and about 5 min of sampling time. In this work, the air temperature is recorded to monitor the electronic device's environment, to avoid jeopardising it during the tests, and to clip the test's times. The principal interest resides in determining the water's temperatures' changes. Once raw data is obtained, these are preprocessed, averaged and fitted to a known model. Whereas, this behaviour for the water's average temperature inside the calorimeter is modelled in (3.3) and corroborated with Figures 3.20 and 3.21 (from the numerical simulation study). The expression for the temperatures' difference  $\theta(t)$  has the well-known form given in (3.4), which is rewritten with an offset parameter added for fitting purposes, as follows,

$$\hat{\theta}(t) = \theta_{\infty} \left(1 - e^{-t/\tau}\right) - \vartheta, \quad (3.30)$$

since  $\hat{\theta}(t)$  [K] means the temperature variation's functional with  $\theta_{\infty}$  [K],  $\tau$  [s], and  $\vartheta$  [K] as real-positive valued unknown parameters. Further, these parameters are correlated with the material's thermophysical properties and geometries conforming the system (the water body) and the energy entering on it, such as  $\tau = RC$  and  $\theta_{\infty} = \dot{Q}R$ . As it was mentioned in Section 3.1,  $R$  [K/W] is the thermal resistance,  $C$  [J/K] is the heat capacity and  $\dot{Q}$  [W] is the thermal power. Thereto, data adjustment were conducted through a non-linear regression process, solving the associated Non-linear Least Squares (NLS) problem (cf. Section 2.1.3). The minimisation procedure was carried out in two stages via an hybrid initialise-and-refine strategy forged with Stochastic Spiral Optimisation Algorithm (SSOA) and, the traditional Levenberg–Marquardt algorithm (LMA). SSOA was proposed as an enhanced version of DSOA, described in the previous Chapter, and more information about it can be found in [153].

Consequently, the calibration stage aimed at defining a strategy for determining the power dissipated by a microelectronic device using, certainly, the characterisation stage's

inferences. To perform that, the Ordinary Least Squares (OLS) problem was considered [170],

$$\hat{\underline{\beta}}^* = \arg \min_{\underline{\hat{\beta}}} \left\{ \|\underline{Y} - \underline{X}\hat{\underline{\beta}}\|^2 \right\}, \quad (3.31)$$

which has a well-known solution given by,

$$\hat{\underline{\beta}}^* = (\underline{X}^T \underline{X})^{-1} \underline{X}^T \underline{Y}, \quad (3.32)$$

since  $\hat{\underline{\beta}} = (\hat{\beta}_0, \hat{\beta}_1)^T$  is the coefficients' vector from the linear expression  $\hat{y}(x) = \hat{\beta}_0 x + \hat{\beta}_1$ ;  $\underline{Y} = \langle \theta \rangle$  are the temperature's measurements,  $\underline{X} = (\underline{t}, \underline{1})$  is a matrix with the time series and a vector of elements equal one, both two concatenated as its first and second columns; and  $\|\cdot\|^2$  is the squared 2-norm. Two manners for determining the heat power were explored, both of them based on the foundations described in Section 3.1 and using (3.32). First is based on obtaining the initial slope for the temperature behaviour according to (3.7), then the heat power is achieved by multiplying that slope with the heat capacity, such as (3.6). Second approach is inspired on the differential equation's solution at (3.4) utilising the experimental values of  $R$  and  $C$  to find  $\tau$  and, transforming the exponential equation to a linear one, with a dummy time series given by  $\tilde{t} = (1 - e^{-t/RC})$ . Likewise, the obtained slope is divided into  $R$  to calculate the heat power. Moreover, the goodness of these simple linear regressions are assessed via the coefficient of determination, or  $R$  squared quantity ( $R^2$ ), defined in [170] as,

$$R^2 = 1 - \frac{\|\underline{Y} - \hat{\underline{Y}}\|^2}{\|\underline{Y} - \langle \underline{Y} \rangle\|^2}, \quad (3.33)$$

since  $\hat{\underline{Y}}$  is the fitted data and  $\langle \underline{Y} \rangle$  is the average value of  $\underline{Y}$ .

### 3.4.2 Results and discussion

Figure 3.30 presents the data acquired during for both six sensors, three inside the *Main Chamber* (filled with air) and three immersed in the *Tank* (filled with water), for tests with 4.91, 9.8 and 14.72 W as illustrative examples. These curves are more like staircase signals when the energy rate is reduced, as it is expected due to the slow changes of temperatures. Besides, it is noticeable that the sheathed sensors (into the *Tank*) register less-varied temperatures when power increases. Hence, the main aim is to read the temperature's changes of the working fluid as is shown in Figure 3.31. This plot summarises the conducted tests as follows: the average measurements and their variations are presented as shaded strips, and the data adjusted as solid lines. It is important to notice that it is a lack of information amongst 20 h and 75 h for measurements of 14.72 W, because a quick power interruption occurred in the laboratory. Immediately the energy returned, the DC Power Supply started duties but somehow, the microcomputer (acquisition system) was unable to start the measurement's daemon.

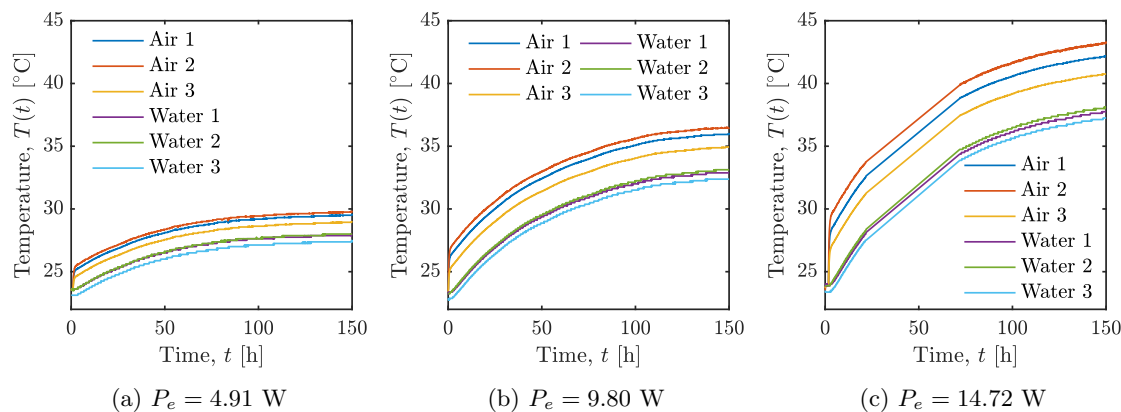


Figure 3.30. Results from three long time (at least 150 h) experiments: temperatures registered by sensors into the *Main Chamber* and *Tank*.

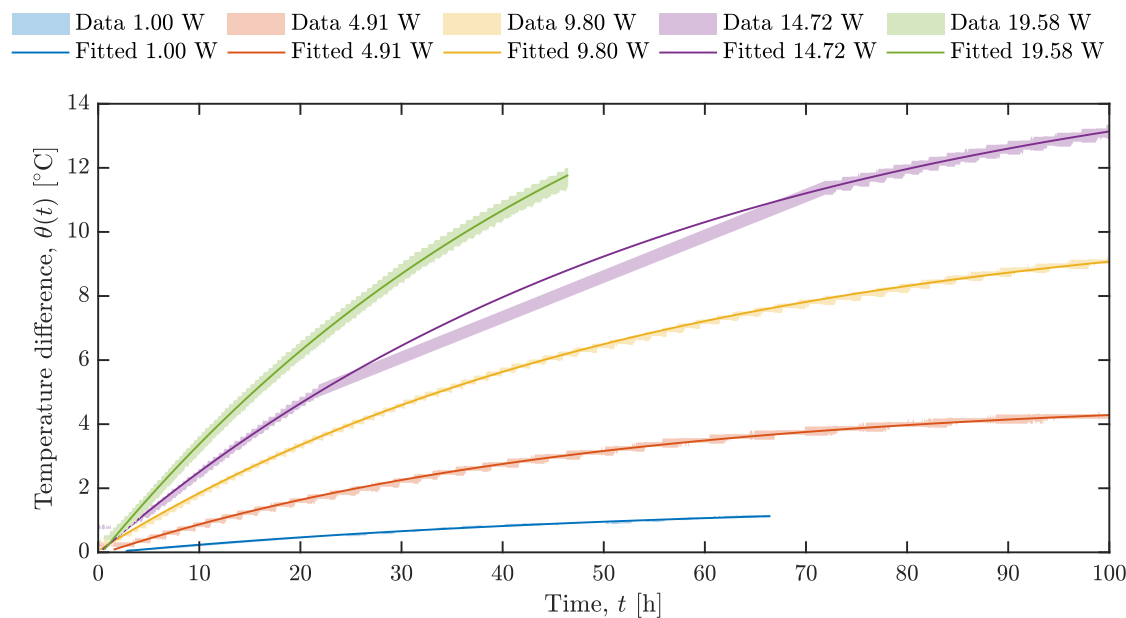


Figure 3.31. Fitted curves for the water's average measurements per experiment

Table 3.10 presents the results obtained from the data fitting procedure, and their adjustment's goodness given by the coefficient of determination ( $R^2$ ). In a glance, it is notorious that  $\theta_\infty$  is close to  $P_e$  in magnitude, which means  $R$  is near unity. However, it is known that the relationship between theoretical power and thermal resistance is indirect, because heat dissipated by the device under analysis (DUA) has to pass through several media, and heat power losses are inevitable but reduced due to the calorimeter's insulation. Heat power entering the water is defined as  $\dot{Q}$  [W] for practical purposes though, and its liaison with  $P_e$  is directly proportional. Likewise, the value of  $R$  is determined by using the time constant ( $\tau$  [s]) and the prior knowledge of the thermal capacity ( $C$  [J/K]) via  $R = \tau/C$ . This value is obtained from the average information of water's volume ( $V$  [m<sup>3</sup>]) and thermophysical properties (*i.e.*,  $\rho$  [kg/m<sup>3</sup>] and  $c$  [J/kg·K]) in Tables 3.1 and



3.4, respectively; which gives place to  $C = \rho cV = 167.94$  kJ/K. The bias parameter  $\vartheta$  serves as numerical time corrector.

Table 3.10: Results from the fitting procedure performed using the data obtained in the characterisation stage and the model in (3.30).

$P_e$ [W]	$R^2$	$\theta_\infty$ [K]	$\tau$ [h]	$\vartheta$ [K]
1.00	0.9943	1.6130	58.1670	0.0210
4.91	0.9992	4.8365	48.6562	0.2006
9.80	0.9997	10.7478	54.6816	0.2798
14.72	0.9999	15.3503	58.2080	0.2049
19.24	0.9998	20.0459	52.8541	0.4193

Figure 3.32 displays the calorimeter's characteristics found using the above described analysis. Thermal resistance values are presented in Figure 3.32a, where it is notorious an average value  $\langle R \rangle$  equals 1.17 K/W with small variations due  $P_e$ . Consequently, the thermal power entering the *Tank* is calculated as Figure 3.32b exhibits. A linear trend is observed, where the slope of 0.87 W/W is the total power's portion reaching the water.

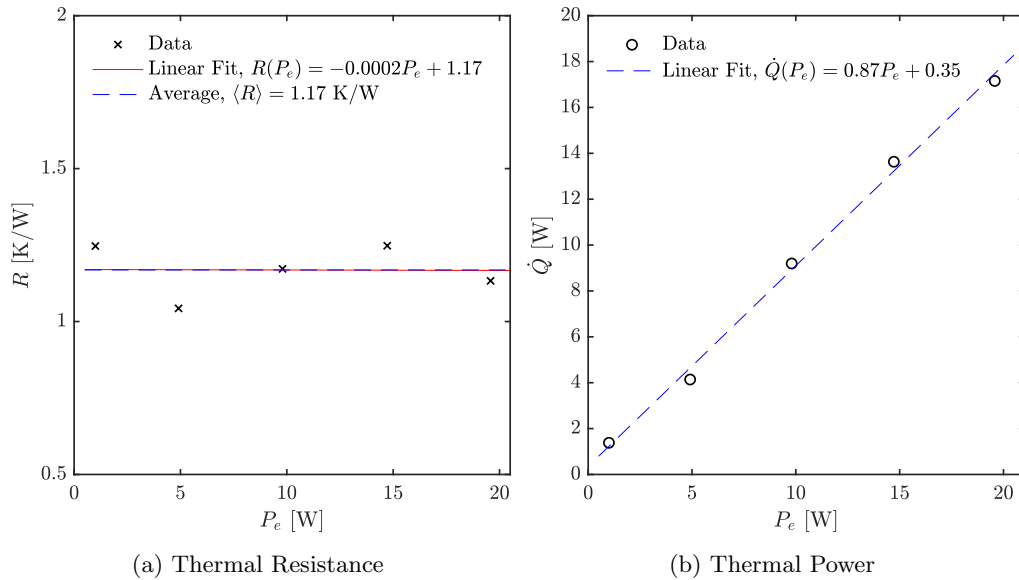


Figure 3.32. Calorimeter's characteristics determined from measurements.

Afterwards, the linear and exponential approaches to solve the OLS problem (3.32) were employed with the experimental data from tests carried out according to Table 3.9. Figures 3.33d to 3.33e display the determined heat power evolution using both approaches, in a time window of 50 h. In all cases a maximum value is observed in the linear approach, as expected, due the first slope of this exponential behaviour (cf. (3.4)) is the greatest; more importantly, it represents the obtained heat power. Despite the fact that it appeared some time later because the amount of sensed temperatures was insufficient. This feature reveals a manner to reduce the measurement time without compromising its quality, remembering that the determination performed in the characterisation stage required of at least 50 h, almost a time equals the calorimeter's time constant. Now, it is evident that

the exponential approach tends to a stable value whilst more data is considered. It is mainly due this approach is an amplitude adjustment for a known shape given by the time constant previously found. Final determination is enhanced when more data is considered. Summarising, the linear approach is fast but obtains acceptable results; conversely, the exponential approach achieves good-enough results but is slow. Then, it is possible to combine the both approaches to take advantage of their key features, *i.e.*, to use the linear approach as a stopping criterion, and the exponential as a determination criterion. When the thermal power is achieved, it is required an adjustment. Figure 3.33f presents the relationship between the obtained heat power  $\dot{Q}$  exciting the water and the power dissipated by the analysed device. Withal, Table 3.11 details the power's determinations and their elapsed times, those decrease when  $P_e$  is increased. It is straightforward to observe the linear tendency betwixt  $P_e$  and  $\dot{Q}$ , which corroborates the information visualised in Figure 3.33f.

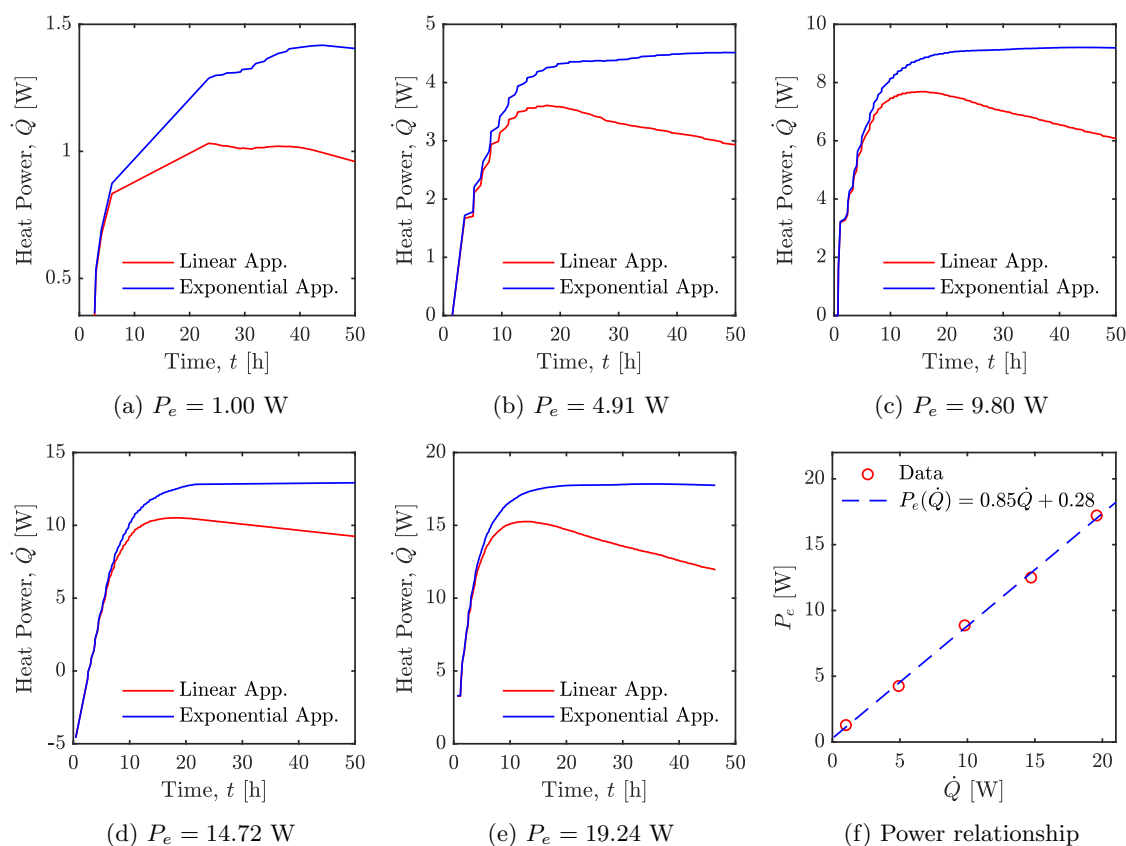


Figure 3.33. Determination of the heat power using two iterative approaches and varying the power source's value.

Taking advantage of above mentioned, a time-reduced measurement procedure can be implemented. Then, a resulting strategy for measuring the power dissipation, using the non-conventional calorimeter, is outlined in Pseudocode 5. These steps were coded and implemented for monitoring the sensing procedures in real-time.

Table 3.11: Determined heat power from several experiments varying the power source.

Theoretical power $P_e$ [W]	Experimental power $\dot{Q}$ [W]	Elapsed time $t_e$ [h]	Power's difference $\dot{Q}/P_e$ [W/W]
1.00	1.2878	23.47	1.2878
4.91	4.2553	17.65	0.8667
9.80	8.8658	16.04	0.9047
14.33	12.5007	18.16	0.8492
19.58	17.2162	12.56	0.8793

---

**Pseudocode 5.** Strategy for determining the power dissipated by a microelectronic device.

---

**Input:** Ambient temperature ( $T_a$  [°C]), Heat capacity ( $C$  [J/K]) and Thermal resistance ( $R$  [K/W]). Adjustment's function ( $P_e = f(\dot{Q})$ ).

- 1: Consider the liner model:  $\hat{y}(x) = \hat{\beta}_0 x + \hat{\beta}_1$ .
  - 2: **repeat**
  - 3:   Read the current temperatures and their times ( $\langle \theta \rangle, \underline{t}$ ) for each sensor.
  - 4:   Obtain  $\langle \theta \rangle$  by preprocessing and averaging the temperatures.
  - 5:   Find  $\hat{\theta}_1$  by OLS, with  $\langle \theta \rangle$  and  $\underline{t}$ , and obtain  $R^2$ . ▷ Linear Approach
  - 6:   Calculate  $\dot{Q}_1 = C\hat{\beta}_0$ , employing  $\hat{\beta}_0$  from the previous step.
  - 7:   Determine  $\tilde{t} = (1 - e^{-t/RC})$  as a dummy time series.
  - 8:   Find  $\hat{\theta}_2$  by OLS, with  $\langle \theta \rangle$  and  $\tilde{t}$ , and obtain  $R^2$ . ▷ Exponential Approach
  - 9:   Calculate  $\dot{Q}_2 = \hat{\beta}_0/R$ , employing  $\hat{\beta}_0$  from the previous step.
  - 10:   Obtain  $P_e$  with  $\dot{Q}_2$ .
  - 11:   Print relevant results and verify  $R^2$  information.
  - 12: **until**  $\max\{\dot{Q}_2\}$  is reached **or** no more data is available
-

### 3.5 Conclusions

In this work, a non-conventional calorimeter is proposed as a complementary tool for thermal management applications in microelectronic devices. This system was designed as a horizontal cylindrical geometry and based on natural convection, without external power sources for the system's operation. The calorimeter is composed of five parts, *i.e.*, the *Enclosure*, *Coat*, *Tank*, *Heat Sink* and *Cover*, since the *Tank* and *Heat Sink* are the classical principal components, such as the fluid reservoir and main chamber, used in calorimetric applications. The proposed system was built using chiefly expanded polystyrene and polyurethane foams, steel and aluminium materials, and common water as working fluid. It was instrumented employing six digital thermometers, three of them were sheathed in a stainless steel waterproof case, and a minicomputer to monitoring, processing and publishing the current process status.

Later, the calorimeter was modelled and numerically simulated employing a symmetry-based reduced system. At first, the stationary state analyses of the reduced system gave us useful information for the correct placement of temperature sensors. Also, results showed the reduced scale of the fluid motion inside the reservoir filled with the working fluid, which allowed a reduction of the problem complexity. Hence, four sets of time dependent simulations were considered with the features of whether include the fluid motion (Navier-Stokes equations), as well as, the inclusion of a practical or ideal insulation. From these analyses, it was observed the importance of employ an excellent insulation for the calorimetric determination of the electronic device power losses. In other words, it was realised that the desired operation of system, in the heat transfer sense, lays on trying to “*slowly burn it up*”. Also, it was performed a preliminary study about the influence of using a water-based copper nanofluid, with difference nanoparticles concentrations, as working fluid in the calorimeter. There was observed slightly enhancements on the determination, which could be inconclusive for practical purposes.

Finally, the calorimeter was experimentally implemented utilising well-known power dissipation values for its characterisation and calibrations. Experimental results corroborated the knowledge acquired in the numerical simulation of the reduced-system. It was found that the calorimeter system can be simplified using a lumped circuit model with  $R = 1.17$  K/W, and  $C = 167.94$  kJ/K. This values laid out information about the time constant for the system, about 50 h, with the water's temperature behaviour as the response of an ordinary first order system. Furthermore, an strategy for determining the power dissipated by a microelectronic devices was defined, aimed to reduce the time elapsed for a power measurement, because more than 50 h could jeopardise the microelectronic device. Nonetheless, it could be useful to test the robustness of these devices. Those long term experiments, mainly due calorimeter's physics, which is governed by natural convection as the heat transfer mechanism, were reduced with the proposed strategy to 23.47 h, at most. It was noticed that measuring times decrease with greater power dissipations. The non-conventional calorimeter was tested with powers from 1.00 W to 20 W, However, power dissipation values greater than 20 W can be detected with ease, monitoring the chamber temperature to avoid any malfunctioning in the electronic component. Conversely, the system in its current state is incapable of detect powers below 1.00 W, thus additional improvements must be performed to allow that.



# Chapter 4

## Summary

This research reported an alternative methodology for solving the well-known thermal management problem of microelectronic components. The methodology is divided in two parts, which consist on the optimal design procedure for heat sinks and the power dissipation measurement using a non-conventional calorimeter. The strategy studied in the first part is based on the entropy generation minimisation (EGM) criterion and modern optimisation methods. Second part constituted the creation procedure, from the conceptual designing to the practical implementation, of the non-conventional calorimeter for the measurement of microelectronic power dissipation. This calorimeter is proposed as a complementary tool for thermal management applications in microelectronic devices, such as to determine the heat power generation eventually utilised in a particular-purpose cooling system designing. In addition, this work deploys various areas of interest to continue researching and generating new knowledge. Some of the topics that surely are going to be investigated are presented in Section 4.1 as future works. Finally, all results reported in this document, further other related work performed during this research period, were peer-reviewed and published in specialised journals or presented in scientific conferences. A detailed list of them is displayed in Section 4.2.

### 4.1 Future works

- To perform a comprehensive simulation of the entire system considering different conditions and alternatives for the calorimeter's improvement. Some of them could be, *e.g.*, considering a working fluid with greater heat capacity than water and adding a mixing mechanism to boosting up the convection process. Moreover, it was found that nanoparticles in the working fluid slightly enhance the calorimetric performance, which could be increased by integrating an electromagnetic field.
- To study the effect of the number of plate-fins in the radial heat sink and the related discrepancies between the designed and the manufactured heat sink.
- To extend the calorimeter's model considering the characterisation of the heat transfer from the main chamber to the working fluid. Further features can be distinguished such as film coefficients, total power losses, etc.
- To improve the temperature sensors' sensitivity immersed in the working fluid, because the waterproof sheathed affected drastically their measurement giving place to staircase-shaped temperature curves.

- To implement and improve the digital signal processing mechanisms carried out in the present study.
- To explore other modelling strategies, which could contribute to the general understanding of the tackled phenomenon, *e.g.*, the calorimetric analysis of microelectronic components under the theory of fractional calculus.
- To disseminate the results found here in the academy and, especially, in the training of future engineers and technicians.

## 4.2 Scientific production

### JCR indexed journals

1. Cruz-Duarte, J. M., Rosales-Garcia, J., Correa-Cely, C. R., Garcia-Perez, A., & Avina-Cervantes, J. G. (2018). A closed form expression for the Gaussian-based Caputo–Fabrizio fractional derivative for signal processing applications. *Communications in Nonlinear Science and Numerical Simulation*, 61, 138–148. **(IF/2017-2018: 3.181)**
2. Contreras, A. O., García, J. J. R., Jiménez, L. M., & Cruz-Duarte, J. M. (2018). Analysis of projectile motion in view of conformable derivative. *Open Physics*, 16, 581-587. **(IF/2017: 0.755)**
3. Lopez-Dieguez, Y., Estudillo-Ayala, J. M., Jauregui-Vazquez, D., Sierra-Hernandez, J. M., Herrera-Piada, L. A., Cruz-Duarte, J. M., Hernandez-Garcia, & J.C., Rojas-Laguna, R. (2017). Multi-mode all Fiber Interferometer based on Fabry-Perot Multi-cavity and its Temperature Response. *Optik - International Journal for Light and Electron Optics*, 147, 232–239. **(IF/2017-2018: 1.191)**
4. Cruz-Duarte, J. M., Morega, A. M., Garcia-Perez, A., & Correa-Cely, C. R. (2017). Numerical simulation of heat transfer process in a non-conventional calorimeter. *Rev. Roum. Sci. Techn.- Électrotechn. et Énerg.*, 62(4), 424–430. **(IF/2017-2018: 1.114)**
5. Cruz-Duarte, J. M., Garcia-Perez, A., Amaya-Contreras, I. M., Correa-Cely, C. R., Romero-Troncoso, R. J., & Avina-Cervantes, J. G. (2017). Design of Microelectronic Cooling Systems Using a Thermodynamic Optimization Strategy Based on Cuckoo Search. *IEEE Transactions on Components, Packaging and Manufacturing Technology*, PP(99), 1–9. **(IF/2017-2018: 1.66)**
6. Cruz-Duarte, J. M., Garcia-Perez, A., Amaya-Contreras, I. M., & Correa-Cely, C. R. (2016). Designing a microchannel heat sink with colloidal coolants through the entropy generation minimisation criterion and global optimisation algorithms. *Applied Thermal Engineering*, 100, 1052–1062. **(IF/2016: 3.356)**
7. Ilunga-Mbuyamba, E., Cruz-Duarte, J. M., Avina-Cervantes, J. G., Correa-Cely, C. R., Lindner, D., & Chalopin, C. (2016). Active contours driven by Cuckoo Search strategy for brain tumour images segmentation. *Expert Systems with Applications*, 56, 59–68. **(IF/2016: 3.928)**

### Conferences and proceedings

1. Guerra, K., Cruz-Duarte, J. M., & Correa, R. (2019). Methodology to solve Mass-Spring-Dashpot (MSD) models through global optimization algorithms. *Revista UIS Ingenierías*, 18(1), 49–60.
2. Matajira-Rueda, D., Cruz-Duarte, J. M., Garcia-Perez, A., Avina-Cervantes, J.G., & Correa-Cely, C.R. A New Improvement Scheme Of Spiral Algorithm (Performance Test). In 2018 IEEE International Autumn Meeting on Power, Electronics and Computing (ROPEC), Nov., 2018, Mexico.
3. Cruz-Duarte, J. M., Garcia-Perez, A., Amaya-Contreras, I., Correa, R., Assessing Film Coefficients of Microchannel Heat Sinks Through the Cuckoo Search Algorithm. In the 7th International Conference on Metaheuristics and Nature Inspired Computing META'18, Oct., 2018.
4. Minjares, J. M., Shmaliy, Y., Ramirez, M. L., & Cruz-Duarte, J. M. (2018). Identifying Outliers in HRV – Seizure Signals using p-shift UFIR Baseline Estimates. In WSEAS Transactions on Signal Processing (pp. 109–114).
5. Martínez-Jiménez, L., Cruz-Duarte, J. M., Rosales, J. J., & Cruz-Aceves, I. (2018). Enhancement of Vessels in Coronary Angiograms Using a Hessian Matrix Based on Grünwald-Letnikov Fractional Derivative. In Proceedings of the 2018 8th International Conference on Biomedical Engineering and Technology - ICBET'18 (pp. 51–54). New York, New York, USA: ACM Press.
6. Matajira-Rueda, D., Cruz-Duarte, J., Avina-Cervantes, J., & Correa-Cely, C. (2018). Global optimization algorithms applied in a parameter estimation strategy. *Revista UIS Ingenierías*, 17(1), 233–242.
7. Cruz-Duarte, J. M., Martin-Diaz, I., Munoz-Minjares, J. U., Sanchez-Galindo, L. A., Avina-Cervantes, J. G., Garcia-Perez, A., & Correa-Cely, C. R. (2017). Primary study on the stochastic spiral optimization algorithm. In 2017 IEEE International Autumn Meeting on Power, Electronics and Computing (ROPEC) (pp. 1–6). Ixtapa, Mexico: IEEE.
8. Cruz-Duarte, J. M., Avina-Cervantes, J. G., Amaya-Contreras, I. M., & Correa-Cely, C. R. (2015). Design of an Optimal Heat Sink for Microelectronic Devices Using Entropy Generation Minimization. 2015 Fourteenth Mexican International Conference on Artificial Intelligence (MICAI), 231–235.





# Bibliography

- [1] Lei He, Shauki Elassaad, Yiyu Shi, Yu Hu, and Wei Yao. System-in-Package: Electrical and Layout Perspectives. *Foundations and Trends® in Electronic Design Automation*, 4(4):223–306, 2010.
- [2] Andreas C Fischer, Fredrik Forsberg, Martin Lapisa, Simon J Bleiker, Göran Stemme, Niclas Roxhed, and Frank Niklaus. Integrating MEMS and ICs. *Microsystems & Nanoengineering*, 1:15005, may 2015.
- [3] Christine Harendt, Jan Kostelnik, Andreas Kugler, Enno Lorenz, Stefan Saller, Alina Schreivogel, Zili Yu, and Joachim N. Burghartz. Hybrid Systems in Foil (HySiF) exploiting ultra-thin flexible chips. *Solid-State Electronics*, 113:101–108, 2015.
- [4] Arnold Knott, Toke M. Andersen, Peter Kamby, Jeppe A. Pedersen, Mickey P. Madsen, Milovan Kovacevic, and Michael A. E. Andersen. Evolution of Very High Frequency Power Supplies. *IEEE Journal of Emerging and Selected Topics in Power Electronics*, 2(3):386–394, 2014.
- [5] Rao R Tummala. 3d system package architecture as alternative to 3d stacking of ics with tsv at system level. In *Electron Devices Meeting (IEDM), 2017 IEEE International*, pages 3–4. IEEE, 2017.
- [6] Santagata Fabio, Jianwen Sun, Elina Iervolino, Hongyu Yu, Fei Wang, Guoqi Zhang, PM Sarro, and Guoyi Zhang. System in package (sip) technology: fundamentals, design and applications. *Microelectronics International*, 1(just-accepted):00–00, 2018.
- [7] Chris Bailey and John Parry. Co-design, modelling and simulation challenges: From components to systems. In *Thermal Investigations of ICs and Systems (THERMINIC), 2017 23rd International Workshop on*, pages 1–4. IEEE, 2017.
- [8] Bill Chen. Heterogeneous Integration Roadmap—A Vision to the Future. *IEEE Electronics Packaging Society Newsletter*, 40(1):12–13, jan 2018.
- [9] Ko Tao Lee, Can Bayram, Daniel Piedra, Edmund Sprogis, Hariklia Deligianni, Balakrishnan Krishnan, George Pappasoulotis, Ajit Paranjpe, Eyal Aklimi, Ken Shepard, Tomás Palacios, and Devendra Sadana. GaN Devices on a 200 mm Si Platform Targeting Heterogeneous Integration. *IEEE Electron Device Letters*, 38(8):1094–1096, 2017.
- [10] Subramanian S.S. Iyer. Heterogeneous Integration for Performance and Scaling. *IEEE Transactions on Components, Packaging and Manufacturing Technology*, 6(7):1–10, 2016.

- [11] Charles A Harper and Ronald N Sampson. *Electronic materials and processes handbook*. McGraw-Hill Professional Publishing, 1994.
- [12] Merrill L Minges et al. *Electronic materials handbook: packaging*, volume 1. ASM International, 1989.
- [13] Kyle L. Grosse, Myung Ho Bae, Feifei Lian, Eric Pop, and William P. King. Nanoscale Joule heating, Peltier cooling and current crowding at graphene-metal contacts. *Nature Nanotechnology*, 6(5):287–290, 2011.
- [14] Yunus A Cengel. Cooling Electronic Equipment. In *Heat Transfer: A Practical Approach*, pages 1501–1569. McGraw Hill Science/Engineering/Math, 2nd edition, 2002.
- [15] WG Alshaer, MA Rady, SA Nada, Elena Palomo Del Barrio, and Alain Sommier. An experimental investigation of using carbon foam–pcm–mwcnts composite materials for thermal management of electronic devices under pulsed power modes. *Heat and Mass Transfer*, 53(2):569–579, 2017.
- [16] Suresh V Garimella, Tim Persoons, Justin A Weibel, and Vadim Gektin. Electronics thermal management in information and communications technologies: Challenges and future directions. *IEEE Transactions on Components, Packaging and Manufacturing Technology*, 7(8):1191–1205, 2017.
- [17] Trijo Tharayil, Lazarus Godson Asirvatham, S Rajesh, and Somchai Wongwises. Thermal management of electronic devices using combined effects of nanoparticle coating and graphene–water nanofluid in a miniature loop heat pipe. *IEEE Transactions on Components, Packaging and Manufacturing Technology*, 8(7):1241–1253, 2018.
- [18] J. Thammanna and A. Srivastav. Thermal Management in Electronic Equipment. Technical Report February, HCL Technologies, 2010.
- [19] Johan Liu and Teng Wang. Carbon nanotubes for thermal management of microsystems. In *Nanopackaging*, pages 775–791. Springer, 2018.
- [20] Taeyoung Han, Erik Yen, Bahram Khalighi, and Shailendra Kaushik. Li-ion battery pack thermal management? liquid vs air cooling. *Journal of Thermal Science and Engineering Applications*, 2018.
- [21] NV Apollo, A Ahnood, H Zhan, K Ganesan, AJR Smith, S Praver, and DJ Garrett. Cooling of miniature electronic systems using diamond circuit boards. In *2018 17th IEEE Intersociety Conference on Thermal and Thermomechanical Phenomena in Electronic Systems (ITherm)*, pages 340–344. IEEE, 2018.
- [22] Nam Nguyen, Songlin Zhang, Abiodun Oluwalowo, Jin Gyu Park, Kang Yao, and Richard Liang. High-performance and lightweight thermal management devices by 3d printing and assembly of continuous carbon nanotube sheets. *ACS applied materials & interfaces*, 10(32):27171–27177, 2018.
- [23] V Lakshminarayanan and M Soundarakumar. Thermal effects in a printed circuit board due to heat emission from mounted components. In *Microelectronics Packaging (NordPac), 2017 IMAPS Nordic Conference on*, pages 101–108. IEEE, 2017.

- [24] Justin L Smoyer and Pamela M Norris. Brief historical perspective in thermal management and the shift toward management at the nanoscale. *Heat Transfer Engineering*, pages 1–14, 2018.
- [25] John Humphries. Thermal management of electronic devices. *OnBoard Technology*, 1(February):48–50, 2006.
- [26] Sarabjeet Singh Sidhu, Sanjeev Kumar, and Ajay Batish. Metal Matrix Composites for Thermal Management: A Review. *Critical Reviews in Solid State and Materials Sciences*, 41(2):132–157, 2016.
- [27] Arden L. Moore and Li Shi. Emerging challenges and materials for thermal management of electronics. *Materials Today*, 17(4):163–174, 2014.
- [28] Richard C. Chu, Robert E. Simons, Michael J. Ellsworth, Roger R. Schmidt, and Vincent Cozzolino. Review of cooling technologies for computer products. *IEEE Transactions on Device and Materials Reliability*, 4(4):568–585, 2004.
- [29] Xianping Chen, Huaiyu Ye, Xuejun Fan, Tianling Ren, and Guoqi Zhang. A review of small heat pipes for electronics. *Applied Thermal Engineering*, 96:1–17, 2016.
- [30] Craig Green, Peter Kottke, Xuefei Han, Casey Woodrum, Thomas Sarvey, Pouya Asrar, Xuchen Zhang, Yogendra Joshi, Andrei Fedorov, Suresh Sitaraman, and Muhanad Bakir. A Review of Two-Phase Forced Cooling in Three-Dimensional Stacked Electronics: Technology Integration. *Journal of Electronic Packaging*, 137(4):040802, 2015.
- [31] Ali Elghool, Firdaus Basrawi, Thamir Khalil Ibrahim, Khairul Habib, Hassan Ibrahim, and Daing Mohamad Nafiz Daing Idris. A review on heat sink for thermoelectric power generation: Classifications and parameters affecting performance. *Energy Conversion and Management*, 134:260–277, 2017.
- [32] Tisha Dixit and Indranil Ghosh. Review of micro- and mini-channel heat sinks and heat exchangers for single phase fluids. *Renewable and Sustainable Energy Reviews*, 41:1298–1311, 2015.
- [33] Satish G Kandlikar. Review and Projections of Integrated Cooling Systems for Three-Dimensional Integrated Circuits. *Journal of Electronic Packaging*, 136(2):24001, 2014.
- [34] Sambhaji T. Kadam and Ritunesh Kumar. Twenty first century cooling solution: Microchannel heat sinks. *International Journal of Thermal Sciences*, 85:73–92, nov 2014.
- [35] Ziyue Ling, Zhengguo Zhang, Guoquan Shi, Xiaoming Fang, Lei Wang, Xuenong Gao, Yutang Fang, Tao Xu, Shuangfeng Wang, and Xiaohong Liu. Review on thermal management systems using phase change materials for electronic components, Li-ion batteries and photovoltaic modules. *Renewable and Sustainable Energy Reviews*, 31:427–438, 2014.
- [36] Azad Qazi Zade, Metin Renksizbulut, and Jacob Friedman. Heat transfer characteristics of developing gaseous slip-flow in rectangular microchannels with variable

- physical properties. *International Journal of Heat and Fluid Flow*, 32(1):117–127, feb 2011.
- [37] Stéphane Colin. Gas Microflows in the Slip Flow Regime: A Critical Review on Convective Heat Transfer. *Journal of Heat Transfer*, 134(2):020908, 2012.
- [38] Satish G Kandlikar, Stéphane Colin, Yoav Peles, Srinivas Garimella, R Fabian Pease, Juergen J Brandner, and David B Tuckerman. Heat Transfer in Microchannels—2012 Status and Research Needs. *Journal of Heat Transfer*, 135(September 2013):18, 2013.
- [39] Ahmed Mohammed Adham, Normah Mohd-Ghazali, and Robiah Ahmad. Optimization of an ammonia-cooled rectangular microchannel heat sink using multi-objective non-dominated sorting genetic algorithm (NSGA2). *Heat and Mass Transfer*, 48(10):1723–1733, may 2012.
- [40] Jorge Cruz, Ivan Iván Amaya, and Rodrigo Correa. Optimal rectangular microchannel design, using simulated annealing, unified particle swarm and spiral algorithms, in the presence of spreading resistance. *Applied Thermal Engineering*, 84:126–137, jun 2015.
- [41] Lan-Ying Zhang, Yang-Fei Zhang, Jia-Qi Chen, and Shu-Lin Bai. Fluid flow and heat transfer characteristics of liquid cooling microchannels in LTCC multilayered packaging substrate. *International Journal of Heat and Mass Transfer*, 84:339–345, 2015.
- [42] Gongnan Xie, Fengli Zhang, Bengt Sundén, and Weihong Zhang. Constructal design and thermal analysis of microchannel heat sinks with multistage bifurcations in single-phase liquid flow. *Applied Thermal Engineering*, 62(2):791–802, jan 2014.
- [43] John Vetrovec. Quasi-Passive Heat Sink for High-Power Laser Diodes. In Mark S. Zediker, editor, *SPIE*, volume 7198, pages 1–10, San Jose, CA, feb 2009.
- [44] Jean-Antoine Gruss, Christophe Bouzon, and Bernard Thonon. Extruded Microchannel-Structured Heat Exchangers. *Heat Transfer Engineering*, 26(3):56–63, feb 2005.
- [45] M. Reyes, J.R. Arias, A. Velazquez, and J.M. Vega. Experimental study of heat transfer and pressure drop in micro-channel based heat sinks with tip clearance. *Applied Thermal Engineering*, 31(5):887–893, apr 2011.
- [46] Chander Shekhar Sharma, Manish K Tiwari, Bruno Michel, and Dimos Poulikakos. Thermofluidics and energetics of a manifold microchannel heat sink for electronics with recovered hot water as working fluid. *International Journal of Heat and Mass Transfer*, 58(1-2):135–151, mar 2013.
- [47] Guangxin Hu and Shanglong Xu. Optimization design of microchannel heat sink based on SQP method and numerical simulation. In *2009 International Conference on Applied Superconductivity and Electromagnetic Devices*, pages 89–92. IEEE, sep 2009.
- [48] Afzal Husain, Sun-Min Kim, and Kwang-Yong Kim. Performance analysis and design optimization of micro-jet impingement heat sink. *Heat and Mass Transfer*, 49(11):1613–1624, jul 2013.

- [49] Ali Kosar and Yoav Peles. Thermal-Hydraulic Performance of MEMS-based Pin Fin Heat Sink. *Journal of Heat Transfer*, 128(2):121, 2006.
- [50] Salma Halefadi, Ahmed Mohammed Adham, Normah Mohd-Ghazali, Thierry Maré, Patrice Estellé, and Robiah Ahmad. Optimization of thermal performances and pressure drop of rectangular microchannel heat sink using aqueous carbon nanotubes based nanofluid. *Applied Thermal Engineering*, 62(2):492–499, jan 2014.
- [51] Yue-Tzu Yang, Kuo-Teng Tsai, Yi-Hsien Wang, and Shih-Han Lin. Numerical study of microchannel heat sink performance using nanofluids. *International Communications in Heat and Mass Transfer*, 57:27–35, oct 2014.
- [52] Assel Sakanova, Shan Yin, Jiyun Zhao, J.M. Wu, and K.C. Leong. Optimization and comparison of double-layer and double-side micro-channel heat sinks with nanofluid for power electronics cooling. *Applied Thermal Engineering*, 65(1-2):124–134, apr 2014.
- [53] M. Hatami and D.D. D. Ganji. Thermal and flow analysis of microchannel heat sink (MCHS) cooled by Cu-water nanofluid using porous media approach and least square method. *Energy Conversion and Management*, 78:347–358, feb 2014.
- [54] Ahmed Adham, Normah Mohd-Ghazali, and Robiah Ahmad. Optimization of nanofluid-cooled microchannel heat sink. *Thermal Science*, 20(1):109–118, 2016.
- [55] Reiyu Chein and Jason Chuang. Experimental microchannel heat sink performance studies using nanofluids. *International Journal of Thermal Sciences*, 46(1):57–66, jan 2007.
- [56] Yanhai Lin, Liancun Zheng, and Xinxin Zhang. Radiation effects on Marangoni convection flow and heat transfer in pseudo-plastic non-Newtonian nanofluids with variable thermal conductivity. *International Journal of Heat and Mass Transfer*, 77:708–716, oct 2014.
- [57] Benjamin Rimbault, Cong Tam Nguyen, and Nicolas Galanis. Experimental investigation of CuO–water nanofluid flow and heat transfer inside a microchannel heat sink. *International Journal of Thermal Sciences*, 84:275–292, oct 2014.
- [58] Ping Li, Di Zhang, and Yonghui Xie. Heat transfer and flow analysis of Al<sub>2</sub>O<sub>3</sub>–water nanofluids in microchannel with dimple and protrusion. *International Journal of Heat and Mass Transfer*, 73:456–467, jun 2014.
- [59] Shahabeddin K. Mohammadian and Yuwen Zhang. Analysis of nanofluid effects on thermoelectric cooling by micro-pin-fin heat exchangers. *Applied Thermal Engineering*, 70(1):282–290, sep 2014.
- [60] Yanlong Li, Fengli Zhang, Bengt Sundén, and Gongnan Xie. Laminar thermal performance of microchannel heat sinks with constructal vertical Y-Shaped bifurcation plates. *Applied Thermal Engineering*, 73(1):185–195, jul 2014.
- [61] K.Y. Leong and Hwai Chyuan Ong. Entropy generation analysis of nanofluids flow in various shapes of cross section ducts. *International Communications in Heat and Mass Transfer*, jul 2014.

- [62] M R Sohel, S S Khaleduzzaman, R Saidur, a Hepbasli, M F M Sabri, and I M Mahbubul. An experimental investigation of heat transfer enhancement of a minichannel heat sink using Al<sub>2</sub>O<sub>3</sub> – H<sub>2</sub>O nanofluid. *Heat and Mass Transfer*, 74(4):164–172, 2014.
- [63] T. Bello-Ochende, J P Meyer, and F. U. Ighalo. Combined Numerical Optimization and Constructal Theory for the Design of Microchannel Heat Sinks, 2010.
- [64] Lin Lin, Yang-Yang Chen, Xin-Xin Zhang, and Xiao-Dong Wang. Optimization of geometry and flow rate distribution for double-layer microchannel heat sink. *International Journal of Thermal Sciences*, 78:158–168, apr 2014.
- [65] Sajjad Bigham, Hossein Shokouhmand, Rasool Nasr Isfahani, and Sajjad Yazdani. Fluid Flow and Heat Transfer Simulation in a Constricted Microchannel: Effects of Rarefaction, Geometry, and Viscous Dissipation. *Numerical Heat Transfer, Part A: Applications*, 59(3):209–230, feb 2011.
- [66] S.G. Kandlikar and H.R. Upadhye. Extending the heat flux limit with enhanced microchannels in direct single phase cooling of computer chips. In *Semiconductor Thermal Measurement and Management IEEE Twenty First Annual IEEE Symposium, 2005.*, pages 8–15. Ieee, 2005.
- [67] M. Bahrami, J. R. Culham, M. M. Yananovich, and G. E. Schneider. Review of Thermal Joint Resistance Models for Nonconforming Rough Surfaces. *Applied Mechanics Reviews*, 59(1):1, 2006.
- [68] Atsushi Tatami, Masamitsu Tachibana, Takashi Yagi, Megumi Akoshima, and Mut-suaki Murakami. High Thermal Conductive Graphite Films from Thin Polymer Films. In *Proceedings of the 15th International Heat Transfer Conference*, page 7, Kyoto, 2014.
- [69] Ismail Solmus. Numerical investigation of heat transfer and fluid flow behaviors of a block type graphite foam heat sink inserted in a rectangular channel. *Applied Thermal Engineering*, 78:605–615, dec 2015.
- [70] H. Fukushima, L. T. Drzal, B. P. Rook, and M. J. Rich. Thermal conductivity of exfoliated graphite nanocomposites. *Journal of Thermal Analysis and Calorimetry*, 85(1):235–238, 2006.
- [71] S. Zhou, W. Luo, H. Zou, M. Liang, and S. Li. Enhanced thermal conductivity of polyamide 6/polypropylene (PA6/PP) immiscible blends with high loadings of graphite. *Journal of Composite Materials*, 2015.
- [72] C. Zhang, X. He, Q. Liu, S. Ren, and X. Qu. Fabrication and thermo-physical properties of graphite flake/copper composites. *Journal of Composite Materials*, dec 2014.
- [73] Yue Feng Li. Research on Expanded Graphite/Nitrate High-Temperature Composite Phase Change Materials. *Applied Mechanics and Materials*, 740:11–14, 2015.
- [74] MJ Mochane and AS Luyt. The effect of expanded graphite on the thermal stability, latent heat, and flammability properties of eva/wax phase change blends. *Polymer Engineering & Science*, 55(6):1255–1262, 2015.

- [75] P.D. D Malliband. Design of a double-jacketed, closed type calorimeter for direct measurement of motor losses. In *Seventh International Conference on Power Electronics and Variable Speed Drives*, number 456 in 1, pages 212–217. IEE, 1998.
- [76] Chucheng Xiao Chucheng Xiao, Gang Chen Gang Chen, and W.G.H. G H Odendaal. Overview of Power Loss Measurement Techniques in Power Electronics Systems. *IEEE Transactions on Industry Applications*, 43(3):657–664, 2007.
- [77] Yang Liu, Liming Shi, and Yaohua Li. Comparison analysis of loss calculation methods and measurement techniques in power electronics and motor systems. In *2013 International Conference on Electrical Machines and Systems (ICEMS)*, pages 530–534. IEEE, oct 2013.
- [78] Patrick K Gallagher, Michael E Brown, and R B Kemp. *Handbook of thermal analysis and calorimetry*. Elsevier, 1999.
- [79] John P McCullough and Donald W Scott. *Calorimetry of Non-Reacting Systems: Prepared Under the Sponsorship of the International Union of Pure and Applied Chemistry Commission on Thermodynamics and the Thermochemistry*, volume 1. Elsevier, 2013.
- [80] J Lerchner, A Wolf, G Wolf, V Baier, E Kessler, M Nietzsche, and M Krügel. A new micro-fluid chip calorimeter for biochemical applications. *Thermochimica Acta*, 445(2):144–150, 2006.
- [81] Jeison Marín, Diego Tibaduiza, and Rodrigo Correa. Determinación experimental de la cantidad de calor emitido por un circuito electrónico. *Revista Ingenierías Universidad de Medellín*, 11(20):191–202, 2012.
- [82] Frede Blaabjerg, J.K. K Pedersen, and E. Ritchie. Calorimetric measuring systems for characterizing high frequency power losses in power electronic components and systems. In *Conference Record of the 2002 IEEE Industry Applications Conference. 37th IAS Annual Meeting (Cat. No.02CH37344)*, volume 2, pages 1368–1376. IEEE, 2002.
- [83] P. D. Malliband, N. P. Van Der Duijn Schouten, and R. A. McMahon. Precision calorimetry for the accurate measurement of inverter losses. *Proceedings of the International Conference on Power Electronics and Drive Systems*, 1:321–326, 2003.
- [84] Sven Weier, Mohsin A. Shafi, and Richard McMahon. Precision calorimetry for the accurate measurement of losses in power electronic devices. *IEEE Transactions on Industry Applications*, 46(1):278–284, 2010.
- [85] D. Christen, U. Badstuebner, J. Biela, and J. W. Kolar. Calorimetric power loss measurement for highly efficient converters. *2010 International Power Electronics Conference - ECCE Asia -, IPEC 2010*, pages 1438–1445, 2010.
- [86] Damien F. Frost and David A. Howey. High-speed Peltier calorimeter for the calibration of high-bandwidth power measurement equipment. *IEEE Transactions on Instrumentation and Measurement*, 65(1):155–163, 2016.
- [87] A. Bejan and A. M. Morega. Optimal Arrays of Pin Fins and Plate Fins in Laminar Forced Convection. *Journal of Heat Transfer*, 115(1):75, 1993.



- [88] Al M. Morega and A. Bejan. Heatline visualization of forced convection laminar boundary layers. *International Journal of Heat and Mass Transfer*, 36(16):3957–3966, 1993.
- [89] G. Ledezma, A. M. Morega, and A. Bejan. Optimal Spacing Between Pin Fins With Impinging Flow. *Journal of Heat Transfer*, 118(August 1996), 1996.
- [90] A M Morega and A Bejan. A constructal approach to the optimal design of photovoltaic cells. *International Journal of Green Energy*, 2(JULY):233–242, 2005.
- [91] A. M. Morega, M. Morega, L. Pîslaru-Dănescu, V. Stoica, F. Nouras, and F. D. Stoian. A novel, ferrofluid-cooled transformer. Electromagnetic field and heat transfer by numerical simulation. *Proceedings of the International Conference on Optimization of Electrical and Electronic Equipment, OPTIM*, pages 140–146, 2010.
- [92] I. Dobrin, A. M. Morega, A. Nedelcu, and M. Morega. Design and fabrication of a 5 T NbTi solenoid magnet cooled by a closed-cycle G-M cryocooler. *2013 - 8th International Symposium on Advanced Topics in Electrical Engineering, ATEE 2013*, pages 0–3, 2013.
- [93] L. Pîslaru-Danescu, A. M. Morega, M. Morega, and V. Stoica. New concept of measurement apparatus for the in situ electrical resistivity of concrete structures. *2013 - 8th International Symposium on Advanced Topics in Electrical Engineering, ATEE 2013*, 2013.
- [94] A. M. Morega, N. Tanase, M. Popa, M. Morega, and J. B. Dumitru. Numerical simulation of an electromagnetic bending-mode cantilever microactuator. *2013 - 8th International Symposium on Advanced Topics in Electrical Engineering, ATEE 2013*, 1(1), 2013.
- [95] J B Dumitru, A M Morega, L Pîslaru-d, and M Morega. A Parametric Study of Lumped Circuit Parameters of a Miniature Planar Spiral Transformer. In *8th International symposium on advanced topics in electrical engineering*, pages 1–6, 2013.
- [96] Alexandru M. Morega, Alin A Dobre, and Mihaela Morega. Numerical simulation in electrical cardiometry. In *2012 13th International Conference on Optimization of Electrical and Electronic Equipment (OPTIM)*, pages 1407–1412. IEEE, may 2012.
- [97] Alexandru M Morega, M S Alina, and Mihaela Morega. On the Thermography Mapping of Anatomic Media with Capillaries and Larger Vessels Blood Flow. In *5th IEEE International Conference on E-Health and Bioengineering*, pages 1–5, Iasi, 2015.
- [98] Mihaela Morega, Alexandru M Morega, and S Alina. Sensitivity to Parameters Variation in Numerical Simulation of Microwave Thermotherapy. *9th International symposium on advanced topics in electrical engineering*, pages 313–316, 2015.
- [99] Diana M. Ciuculete and Alexandru M. Morega. Numerical simulation of transdermal transport through iontophoresis. In *2015 E-Health and Bioengineering Conference (EHB)*, number 4 in 1, pages 1–5. IEEE, nov 2015.

- [100] Masoud Asadi, Gongnan Xie, and Bengt Sundén. A review of heat transfer and pressure drop characteristics of single and two-phase microchannels. *International Journal of Heat and Mass Transfer*, 79:34–53, dec 2014.
- [101] D.B. B Tuckerman and R.F.W. F W Pease. High-performance heat sinking for VLSI. *IEEE Electron Device Letters*, 2(5):126–129, may 1981.
- [102] Chuan Leng, Xiao-Dong Wang, Tian-Hu Wang, and Wei-Mon Yan. Optimization of thermal resistance and bottom wall temperature uniformity for double-layered microchannel heat sink. *Energy Conversion and Management*, 93:141–150, 2015.
- [103] Assel Sakanova, Jiyun Zhao, and King-Jet Tseng. Investigation on the Influence of Nanofluids in Wavy Microchannel Heat Sink. *IEEE Transactions on Components, Packaging and Manufacturing Technology*, 5(7):956–970, jul 2015.
- [104] Masoud Kharati-Koopae and Mohsen Zare. Effect of aligned and offset roughness patterns on the fluid flow and heat transfer within microchannels consist of sinusoidal structured roughness. *International Journal of Thermal Sciences*, 90:9–23, 2015.
- [105] Ahmed Mohammed Adham, Normah Mohd-Ghazali, and Robiah Ahmad. Thermal and hydrodynamic analysis of microchannel heat sinks: A review. *Renewable and Sustainable Energy Reviews*, 21:614–622, may 2013.
- [106] Jorge Mario Cruz-Duarte, Iván Mauricio Amaya-Contreras, and Carlos Rodrigo Correa-Cely. An optimal high thermal conductive graphite microchannel for electronic device cooling. *Revista Facultad de Ingeniería, Universidad de Antioquia*, 1(77):143–152, 2015.
- [107] Sadik Kakaç and Anchasa Pramuanjaroenkij. Single-phase and two-phase treatments of convective heat transfer enhancement with nanofluids - A state-of-the-art review. *International Journal of Thermal Sciences*, 100:75–97, 2016.
- [108] Baodong Shao, Zhaowei Sun, and Lifeng Wang. Optimization design of microchannel cooling heat sink. *International Journal of Numerical Methods for Heat & Fluid Flow*, 17(6):628–637, 2007.
- [109] Yi Chen, Bei Peng, Xiaohong Hao, and Gongnan Xie. Fast approach of Pareto-optimal solution recommendation to multi-objective optimal design of serpentine-channel heat sink. *Applied Thermal Engineering*, 70(1):263–273, sep 2014.
- [110] J.R. Culham and Y.S. Muzychka. Optimization of plate fin heat sinks using entropy generation minimization. *IEEE Transactions on Components and Packaging Technologies*, 24(2):159–165, jun 2001.
- [111] Ashok Reddy. A Critical Review of Entropy Generation Analysis in Micro Channel Using Nano Fluids. *International Journal of Scientific Development and Research*, 1(5):7–12, 2016.
- [112] Lütfullah Kuddusi. Entropy generation in rectangular microchannels. *International Journal of Exergy*, 19(1):110, 2016.

- [113] Amir Shalchi-Tabrizi and Hamid Reza Seyf. Analysis of entropy generation and convective heat transfer of Al<sub>2</sub>O<sub>3</sub> nanofluid flow in a tangential micro heat sink. *International Journal of Heat and Mass Transfer*, 55(15-16):4366–4375, jul 2012.
- [114] I. Cruz-Aceves, J. G. Aviña-Cervantes, J. M. López-Hernández, and S. E. González-Reyna. Multiple Active Contours Driven by Particle Swarm Optimization for Cardiac Medical Image Segmentation. *Computational and Mathematical Methods in Medicine*, 2013:1–13, 2013.
- [115] I Fister Jr., XS Yang, I Fister, J Brest, and D Fister. A Brief Review of Nature-Inspired Algorithms for Optimization. *ELEKTROTEHNIŠKI VESTNIK*, 80(3):116–122, 2013.
- [116] Ahmed Mohammed Adham, Normah Mohd-Ghazali, and Robiah Ahmad. Optimization of a Rectangular Microchannel Heat Sink Using Entropy Generation Minimization (EGM) and Genetic Algorithm (GA). *Arabian Journal for Science and Engineering*, 39(10):7211–7222, oct 2014.
- [117] Waqar Ahmed Khan, Muhammad Bilal Kadri, and Qasim Ali. Optimization of Microchannel Heat Sinks Using Genetic Algorithm. *Heat Transfer Engineering*, 34(4):279–287, jan 2013.
- [118] Jorge M. Cruz-Duarte, Arturo Garcia-Perez, Ivan M. Amaya-Contreras, and C. Rodrigo Correa-Cely. Designing a microchannel heat sink with colloidal coolants through the entropy generation minimisation criterion and global optimisation algorithms. *Applied Thermal Engineering*, 100:1052–1062, 2016.
- [119] Jorge Cruz, Ivan Amaya, and Rodrigo Correa. Cooling microelectronic devices using optimal microchannel heat sinks. *Revista EIA*, 12(24):151–166, 2015.
- [120] Mohamed Abdel-Basset, Abdel-Naser Hessin, and Lila Abdel-Fatah. A comprehensive study of cuckoo-inspired algorithms. *Neural Computing and Applications*, 2016.
- [121] Baodong Shao, Lifeng Wang, Jianyun Li, and Heming Cheng. Multi-objective optimization design of a micro-channel heat sink using adaptive genetic algorithm. *International Journal of Numerical Methods for Heat & Fluid Flow*, 21(3):353–364, 2011.
- [122] Waqar Ahmed Khan, J.R. Richard Culham, and M.M. Michael Yovanovich. Optimization of Microchannel Heat Sinks Using Entropy Generation Minimization Method. *IEEE Transactions on Components and Packaging Technologies*, 32(2):243–251, jun 2009.
- [123] R. J. Culham, Waqar A. Khan, M. Michael Yovanovich, and Yuri S. Muzychka. The Influence of Material Properties and Spreading Resistance in the Thermal Design of Plate Fin Heat Sinks. *Journal of Electronic Packaging*, 129(1):76, 2007.
- [124] S. J. Kim and D Kim. Forced Convection in Microstructures for Electronic Equipment Cooling. *Journal of Heat Transfer*, 121(3):639, 1999.
- [125] Theodore L Bergman, Frank P Incropera, David P DeWitt, and Adrienne S Lavine. *Fundamentals of heat and mass transfer*. John Wiley & Sons, Hoboken, NJ, USA, 2011.

- [126] MB B Kleiner, SA A Kühn, and K Habeger. High performance forced air cooling scheme employing microchannel heat exchangers. *IEEE Transactions on Components, packaging, and manufacturing technology-Part A*, 18(4):795–804, 1995.
- [127] Alexandru M Morega. Principles of Heat Transfer. In Dan B. Marghitu, editor, *Mechanical Engineer's Handbook*, chapter 7, pages 445–557. Academic Press, 2001.
- [128] John H. Lienhard IV and John H. Lienhard V. *A Heat Transfer Textbook*. Phlogiston Press, Cambridge, M, 4th edition, 2012.
- [129] M M Awad and Y S Muzychka. Thermodynamic Optimization, Heat Exchangers - Basics Design Applications. In Jovan Mitrovic, editor, *Heat Exchangers - Basics Design Applications*, volume 1, chapter 1, page 586. InTech, 2012.
- [130] Satish G Kandlikar. History, advances, and challenges in liquid flow and flow boiling heat transfer in microchannels: A critical review. In *International Heat Transfer Conference*, pages 1–20, Washington, D.C., 2010. ASME.
- [131] Buyoung Yun, Kang G Shin, and Shige Wang. Predicting thermal behavior for temperature management in time-critical multicore systems. *Real-Time Technology and Applications - Proceedings*, pages 185–194, 2013.
- [132] Jinguo Li, Ning Jiang, Zengliang Gao, Hong Liu, and Gengjie Wang. An inverse heat conduction problem of estimating the multiple heat sources for mould heating system of the injection machine. *Inverse Problems in Science and Engineering*, 24(9):1587–1605, nov 2016.
- [133] Guangjun Wang, Lihui Zhang, Xudong Wang, and Bruce L. Tai. An inverse method to reconstruct the heat flux produced by bone grinding tools. *International Journal of Thermal Sciences*, 101:85–92, 2016.
- [134] Guangjun Wang, Lihui Zhang, Xudong Wang, and Bruce L. Tai. An inverse method to reconstruct the heat flux produced by bone grinding tools. *International Journal of Thermal Sciences*, 101:85–92, 2016.
- [135] Yuan Wang, Xiaochuan Luo, Yang Yu, and Qidong Yin. Evaluation of heat transfer coefficients in continuous casting under large disturbance by weighted least squares Levenberg-Marquardt method. *Applied Thermal Engineering*, 111:989–996, 2017.
- [136] Xiaochuan Luo and Zhi Yang. A new approach for estimation of total heat exchange factor in reheating furnace by solving an inverse heat conduction problem. *International Journal of Heat and Mass Transfer*, 112:1062–1071, 2017.
- [137] Mohebbi F, Sellier M, and Rabczuk T. Estimation of linearly temperature-dependent thermal conductivity using an inverse analysis. *International Journal of Thermal Sciences*, 117:68–76, 2017.
- [138] J.K. Dhiman, S.K., Prasad. Inverse estimation of heat flux from a hollow cylinder in cross-flow of air. *Applied Thermal Engineering*, 113(113):952–961, 2017.
- [139] David Matajira-Rueda, Jorge Cruz-Duarte, Juan Avina-Cervantes, and Carlos Correa-Cely. Global optimization algorithms applied in a parameter estimation strategy. *Revista UIS Ingenierías*, 17(1):233–242, 2018.

- [140] M Necat Ozisik. *Inverse heat transfer: fundamentals and applications*. CRC press, 2000.
- [141] KE E Parsopoulos and MN N Vrahatis. UPSO: A unified particle swarm optimization scheme. In *Proceedings of the International Conference of "Computational Methods in Sciences and Engineering*, volume 1 of *Lecture Series on Computer and Computational Sciences*, pages 868–873, Zeist, 2004. VSP International Science Publishers.
- [142] J. Kennedy and R. Eberhart. Particle swarm optimization. In *Proceedings of ICNN'95 - International Conference on Neural Networks*, volume 4, pages 1942–1948, Perth, 1995. IEEE.
- [143] Jérôme Euzenat and John Domingue, editors. *Artificial Intelligence: Methodology, Systems, and Applications*, volume 4183 of *Lecture Notes in Computer Science*. Springer Berlin Heidelberg, Berlin, Heidelberg, 2006.
- [144] Mingzhu Tang, Wen Long, Huawei Wu, Kang Zhang, Yuri A W Shardt, Takuya Shindo, Jianze Xiao, Takuya Kurihara, Sankalap Arora, Satvir B Singh, Narinder Singh, Satvir B Singh, Wang Zhi-gang, Michalis Mavrovouniotis, Changhe Li, Shengxiang Yang, Zakaria N. Alqattan, and Rosni Abdullah. A survey of swarm intelligence for dynamic optimization: Algorithms and applications. *Swarm and Evolutionary Computation*, 2017(4):1–14, 2017.
- [145] Yudong Zhang, Shuihua Wang, Genlin Ji, Yudong Zhang, Shuihua Wang, and Genlin Ji. A Comprehensive Survey on Particle Swarm Optimization Algorithm and Its Applications. *Mathematical Problems in Engineering*, 2015:1–38, 2015.
- [146] Xin-She Yang and Suash Deb. Cuckoo Search via Levy flights. In *2009 World Congress on Nature & Biologically Inspired Computing (NaBIC)*, pages 210–214. IEEE, 2009.
- [147] M.K. K Marichelvam, T. Prabakaran, and X.S. S Yang. Improved cuckoo search algorithm for hybrid flow shop scheduling problems to minimize makespan. *Applied Soft Computing*, 19:93–101, jun 2014.
- [148] Kenichi Tamura and Keiichiro Yasuda. Primary study of spiral dynamics inspired optimization. *Transactions on Electrical and Electronic Engineering*, 6(S1):S98–S100, nov 2011.
- [149] Kenichi Tamura and Keiichiro Yasuda. Spiral Dynamics Inspired Optimization. *Journal of Advanced Computational Intelligence and Intelligent Informatics*, 15(8):1116–1122, 2011.
- [150] Kenichi Tamura and Keiichiro Yasuda. The Spiral Optimization and its stability analysis. In *2013 IEEE Congress on Evolutionary Computation*, pages 1075–1082. IEEE, jun 2013.
- [151] Kenichi Tamura and Keiichiro Yasuda. Spiral Optimization Algorithm with Spiral Trajectories Generating Periodic Descent Directions. *SICE Journal of Control, Measurement, and System Integration*, 9(3):134–143, 2015.
- [152] Jian S Dai. Euler–rodriques formula variations, quaternion conjugation and intrinsic connections. *Mechanism and Machine Theory*, 92:144–152, 2015.

- [153] Jorge M. Cruz-Duarte, Ignacio Martin-Diaz, J. U. Munoz-Minjares, Luis A. Sanchez-Galindo, Juan G. Avina-Cervantes, Arturo Garcia-Perez, and C. Rodrigo Correa-Cely. Primary study on the stochastic spiral optimization algorithm. In *2017 IEEE International Autumn Meeting on Power, Electronics and Computing (ROPEC)*, number Ropec in 1, pages 1–6, Ixtapa, Mexico, nov 2017. IEEE.
- [154] Momin Jamil and Xin She Yang. A literature survey of benchmark functions for global optimisation problems. *International Journal of Mathematical Modelling and Numerical Optimisation*, 4(2):150, 2013.
- [155] W A Khan, M M Yovanovich, and J R Culham. Optimization of microchannel heat sinks using entropy generation minimization method. In *Twenty-Second Annual IEEE Semiconductor Thermal Measurement And Management Symposium*, pages 78–86, Dallas, TX, 2006. IEEE.
- [156] Chih-Wei Chen, Ji-Jen Lee, and Hong-Sen Kou. Optimum thermal design of microchannel heat sinks by the simulated annealing method. *International Communications in Heat and Mass Transfer*, 35(8):980–984, oct 2008.
- [157] Mehdi Ashjaee, Mohammad Goharkhah, Leila Azizi Khadem, and Reza Ahmadi. Effect of magnetic field on the forced convection heat transfer and pressure drop of a magnetic nanofluid in a miniature heat sink. *Heat and Mass Transfer*, 51(7):953–964, jul 2015.
- [158] A. Malvandi and D. D. Ganji. Effects of nanoparticle migration on force convection of alumina/water nanofluid in a cooled parallel-plate channel. *European Journal of Mechanics - B/Fluids*, 52:169–184, 2015.
- [159] Michael E Brown. *Handbook of Thermal Analysis and Calorimetry*, volume 5. Elsevier, 2008.
- [160] Peter Haines, editor. *Principles of Thermal Analysis and Calorimetry*. RSC Paperbacks. Royal Society of Chemistry, Cambridge, 2002.
- [161] B. Aubert and et al. Construction, assembly and tests of the ATLAS electromagnetic barrel calorimeter. *Nuclear Instruments and Methods in Physics Research Section A: Accelerators, Spectrometers, Detectors and Associated Equipment*, 558(2):388–418, mar 2006.
- [162] Yunus A Cengel and Michael A Boles. *Thermodynamics: an engineering approach*, volume 5. McGraw-Hill, New York, 5 edition, 2006.
- [163] Frank Kreith, Raj M. Manglik, and Mark S. Bohn. *Principles of Heat Transfer*. Cengage Learning, Stamford, CT, 7th edition, 2011.
- [164] Koji Orikawa, Atsushi Nigorikawa, and Jun-ichi Itoh. Evaluation on chamber volume and performance for simple calorimetric power loss measurement by two chambers. In *2013 1st International Future Energy Electronics Conference (IFEEC)*, pages 914–919. IEEE, nov 2013.
- [165] Adrian Bejan. *Advanced engineering thermodynamics*. Wiley, New York, 3rd edition, 2006.

- [166] Adrian Bejan. *Convection heat transfer*. John Wiley & Sons, 2013.
- [167] R B Bird, W E Stewart, and E N Lightfoot. *Transport Phenomena*. Wiley, 2nd edition, 2006.
- [168] Donald F. Young, Bruce R. Munson, Theodore H. Okiishi, and Wade W. Huebsch. *A Brief Introduction To Fluid Mechanics*. John Wiley & Sons, Inc., fifth edition, 2010.
- [169] Omid Mahian, Ali Kianifar, Clement Kleinstreuer, Moh'd a. Al-Nimr, Ioan Pop, Ahmet Z. Sahin, and Somchai Wongwises. A review of entropy generation in nanofluid flow. *International Journal of Heat and Mass Transfer*, 65:514–532, oct 2013.
- [170] Douglas C Montgomery and George C Runger. *Applied statistics and probability for engineers*. John Wiley & Sons, 2010.